Experimental investigations of the deep Earth's mantle melting properties

Giacomo Pesce

UNIVERSITÉ BLAISE PASCAL

U.F.R. Science et Technologies

ÉCOLE DOCTORALE DES SCIENCES FONDAMENTALES

Laboratoire Magmas et Volcans

THÉSE

Présentée pour obtenir le grade de

DOCTEUR D'UNIVERSITÉ

Spécialité : Pétrologie expérimentale

Présentée et soutenue publiquement le 07/12/2016

Par

Giacomo PESCE

Experimental investigations of the deep Earth's mantle melting properties

JURY

Gaillard Fabrice	Chargé de recherche – ISTO, Orléans	Rapporteur
Reynard Bruno	Directeur de Recherches – LGLTPE, ENS Lyon	Rapporteur
Debayle Eric	Directeur de Recherche – LGLTPE, ENS Lyon	Examinateur
Laporte Didier	Directeur de Recherche – LMV, Clermont-Fd	Examinateur
Manthilake Geeth	Chargé de Recherche – LMV, Clermont-Fd	Examinateur
Andrault Denis	Professeur – LMV, Clermont-Fd	Directeur de thèse

ABSTRACT

Melting processes play a key role in the Earth's evolution. In the early stages of the Earth's formation, large amounts of heat were released from (i) gravitational energy from core-mantle segregation, (ii) radiogenic decay and (iii) collisions with large-scale impactors (such as the Moon-forming impact). This led to extensive mantle melting with eventual formation of a magma ocean. Then, chemical segregation between the different terrestrial reservoirs resulted from the complex processes of mantle crystallization. These mechanisms were primarily controlled by thermal evolution of partially molten mantle. Partial melting however may still occurs today in different mantle regions. Evidences of low velocities zones (LVZ) in the upper mantle have been reported by different seismological and magneto-telluric studies, at a depth ranging from 80 km down to the 410 km seismic discontinuity. The reduction in seismic wave velocities reported is also consistent with the occurrence of partial melting. However, this matter remains the source of a vivid debate.

The experimental studies addressing melting of mantle materials show that the present-day temperature is not sufficient to induce melting of the bulk peridotitic or pyrolitic mantle, at all depths throughout upper mantle, transition zone and lower mantle. Melting can still arise in certain conditions, i.e. (i) in presence of significant amounts of volatile elements, such as water or CO_2, because it can decrease the melting temperature of silicate rocks by hundreds of degrees or (ii) for significant compositional changes, e.g. when the oceanic crust is subducted in the mantle.

In this study, we performed melting experiment on a homogeneous glass with chondritic composition, a proxy for the primitive Earth's mantle after core segregation. We performed *in situ* synchrotron X-ray diffraction and *in situ* impedance spectroscopy measurements to detect the onset of melting during the experiments in a multi anvil apparatus, at pressures up to 25 GPa, in order to determine the solidus temperature of the primitive upper mantle. Our results show that previous studies overestimated the solidus by approximately 250 K. The implication for a lower solidus are manifold. Firstly, partial melting could take place in the mantle today at lower temperatures than previously believed, especially when volatile elements such as H are present. The variation of the solidus temperature as a function of water content was therefore calculated using the cryoscopic relation reported in previous studies. Our results show that 500-600 ppm of water are required to depress the solidus temperature enough to cross the mantle geotherm at depths in which LVL are observed, which is compatible with the reported maximum water storage capability of the upper mantle.

Another major implication concerns the early state of the upper mantle. Mantle temperatures 200-300 K higher than today, as suggested from the composition of ancient non-arc basalts and komatiites, would induce partial melting at depths from ~200 to ~400 km. Thus, a shell of partially molten material could have persisted in the upper mantle for long geological times. Such weak layer could have decoupled the convection in upper and lower part of the mantle, possibly disabling the establishment of modern tectonic during the Archean. Then, upon secular mantle cooling, the final mantle crystallization at mid upper-mantle depths would have drastically modified the mantle dynamics, inducing global mantle convection.

In this work, the melting properties of the basaltic crust subducted in the lower mantle is also presented. Subduction of the oceanic lithosphere is thought to be a major responsible for mantle heterogeneities. At shallow depths, slabs undergo dehydration, which induces partial melting of the mantle wedge and arc magmatism. Still, the layered structure of the slab, formed by a ~2 km thick layer of MORB (mid-ocean ridge basalt) sitting on a depleted harzburgitic residue, can penetrate deep into the mantle, as evidenced by seismic tomography. The reason is that the enriched MORB material is denser than the surrounding mantle because of its higher Fe-content and its lower temperature. Injection of colder, denser and chemically different material in the deep lower mantle should affect its physical properties. By itself, it could affect the geophysical observables (e.g. seismic velocities, electrical and thermal conductivities) sufficiently to be detected from the Earth's surface. However, interpretations of the seismic signature remain controversial. In particular, seismic anomalies in compressional and shear velocities suggest the presence of some melt in the so-called ultra-low velocity zones (ULVZ) located just above the core-mantle boundary. We therefore explored MORB melting properties using *in situ* synchrotron X-ray diffraction in a laser-heated diamond anvil cell (LH-DAC), at pressures up to the 135 GPa found at the CMB. We observed an increase in the solidus temperature from about 2100(150) K to 3200(150) K at pressures from 20 to 80 GPa, respectively. At 80 GPa, which corresponds to a mantle depth of 1900 km, the MORB solidus is identical to that of a chondritic-type mantle. With further increase in pressure to 135 GPa, however, the MORB solidus temperature increases to 3800 K, while that of the mean mantle increases to 4150 K. The flattening of the MORB solidus could be linked to a change in liquid composition with pressure. Indeed, our data show a significant increase of the SiO_2 content in the melt with increasing pressure. We thus expect that the subducted basaltic slab should will undergo partial melting when reaching the lowermost mantle, producing a SiO_2-rich liquid that will eventually percolates and diffuses out of the slab into the lower mantle. Such liquid would react with the surrounding MgO-rich environment, producing bridgmanite (the major phase of the lower mantle) and thus favouring the "recycling" of the SiO_2-excess present subducted MORB, leading to a re-homogenization of the mantle.

RÉSUMÉ

Les processus de fusion ont joué un rôle clé dans l'évolution de la Terre. Au cours des premiers stades de la formation de la Terre, de grandes quantités de chaleur ont été libérées par (i) l'énergie gravitationnelle lors de la ségrégation noyau-manteau, (ii) la désintégration radioactive et (iii) les collisions entre corps orbitant autour du Soleil (en incluant l'impact géant qui a formé la Lune). Tous ces évènements ont conduit à la fusion du manteau et à des épisodes d'océan magmatique. Ensuite, les processus complexes de cristallisation du manteau ont conduit à la ségrégation chimique entre les différents réservoirs terrestres. Ces phénomènes ont été contrôlés par les propriétés de fusion des matériaux qui constituent le manteau.

La fusion partielle se produit encore aujourd'hui dans les différentes régions du manteau. Comme preuves, des zones de vitesses sismiques faibles (LVZ) ont été rapportées dans le manteau supérieur, pour des profondeurs allant de 80 jusqu'à 410 km, grâce à différentes études sismologiques et magnétotelluriques. La diminution de vitesse des ondes sismiques est compatible avec la fusion partielle du manteau. Toutefois, cette question reste la source de vifs débats. Les études expérimentales portant sur la fusion des matériaux du manteau montrent en effet que la température actuelle du manteau est insuffisante pour provoquer la fusion du manteau péridotitique (ou pyrolitique) dans le manteau supérieur. La fusion peut seulement se produire dans certaines conditions, à savoir (i) en présence d'une quantité importante d'éléments volatils, tels que l'eau ou le CO_2, car ces éléments diminuent significativement la température de fusion, ou (ii) pour des changements importants de composition chimique, par exemple pour de la croûte océanique subduite dans le manteau.

Dans une première partie de cette étude, nous avons effectué des expériences de fusion sur un verre homogène, de composition chondritique, comme analogue du manteau de la Terre primitive après la ségrégation du noyau. Nous avons effectué des études *in situ* de diffraction de rayons X et de spectroscopie d'impédance pour détecter les premiers stades de fusion. À l'aide d'une presse à multi-enclumes, nous avons reproduit des pressions jusqu'à 25 GPa en vue de déterminer la température de solidus du manteau supérieur primitif. Nos résultats suggèrent que les études précédentes qui utilisaient la méthode de la trempe ont surestimé le solidus d'environ 250 K. Les implications sont multiples. Tout d'abord, cela suggère que la fusion partielle pourrait avoir lieu plus facilement dans le manteau actuel qu'on ne le pensait initialement, en particulier lorsque des éléments volatils, tels que H, sont présents. Nous avons calculé l'effet de l'eau sur la température de solidus en fonction de la teneur en eau, en utilisant la relation cryoscopique. Nos résultats montrent que 500-600 ppm d'eau sont suffisantes pour abaisser la température de solidus jusqu'à la température actuelle du manteau. La présence d'eau dans le manteau pourrait donc expliquer les LVZ observées sismiquement.

Une autre implication majeure concerne l'état du manteau supérieur au cours de l'Archéen. Des températures mantelliques 200 à 300 K plus élevées qu'aujourd'hui, comme le suggère la composition d'anciens basaltes et de komatiites, induiraient la fusion partielle à des profondeurs d'environ 200 à 400 km. Ainsi, une couche de matériau partiellement fondu pourrait avoir persistée pendant de longues périodes géologiques au milieu du manteau supérieur. Cette couche aurait entraîné le découplage dynamique entre les parties supérieure et

inférieure du manteau, pour éventuellement inhiber la convection globale du manteau. Ensuite, avec le refroidissement séculaire, la disparition de cette zone partiellement fondue aurait pu induire, il y a environ 2.5 milliards d'années, une convection globale et la tectonique des plaques telle que nous l'observons aujourd'hui.

Un autre chapitre de cette thèse traite des propriétés de fusion de la croûte basaltique qui est subduite dans le manteau profond. Le devenir des plaques subduites reste méconnu, bien qu'elles puissent être responsables d'hétérogénéités dans le manteau. À de faibles profondeurs, la plaque subit la déshydratation, ce qui induit la fusion partielle du coin mantellique, et la mise en place du magmatisme d'arc. Pourtant, la structure en couches de la croute océanique, formée de basalte sur une épaisseur d'environ 2 km assis sur un résidu harzburgitique appauvri, peut pénétrer profondément dans le manteau, comme en témoigne la tomographie sismique. En effet, le basalte enrichi en fer est plus dense que le manteau qui l'entoure. L'injection dans le manteau profond de matière plus dense et chimiquement différente peut affecter les propriétés physico-chimiques de façon suffisamment importantes pour produire des hétérogénéités détectables par les méthodes géophysiques (vitesses sismiques, conductivités électriques, etc.). Toutefois, la signature des matériaux subduits n’est pas omniprésente et les interprétations demeurent controversées. Dans la couche D", située juste au-dessus de la frontière noyau-manteau, les mesures sismiques subissent indiquent une forte diminution des vitesses de cisaillement (ULVZ), ce qui a été interprété comme de la fusion partielle. La fusion partielle du manteau pyrolitique ne parvient pas à expliquer ces anomalies sismiques. Nous avons donc exploré les propriétés de fusion du basalte jusqu'à la pression de 135 GPa régnant à la CMB, en utilisant la diffraction X, dans une cellule à enclumes de diamant chauffée à l'aide d'un laser infrarouge. Nous avons observé l'augmentation progressive de la température de fusion au solidus, d'environ 2100 K à 3200 K, pour des pressions de 20 à 80 GPa. A la pression de 80 GPa, qui correspond à une profondeur de 1900 km dans le manteau, le solidus du basalte est similaire à celui du manteau moyen. Cependant, pour des pressions jusqu'à 135 GPa, la température de fusion du basalte augmente jusqu'à 3800 K, alors que celle du manteau augmente jusqu'à 4150 K. La fusion du basalte se produit donc à des températures inférieures, un effet qui pourrait être lié à un changement de la composition chimique du liquide avec la pression. Nos données montrent en effet une augmentation significative de la teneur en SiO_2 dans le liquide avec l'augmentation de la pression. La plaque basaltique subduite pourrait donc subir la fusion partielle dans le manteau inférieur et générer un liquide riche en SiO_2. Ce liquide finirait par percoler et réagir avec le matériau riche en MgO qui compose le manteau moyen. Ce phénomène pourrait faciliter le "recyclage" de basalte subducté par réaction chimique, et donc conduire à une ré-homogénéisation du manteau.

1. INTRODUCTION

The most widely recognised theory for the formation of the terrestrial planets in the early solar system states that planetary accretion takes place in three main stages, (i) the settling of a disk of dust and gas spinning around a young sun. This process takes place over timescales of thousands of years, in which the condensation of materials allow the (ii) merging of dust grains into km-size planetesimals. This leads to gravitational instabilities in different zones of the disk and runaway of the planetary embryos, triggering (iii) catastrophic collisions of planetesimals, resulting in the growth of larger planets. The energy released by such collisions would have been sufficient not only to raise the temperature of a proto-planet by thousands of degrees, but also most likely enough to create large molten pond across its surface. In the case of the Earth, it is crucial to highlight that such extensive melting events played a major role not only in the initial stages of accretion and differentiation of the planet, but also in the setting up the foundations to the mechanisms controlling the Earth's dynamics today. In the following paragraphs, therefore, we will investigate the melting processes that dominated the Earth's evolution, from its early stages to the present day.

1.1. CI Chondrite: a primitive Earth proxy

Our sun contains 99.9% of the mass of the solar system, and by analysing its chemical composition, we are able to infer the composition of circumsolar disk in the cooling nebula from which the planet embryos accreted. Yet, the composition of the planets today is widely heterogeneous, due to the mechanisms that segregated different elements in the early stages of planetary accretion. In order to investigate the processes that took place in the primitive Earth, we need to find a suitable composition. Meteorites offer us the opportunity to extend both of these dimensions. Meteorites are conventionally classified into three main groups, according to their structure, chemical and isotopic composition and mineralogy, namely (i) stony meteorites, mainly composed of silicate minerals, (ii) iron meteorites, largely composed of metallic alloys, and (iii) stony-iron meteorites that contain large amounts of both metallic and rocky material. Stony meteorites are then traditionally divided into two other categories, achondrites (meteorites that have been differentiated and chondrites. The formers represent meteorites originating from planetary bodies that have experience differentiation. Chondrites on the other hand are undifferentiated chemically primitive meteorites, having compositions (volatile elements excluded) very similar to that of the sun. Most chondrites in fact contain refractory inclusion enriched in elements such as Ca and Al (thus, calcium-aluminium

inclusions, or CAIs). These inclusions are the first, and therefore the oldest, object to condense from the nebular disk, and isotopic analysis have dated the oldest CAIs in chondrites at ~4.56 Ga (Amelin et al., 2002). Chondrites are divided in three main groups.

(i) Ordinary chondrites are more abundant than all other types of meteorites. They are chemically similar but differ in their contents of iron and other siderophile, and in the ratio of oxidized to metallic iron. Along with olivine, feldspar and diopside, common mineralogy of ordinary chondrite include Cr- and Ti-rich iron oxides, along with iron sulphides.

(ii) Enstatite chondrites take their name from their main mineralogy, i.e. enstatite ($MgSiO_3$). In these meteorites, iron is mostly found in its metallic form or in sulphides. They are in fact the most chemically reduced type of chondrite. A recent study proposes that enstatite chondrites could in fact represent the material from which the proto-Earth had formed, due to the mostly identical isotopic composition between E-chondrites and Earth (Boujibar et al., 2015). The authors report that the difference in Si/Mg ratio could be in fact due to collisional erosion of the early Earth proto-crust.

(iii) Carbonaceous chondrites are the most primitive and volatile-rich kind of chondrite. The high concentration of volatiles (such as water and organic compounds) in the majority of carbonaceous chondrites may suggest that since their formation such meteorites must not have be affected by high temperatures.

Classification of carbonaceous chondrites based on their compositions reflects the type of parent body from which they originated. Among carbonaceous chondrites, CI chondrites distinguish themselves for the absence of chondrules, as well as for having a chemical composition closely matching that of the Sun, with the exception of the most volatile elements. In particular, the concentration of oxygen, magnesium, silicon and iron in chondrites matches on a first approximation the proportion found in the Earth.

In the last years, however, several studies have attempted to solve a long lasting dispute on whether our planet share a common origin as chondrites. While comparing Earth's composition with that of the Sun or CI chondrites, in fact, one can notice few differences. First, the primitive Earth mantle, also referred to as bulk silicate Earth (BSE), is depleted of volatile and siderophile elements. The latter, even if they are refractory, are most likely depleted due to partitioning into the Earth's core. Moreover, Si/Mg ratio of the BSE is lower than is found

in chondrites. Several theories have been proposed to explain this, such as partitioning of Si into the core (Gessmann et al., 2001; Takafuji et al., 2005), or that the proto Earth did not accrete from the same material as chondrites (Drake and Righter, 2002).

Another issue revolves around the difference in the isotopic composition of the Earth compared to the solar ratio inferred from chondrites. Several studies have in fact observed that $^{142}Nd/^{144}Nd$ ratio measured for the Earth does not match the chondritic values, which conflicts with the idea that the BSE composition is chondritic (Boyet and Carlson, 2005; Campbell and O'Neill, 2012; Caro et al., 2008). The formation of a layer rich in incompatible elements and depleted in ^{142}Nd at a specific point in the Earth's early history has been proposed in order to explain this discrepancy. The presence of such layer in the deep Earth, however, does not reconcile with the heat transport from mantle plumes, hence alluding to the possibility that such layer could have been lost into space through collisional erosion. In both cases, a "missing" reservoir is needed to justify the chondritic origin of the Earth. In their recent work, however, (Burkhardt et al., 2016) disproven the need for such reservoir to explain the difference in radiogenic ^{142}Nd between BSE and chondrites. In their study, an enrichment in neodymium in the Earth's parental bodies through the process of nucleosynthesis is advocated as responsible for the discrepancy in $^{142}Nd/^{144}Nd$ ratios. Corrections for such process leads to a virtually identical ratio between BSE and chondrites, hence refuting the models from previous studies, and concluding that chondrites are indeed a suitable proxy for the Earth's composition.

We can therefore conclude that CI chondrites are most likely the best candidate to represent the undifferentiated protoplanetary material, reproduce the volatile depleted primordial composition of the terrestrial planets, in particular that of the primitive Earth.

1.2. Structure of the Earth

Uncovering the hidden mechanisms that control the Earth has been the main goal for geoscientists over the centuries. Even though we are unable to directly observe the mantle's mineralogy, information about the composition of the upper half of the mantle can be obtained from different sources. Peridotite, for example, is an ultramafic rock composed primarily by olivine (Ol), clino- and ortho-pyroxenes (Cpx, Opx), and garnet (Grt), that is carried to the surface as mantle xenoliths by the rising magmas, and it is the upper mantle's major constituent. Similarly, evidences of high pressure minerals similar to those present in the Earth's deep mantle can be found in meteorites, which are produced by shock-metamorphism due to the

high-velocity impact. Geological samples from the Earth's interior, however, are limited to just few hundreds kilometer in depth, which, compared to the whole extent of the Earth's interior, does not allow us to have a clear view of what is the mineralogy and the structure of the Earth up to its very core.

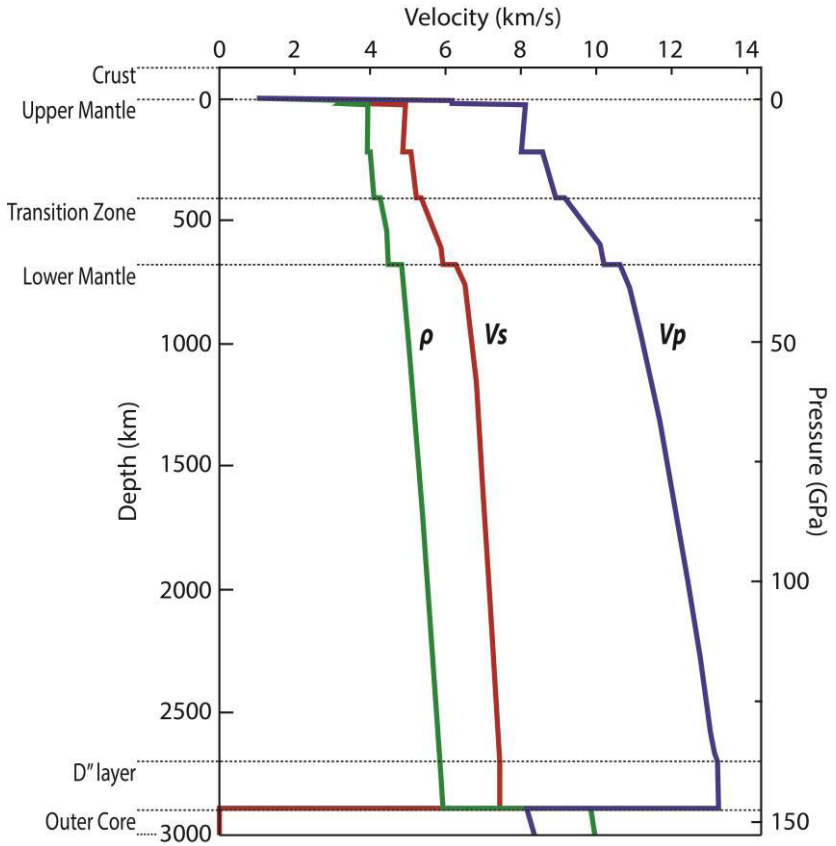

Figure 1.1. Preliminary Reference Earth Model (PREM).

A first Earth's interior subdivision, however, can be obtained from seismological and geophysical analysis (Jeffreys and Bullen, 1940). Such data have not only improved our knowledge of the Earth's structure, but they have also provided several fundamental information about the composition, the mineralogy and the elastic and dynamics properties of Earth's materials. At the planetary scale, the most important information we can obtain on the Earth's interior comes in fact from the measurement of seismic waves velocities. Seismic waves originating from earthquakes, would pass through the innermost parts of the Earth, refracting when encountering seismic discontinuities, and they would be recorded by seismograms at different locations around the globe. By analysing the seismograms, one can obtain major information on the Earth's geophysical properties, such as the location of seismic boundaries and different heterogeneities within the Earth. From the measured velocities of

compressional (primary, P) and shear (secondary, S-) waves through a media, we can in fact derive the density (ρ), and bulk (K_s) and shear (μ) moduli can also be inferred from P- and S-waves, respectively, using:

$$V_p = \sqrt{\frac{K_s + \frac{4}{3}\mu}{\rho}}$$

and

$$V_s = \sqrt{\frac{\mu}{\rho}}$$

From the analysis of the seismic waves velocities through the Earth, we can observe a number of discontinuity in the waves propagation, representing sharp changes in physical properties with depth. Many discontinuities in fact occur at conditions that correspond closely to the pressure and temperature of phase transformations known from experimental studies. Phase transformations also depend on composition, which means that seismic discontinuities can also constrain information on the chemistry of the mantle. Figure 1.1 shows one of the models describing the variation of seismic waves velocities, also known as PREM, Preliminary Reference Earth Model (Dziewonski and Anderson, 1981).

Some of the discontinuities observed from seismic analysis allow us to divide the Earth's mantle in three main domains, i.e. upper mantle, transition zone, and lower mantle (figure 1.2). The first sharp change in velocity gradient at 410 km corresponds to the phase transition of olivine $(Mg,Fe)_2SiO_4$, the most important paragenesis of the upper mantle (56-60% of its total mass) into wadsleyite (β-olivine). Wadsleyite would then transform into ringwoodite (γ-olivine) at 520 km, marking a smaller seismic boundary within the transition zone. The most important phase transition in the mantle is likely the one responsible for the seismic discontinuity observed at around 660 km. At such depth, ringwoodite decomposes into ferropericlase (Mg,Fe)O and bridgmanite, Al-$(Mg,Fe)SiO_3$. The most significant seismic anomaly in the lower mantle is the one defining the so-called D" layer (Kellogg et al., 1999). This ~200 km thick layer located above the boundary can be attributed to the phase transition from bridgmanite to post-perovskite, its high pressure polymorph (Murakami et al., 2004).

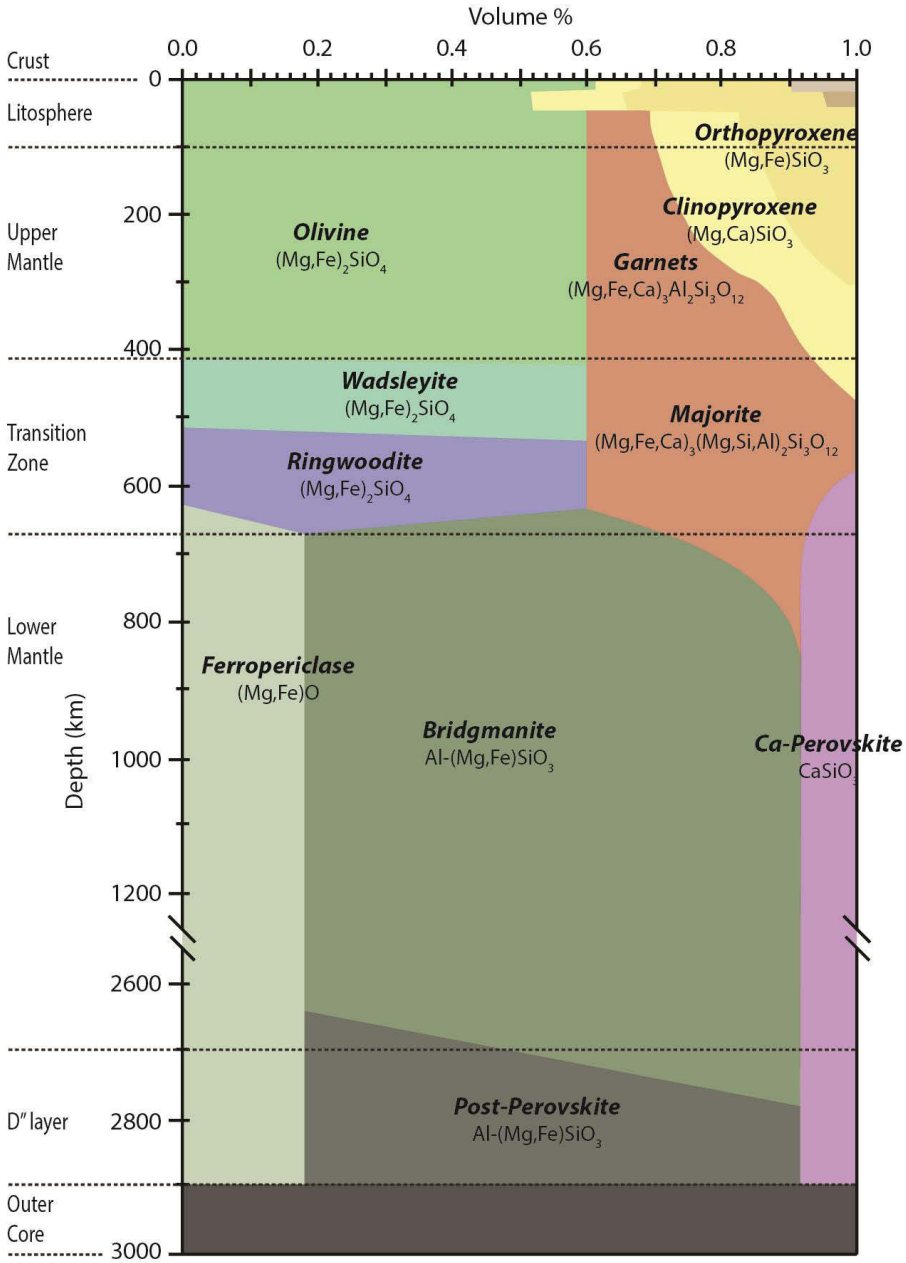

Figure 1.2. Earth's mantle mineralogy (modified from (Frost, 2008)).

1.3. Mantle Heterogeneities

1.3.1. Seismic anomalies in the upper mantle

Over the years, numerous studies have explored the nature of anomalies in the upper mantle (e.g. (Romanowicz, 1995a)). Seismic and magneto-telluric profiles of the oceans and continental regions present prominent anomalies, in particular at depths between 80 and 250

km, corresponding to a decrease of about 3–6% in S-wave velocity. This low-velocity zone (LVZ) occurs close to the boundary between the lithosphere and the asthenosphere in the upper mantle, with both depth and thickness varying from one tectonic environment to another. The presence of partial melting has since long been advocated as the main theory to explain the observations of such zones in the upper mantle (Anderson and Sammis, 1970; Lambert and Wyllie, 1970; Sato et al., 1989; Solomon, 1972; Thybo, 2006). At these depths, in fact, melts have been shown to be thermodynamically stable, due to the depression of the solidus temperature by the presence of fluids and volatiles (Hirschmann, 2010).

Recently, localized seismic and electrical anomalies have also been reported atop the 410-km mantle discontinuity (e.g. (Revenaugh and Sipkin, 1994; Song et al., 2004; Vinnik and Farra, 2007)), at different areas around the globe (e.g. Asia, north America, pacific and Africa). Recent seismological studies have shown that such low velocity layer (LVL) is actually not limited in specific isolated locations (Tauzin et al., 2010), but it can in fact be found globally atop the 410 km discontinuity, with thicknesses ranging from few tens of km to 200 km. The nature of the LVL is however still unclear. Lateral variations of the LVL thickness are in fact difficult to resolve as caused by a temperature variation, nor by variations in thickness of the transition zone boundary. On the other hand, several studies have concluded that the presence of partial melt is most likely responsible for the low-velocity layer (Kawakatsu et al., 2009; Mierdel et al., 2007; Tan and Helmberger, 2007), as thermochemical effect alone cannot explain the magnitude of the anomalies. (Bercovici and Karato, 2003a) in fact proposed that LVL may be caused by dehydration-induced melting, caused by upwelling mantle material (pushed up by the cold subducting slab) from the high-water-solubility transition zone into the low-water-solubility upper mantle. (Mierdel et al., 2007) presented experimental evidence that water storage capacity could have a minimum at depths corresponding to the seismically observed low velocity layer, concluding that water content in peridotite could indeed depress the solidus temperature enough to cross the geotherm, producing low degree of partial melting. Alternative mechanisms based on solid-state processes, such as anelastic relaxation or hydrogen diffusion (Karato, 2014; Priestley and McKenzie, 2013; Stixrude and Lithgow-Bertelloni, 2005) have been alternatively proposed. However, the recent finding of young (< 10 Ma) alkali basalt on the 135 million-year-old Pacific Plate (Hirano et al., 2006) provides strong physical evidences for partial melting in the asthenosphere.

Despite the great number of studies investigating the partial melting origin of the LVL, several major factors remain unconstrained. Namely, despite the fact pressures are well constrained at all mantle depths based on the density profile provided by seismology, our

knowledge on the mantle's temperature profile remains imprecise. Anchor points are provided by phase transformations in the major mantle minerals, which are responsible for the seismic discontinuities between 410 and 660 km depths. It yields a potential temperature (Tp) of ~1600 K, which corresponds to the extrapolation to the Earth's surface of the adiabatic temperature profile going through these anchor points (Katsura et al., 2010). Altogether, it happens that the mantle geotherm plots at significantly lower temperatures compared to the melting curve of the peridotitic mantle determined experimentally (see fire 1.3). Noticeable exceptions exist, for example at mantle ridges, where the uprising of hot mantle material can eventually melt when pressure is released at the approach of the Earth's surface. Nevertheless, if partial melting would indeed occur at mid upper mantle depths, volatile elements should be present to significantly lower the mantle solidus (e.g. (Hirschmann et al., 1999)).

a. Melting curves of the upper mantle/transition zone

Measuring the melting curves of the mantle is therefore a crucial step in understanding the nature of seismic discontinuities in the upper mantle. Several studies have pursued the task of experimentally determine the solidus of different mantle materials, in order to clarify whether melting is possible in upper mantle regions were seismic anomalies were recorded, particularly for the LVL (Figure 1.3). (Herzberg and Zhang, 1996; Zhang and Herzberg, 1994) performed melting experiments on anhydrous mantle peridotite KLB-1 at pressures between 5 and 23 GPa, using a large volume apparatus. Their results show that melting could occur in an anhydrous upper mantle only for mantle temperatures hotter than those of the present-day. The comparison between different studies on natural peridotites at both low (Hirschmann, 2000; Walter, 1998) and high pressures (Tronnes and Frost, 2002), with the present day geotherm (Katsura et al., 2010) also showed that melting of dry mantle material is unlikely to take place in the upper mantle today. The same kind of result was found for synthetic CMAS-pyrolite under anhydrous conditions, up to 25 GPa (Litasov and Ohtani, 2002). In their study, however, the authors also performed melting experiments on the same sample under hydrous conditions (2% H_2O). They observed a significant depression of the solidus temperature in hydrous experiments, concluding that dehydration melting of rising wet material from the transition zone up to the base of the upper mantle could in fact be possible.

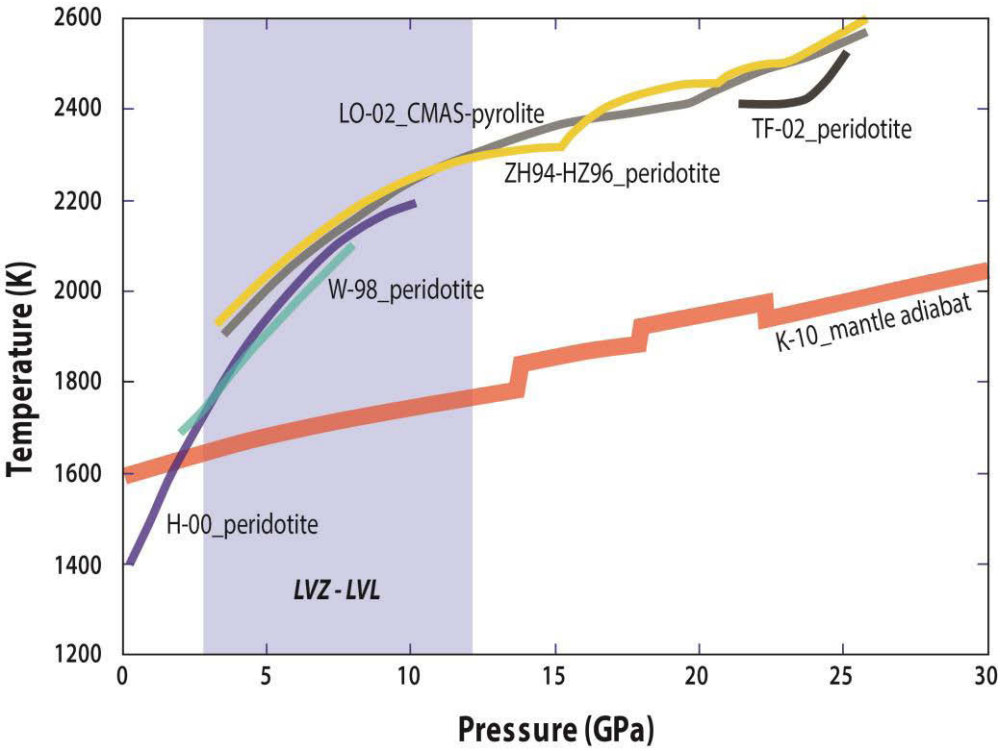

Figure 1.3. Solidus curves of different mantle materials compared to the present day mantle adiabat. ZH94-HZ96: (Herzberg and Zhang, 1996; Zhang and Herzberg, 1994); W-98: (Walter, 1998); H-00: (Hirschmann, 2000); LO-02: (Litasov and Ohtani, 2002); TF-02:(Tronnes and Frost, 2002); K-10: (Katsura et al., 2010).

b. Effect of volatiles on melting curves

The results of (Litasov and Ohtani, 2002) showed that hydrous conditions influences the solidus of the mantle. In their study, however, the amount of water required to justify the presence of partial melt at the depths in which the LVL are reported is significantly greater than the maximum water storage capacity of the mantle, reported to be not greater than 1000 ppm at such conditions (Ferot and Bolfan-Casanova, 2012). Their results, however, opened a question that is crucial in solving the question around the partial melting-nature of the LVL. How much do volatiles (such as water and/or CO_2) influences the melting temperature of the mantle?

The presence of carbon in the mantle is apparent not only form the occurrence of carbonate in mantle xenoliths, but also from the existence of ultra-deep diamonds (Pearson et al., 2014). Experimental studies on melting of carbonated periodotites below 20 GPa (Figure 1.4), have clearly shown that the presence of CO_2 has a quite drastic effect on the solidus temperature of the mantle (Dasgupta and Hirschmann, 2010; Litasov and Ohtani, 2009; Litasov et al., 2014). The presence of carbonated melt may therefore generate seismic low-velocity zones in the upper mantle (Dasgupta and Hirschmann, 2006). Such conclusions are supported

by electrical conductivity measurements of carbonated melts, which show that the high conductivity observed in the oceanic asthenosphere could be explained by a small degree of carbonated partial melt (Gaillard et al., 2008). Carbonated fluids, however, might not be ubiquitously distributed in the upper mantle, in contrast with the observations of a global distribution of the LVL.

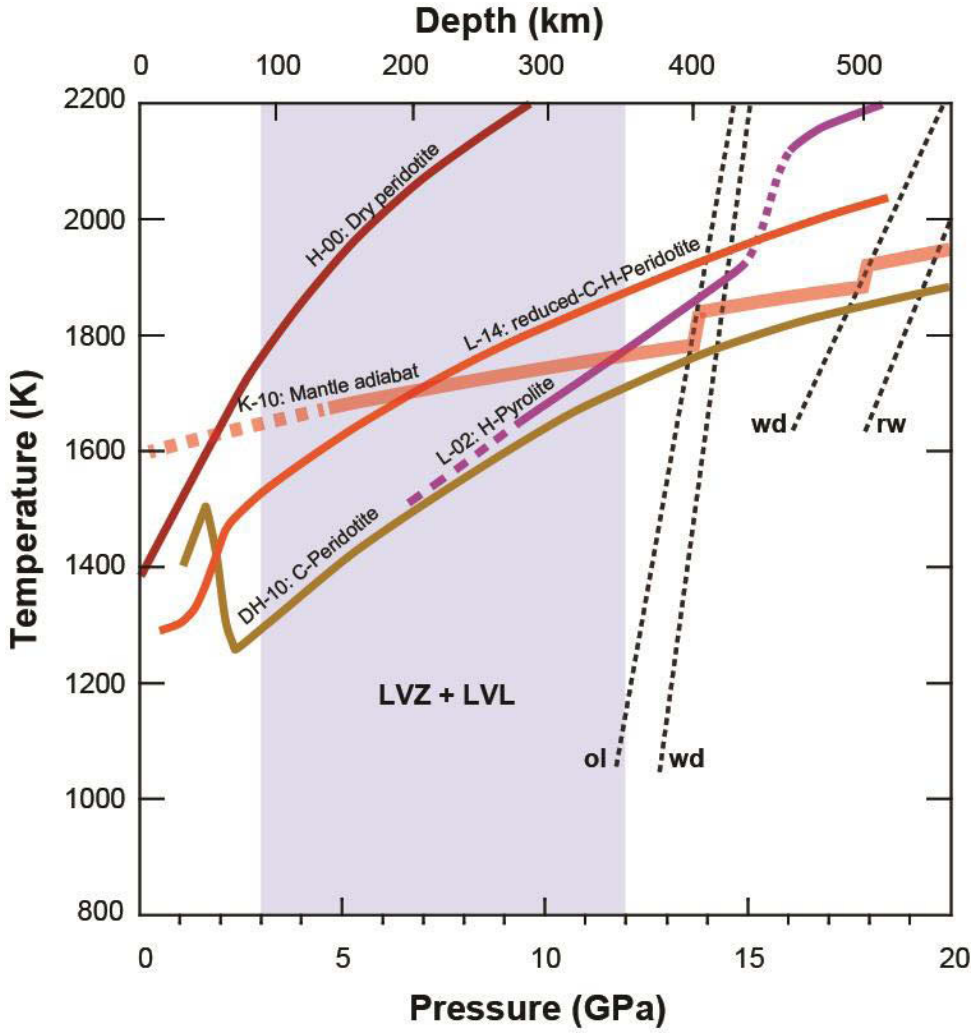

Figure 1.4. Comparison between different mantle solidi for "dry" peridotite (H-00, (Hirschmann, 2000)) and other reports with presence of volatile elements in the experimental charges, in relation to the mantle adiabat (K-10, (Katsura et al., 2010)). Nominally anhydrous carbonated peridotite (DH-10: C-Peridotite (Dasgupta and Hirschmann, 2010)); Pyrolite with 2wt.% H2O (L-02: H-Pyrolite (Litasov and Ohtani, 2002)); Peridotite with a reduced C-O-H fluid (L-14: reduced-C-H-Peridotite(Litasov et al., 2014)). Dashed grey lines represent the phase transitions between olivine (ol), wadsleyite (wd), and ringwoodite (rw), including depth intervals for the progressive transitions. The purple shadow region corresponds to mantle depths where seismic anomalies have been reported.

Water, on the other hand, is well known to be more abundant in the upper mantle than carbon, and since H can be stored as a defect in nominally anhydrous minerals (Ferot and Bolfan-Casanova, 2012), water can easily be present in anomalously high amount in parts of the mantle that are otherwise considered dry. Several studies have investigated the effect of water on the melting properties of the mantle (Green et al., 2014; Novella and Frost, 2014). The concentration of water in the mantle necessary to depress the solidus temperature enough to cross the mantle geotherm and cause a sufficient amount of melt to explain the seismic observations at the LVZ, however, has still not been successfully defined. A number of studies have tried to use a so-called "cryoscopic relation" (see Methods) based on experimental determination of water solubility in silicate melts to model the depression of the solidus in the mantle (Aubaud et al., 2004; Hirschmann et al., 1999), but the lack of experimental data available for partitioning coefficient limit the suitability of such model beyond the transition zone.

c. Melting in the early Earth's mantle

Within the first 100 million years of the Earth's history, the giant Moon forming impact (MFI) melted Earth almost entirely (Nakajima and Stevenson, 2015). Release of energy induced by gravitational segregation of the impactor's core could have potentially heated the Earth's core by 3500–4000 K above the temperature reached prior to giant impact (Herzberg et al., 2010; Nakajima and Stevenson, 2015; Rubie et al., 2015). It could have led to a CMB temperature on the order of 6000 K (Davies et al., 2015; Labrosse, 2015; Nakagawa and Tackley, 2010), which is well above the mantle solidus of ~4150 K. Therefore, MFI could have caused intensive melting at all mantle depths. There are geochemical evidences, however, that the accretion processes and MFI did not induce complete chemical homogenization of the Earth's mantle. For example, excesses in ^{182}W (produced by the decay of ^{182}Hf) measured in 2.7 Ga-old komatiites require a large-scale magmatic differentiation during the first 30 Ma of the Solar system's history (Touboul et al., 2012). Same conclusion arises for the difference in Xenon isotopic composition between MORBs and the Iceland plume (Mukhopadhyay, 2012). Geodynamical arguments also suggest presence of an unmixed and primordial material in the deep mantle (Davaille, 1999; Kellogg et al., 1999). Therefore, it is unlikely that the primordial mantle temperatures were above liquidus at all mantle depths. Low viscosity of magma-ocean is expected to induce vigorous and turbulent convective flows, which favour a homogeneous mixing. In the meantime, heat flux at the magma ocean surface could have been as high as ~106 W/m2, which suggests its crystallization within ~103 years after MFI (Solomatov, 2007).

Longer time scale are also possible, due to eventual formation of an opaque atmosphere at the Earth's surface or other geodynamical complications, such as physical or chemical mantle layering, etc. (Hamano et al., 2013; Lebrun et al., 2013; Sleep et al., 2014; Zahnle et al., 1988). On the other hand, petrological analyses of Archean and Proterozoic basalts preserved at Earth's surface show primary magma compositions compatible with Tp only 200-300 K greater than today (Herzberg et al., 2010). A similar temperature change is reported between Archean tonalite-trondhjemite-granodiorite associations of 4.0 to 2.5 Ga old (Martin and Moyen, 2002). This modest increase of mantle temperature compared to the present situation suggests a relatively rapid mantle cooling just after the MFI. In the lowermost mantle, it has been suggested that a basal magma ocean (BMO) could have lasted for very long times, billions of years, in correlation with an outer-core temperature significantly higher than the mantle solidus (e.g. (Labrosse, 2015)). This issue remains largely opened, however, because geodynamical models do not explain what could prevent such a hot core from rapid cooling (Monteux et al., 2016; Nakagawa and Tackley, 2010). We note that the gravitational descent of mantle melts to the CMB could have facilitated the persistence of a BMO (Nomura et al., 2011). Such layer may still be present at the base of the mantle, thus explaining the seismological anomalies called ultra-low velocity zones (ULVZ) detectable today by seismic observations (see chapter below).

d. Aim of this study

Previous experimental studies addressing the melting of the upper mantle report solidus temperatures much higher than the present-day temperature profile (e.g. (Katsura et al., 2010; Litasov and Ohtani, 2002)). Thus, the dry peridotitic or pyrolitic mantle compositions should not encounter melting in the upper mantle. Melting could still take place in the mantle if certain conditions are fulfilled, i.e. (i) presence of significant amounts of volatile elements, such as water or CO_2, because it decreases the melting temperature of silicate rocks by hundreds of degrees 3 or (ii) for significant compositional changes, e.g. when the oceanic crust is subducted in the mantle (e.g. (Andrault et al., 2014; Martin et al., 2014)). However, the lack of precision concerning the previous experimental determination of the solidus temperature at the upper mantle conditions may affect our understanding of the melting behaviour. Previous studies, in fact, used the so-called “quench method”. This technique based on the analyses of recovered samples, where the first low-degree of partial melting could be difficult to detect due to fast sample recrystallization upon cooling (e.g. (Laporte et al., 2004)). This could lead to an over-estimation of the solidus temperatures.

In this part of my PhD thesis, we will determine the mantle solidus temperature with two independent in situ techniques, X-ray diffraction and electrical conductivity measurements, at pressures and temperatures up to ~25 GPa and ~2500 K using multi anvil apparatus. These in situ techniques are sensitive to the presence of small amount of melt in the sample and they allow monitoring the sample behaviour at wide temperature range.

Our newly measured solidus will be compared to the temperature profile of the upper mantle, and we will discuss the implications the presence of water in the upper mantle. Using the cryoscopic relation ((Hirschmann et al., 1999), see Methods), in fact, we will determine the amount of water necessary to deplete the solidus enough to cross the geotherm, and determine whether the nature seismic anomalies such as the LVL atop the 410 km discontinuity can be attributed to the presence of volatiles-induced partial melting.

We will use our original data of the chondritic upper mantle solidus to discuss the thermal evolution of the early Earth in relation to the presence of partial melting, and in particular the effects that crystallization of a partially molten layer would have on the geodynamics of the mantle in the Archean-Proterozoic age.

1.3.2. Ultra-low velocity zones at the CMB

Seismological studies have observed the presence of ultra-low velocity zones (ULVZ) in specific locations in the mantle just above the core-mantle boundary (CMB), characterized by a decrease in P- and S- wave velocities of 10 and 30%, respectively (Garnero and McNamara, 2008; Lay et al., 2004; Stutzmann et al., 2000; Wen and Helmberger, 1998; Williams and Garnero, 1996). Their size is limited to just about 100 km wide, and few tens of km in thickness, and their density have been found to be about 10% higher than the surrounding mantle. ULVZ may truly be laterally discontinuous, rather than representing the thicker portions of an otherwise ubiquitous thin layer, but the existence of a very thin ULVZ-like layer spanning the entire CMB cannot be ruled out.

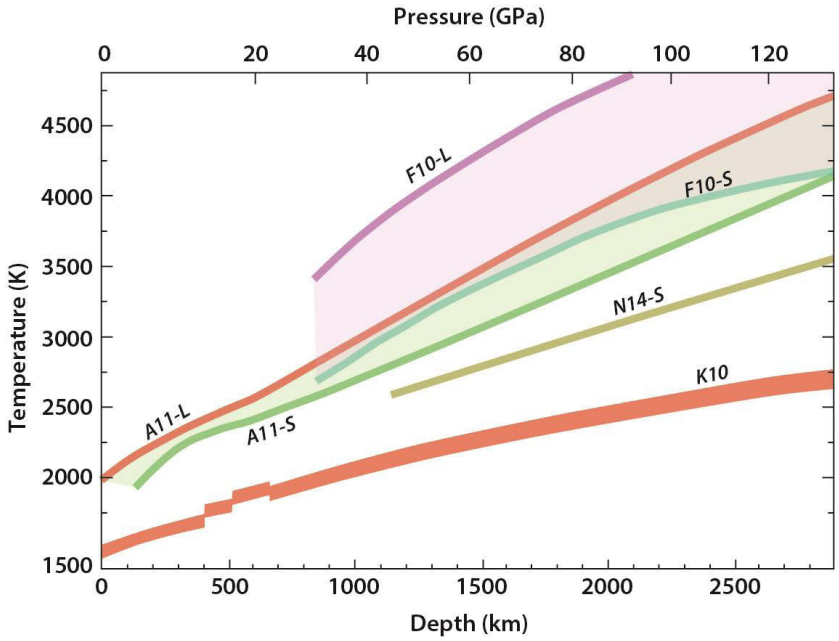

Figure 1.5. Solidus (S-) and liquidus (L-) curves for different lower mantle compositions, together with the present-day mantle adiabat (Katsura et al., 2010). F10: (Fiquet et al., 2010); A11: (Andrault et al., 2011b); N14: (Nomura et al., 2014).

Despite being reported in several regions across the CMB, it is still unclear whether ULVZ exhibit the same characteristic ubiquitously (Thorne and Garnero, 2004). Their observation has generally been interpreted as being an outcome of the presence of partial melting due to the steep temperature gradient at the CMB. A degree of partial melting between 5 and 30% could in fact decrease P- and S- seismic wave velocities to a similar value as that reported for ULVZ (Rost et al., 2005). In their study, however, (Thomas and Asimow, 2013) concluded that the ambient mantle cannot produce a partial melt in equilibrium with a residue that is sufficiently dense to be compatible with the observed ULVZ. Moreover, solidi determinations of pyrolitic, peridotitic and chondritic mantle, show that partial melting is not likely to happen in the mantle today, as melting temperatures are much higher than the present-day geotherm (Figure 1.5) (Andrault et al., 2012; Fiquet et al., 2010; Nomura et al., 2014; Nomura et al., 2011). Alternatively, partial melting in the D" layer could eventually be induced by a change in the chemical composition of the mantle. A local concentration of incompatible elements (Na, K) and/or volatiles (H_2O, CO_2) could in fact have a moderate effect on the solidus temperature. Another hypothesis involve the presence of a basal magma ocean enriched in incompatible elements (Labrosse et al., 2007). At the present, however, the most likely explanation for the nature of the ULVZ is that they represent compositionally distinct material, probably iron enriched, which may or may not be partially molten. Sinking of particularly

dense melts from the mantle above and accumulation at the CMB could provide a source for melting that is chemically diverse from the surrounding mantle, thus explaining the ULVZ in the D” region.

2. METHODS

Understanding the deep structure and the composition of our planet is the main goal of Earth's scientists. Seismology is the most reliable tool to investigate the inaccessible part of the Earth. However, even if the study of the propagation of the seismic waves through the Earth allows us to identify the presence of discontinuities through the Earth, such important approach cannot explain by itself the origin and the nature of such discontinuities. Therefore, in order to understand the behaviour of different materials at conditions typical of the Earth's interior, high pressure and high temperature experiments have become the most important tool in mineral physics. Throughout the years a number of high pressure devices have been developed, such as diamond anvil cell (DAC) and multi anvil apparatus (MAA). In both DAC and MAA the smaller the compressed area (so called pressure chamber), the higher the resulting pressure. DACs have a smaller pressure chamber than MAAs (an advantage to reach higher pressures) but they employ smaller samples. Usually, a typical size of a DAC sample is some tens of μm^3, whereas that of a MAA experiment is up to few tens mm^3. Through the years, geoscientists have tried to develop new types of both MAAs and DACs, in order to extend the range of pressure and temperature achievable, but still preserving a relatively large size of the samples.

2.1. Sample preparation

Oxide	Chondritic mantle (wt.%)	Pyrolite (wt.%)
SiO_2	48.1	45.1
TiO_2	0.2	0.2
Al_2O_3	4.0	3.3
Cr_2O_3	0.3	0.4
FeO	7.2	8
MgO	34.0	38.1
CaO	5.7	3.1
Na_2O	0.5	0.4

Table 2.1. Composition of our starting material.

Our sample consisted in a mixture of oxides with composition typical of the chondritic mantle after core segregation (see Table 2.1). We used two different compositions, with or without Fe, in order to test the effect of Fe on the melting curves. No trace elements were added to the mixture. Their effect on the melting curves is believed to be negligible, since they do not partition strongly to the melt and instead preferably enter Ca-rich phases (Corgne et al., 2003).

Powders were initially grinded to a homogeneous mixture in an agate mortar for approximately 1 hour.

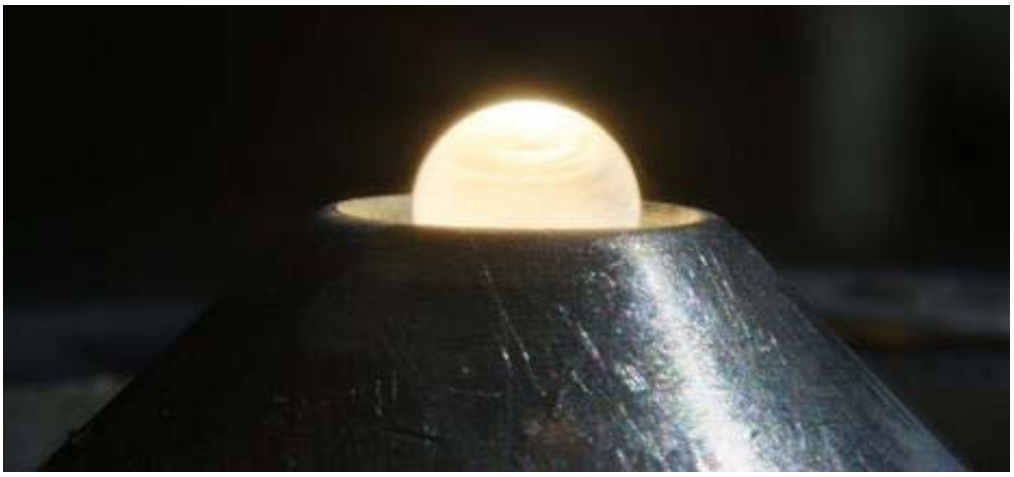

Figure 2.1. Close-up of the molten glass sphere levitating on the aluminium nozzle (Credit: Oak Ridge National Laboratory).

Starting powders were molten into glass spheres of ~2.5 cm in diameter, using the high temperature aerodynamic levitation system at the laboratory Conditions Extrêmes et Matériaux: Haute Température et Irradiation in Orléans (France). This containerless method uses a regulated gas flow, through a conical nozzle below the sample, eliminating completely any contact between sample and container and thus, preventing any contamination. The oxide powders were first pressed in a pellet die with a load of 6 tons. Weighted pieces of these pellets were melted for a few minutes at a temperature above 2000°C in an aluminium nozzle, giving a spherical shape to the sample (Figure 2.1). Then the samples were quenched down to room temperature in few seconds with a maximum cooling rate of 500°C/s. In order to obtain reduced and oxidized atmospheres the levitation chamber can either first evacuated and further filled with pure Ar with less than 0.05 ppm of oxygen, however the vessel remained opened to air during the synthesis at high temperature. This prevents for the formation of metallic Fe at very high temperatures when using a reduced atmosphere. A description of the complete laser-heating levitation procedure can be found in ((Hennet et al., 2006); (Hennet et al., 2011)). The recovered glass spheres were polished in the shape of a cylinder that can be directly inserted into the capsule of the high pressure assembly. Such starting material provides consistent advantages when performing studies of the melting behaviour. Firstly, the presence of moisture at the surface of the grain is decreased drastically. Moreover, chemical homogeneity is ideal in the glass, compared to the intrinsic heterogeneities typical of the mixtures of powders.

The key diffusive length scale for equilibration is micron scale of the grains. Achievement of such equilibrated textures, including documentation of well-developed triple junctions devoid of melt or excess phases (see for example, (Davis et al., 2011)). It seems rather logical that the scale of heterogeneity will be smaller at the solidus temperature when starting from an homogeneous glass rather than from a mixture of powders with an initially broad distribution of grain scale. When our glass recrystallizes, it produces nanograins first that do not achieve a size larger than a micron until we reach the solidus. This is shown in our SEM images (see figure 2.14). We note that in previous studies (e.g. (Herzberg et al., 2000b)), the grain size of the initial powder is not mentioned. It demonstrate that the kinetic effects, in particular the grain to grains diffusion, was not taken into account in this previous study.

Table 2.2 provides a list of the experimental runs performed in this work, for both synchrotron X-ray diffraction experiments and in situ electrical conductivity measurements. Pressure *P(GPa)* is the experimental pressure at the onset of melting. T_{obs} is the raw experimental temperature when the melting criterion is observed. ΔT_{grad} is temperature correction for presence of thermal gradients in the cell assembly (see figure 2.3). ΔT_{H2O} is the temperature correction for presence of 90 ppm water in the sample (see figure 2.16). $T_{Solidus}$ is the true solidus temperature. T_{cryst} is the temperature at crystallisation of the glassy starting material is observed. *Phases* is the list of minerals present in the sample, as refined from the X-ray diffraction patterns (see figure 2.12). *Oli*, *Gt* and *Wad* stand for olivine, garnet and wadsleyite, respectively.

X-ray diffraction							
Exp. #	P(GPa)	T_{obs} (°C)	Δt_{grad}	ΔT_{H2O}	$T_{Solidus}$(K)	T_{cryst}(K)	Phases
MA2_05	1	1130	80	36	1519	1250	Gt, Oli
MA2_05	11.6	1630	80	47	2030		Gt, Oli
MA2_06	4.7	1430	80	40	1823	1473	Gt, Oli
MA2_07	9.8	1608	80	45	2006	1500	Gt, Oli
MA2_08	17.4	1750	80	52	2155	1600	Gt, Wad
MA3_08	1.4	1211	80	36	1600	1173	Gt, Oli
MA3_09	7	1444	80	42	1839	1273	Gt, Oli
MA4_01	9	1520	80	44	1917	1550	Gt, Oli
MA4_02	16	1703	80	51	2107	1500	Gt, Wad
MA4_03	24	1860	80	55	2268	1573	Gt, MgO
MA4_04	13.5	1660	80	49	2062	1385	Gt, Oli
Electrical Conductivity							
LMV-157	5	1472	80	40	1865	1373-1573*	
LMV-183	5	1447	80	40	1840	1373-1573*	
LMV-170	5	1447	80	40	1840	1373-1573*	
LMV-171	5	1422	80	40	1815	1373-1573*	
LMV-172	5	1422	80	40	1815	1373-1573*	
LMV-285	20	1777	80	55	2185	1373-1573*	

Table 2.2. Summary of the experimental run performed in this study. * During conductivity experiments, onset of sample crystallization was observed below 1273 K. Then, the temperature was keep constant between 1373 and 1573 K for ~3h.

2.2. Multi Anvil Experiments

During the last 50 years, a number of different MAAs have been used in high pressure and high temperature experiments. From the Bridgman anvil (developed in 1952 and used by Ringwood to observe the olivine-spinel transformation (Ringwood, 1970) to the 6/8 Kawai-type multi anvil (Kawai and Endo, 1970), the evolution of such devices passed through many stages. We can distinguish between three main MAAs, i.e. tetrahedral, cubic and octahedral types, corresponding to the geometry of the system. Each type has a precise number of anvils (4, 6 and 8, respectively) and a different polyhedral pressure medium (cubic, tetrahedral and octahedral, respectively). In the so-called Hall's tetrahedral apparatus (Hall, 1958), four tungsten carbide anvils compress simultaneously four faces of the tetrahedral pressure medium (usually pyrophyllite), and, at room temperature, a maximum pressure of ~12 GPa can be reached (Ito, 2007). Today, the most used large volume apparatuses are the DIA-type multi anvil and the 6/8 Kawai-type multi anvil. In the DIA-type MAA (cubic geometry) six so-called primary-stage anvil (made of either hardened steel or tungsten carbide) are driven along three opposite directions perpendicular to each other, compressing a cubic high pressure medium. Since pressure generation in the DIA-type MAA is usually limited to approximately 10 GPa, a second stage anvil system can be implemented to achieve higher pressure (see later). A modified version of the cubic geometry large volume press is the D-DIA (deformation-DIA) MAA, which allows us to drive independently two of the six primary anvils, in order to create a non-hydrostatic stress and to apply a controlled strain rate to the sample. In the Kawai-type MAA (also known as split cylinder-type), the force is applied simultaneously to 8 inner cubic anvils (tungsten carbide, synthered diamond, polycrystalline diamond) by 6 outer anvils, usually made of hardened steel or tungsten carbide. When implementing a secondary stage system, a corner of each cube has been truncated in order to create a triangular face with a precise edge length (TEL, truncation edge length). The cavity generated by the eight truncations is the vessel of the pressure medium. The pressure medium is usually made of semi-sintered MgO-5%Cr_2O_3 ceramic, although other ceramic material, such as zirconia or pyrophyllite, are sometimes used. During compression, the pressure medium edges are extruded into the space between the anvils. This determines non-hydrostatic conditions inside the pressure chamber. In order to prevent such problem, a lateral supports for the pressure medium is used. The support, called gasket, should be made of a softer material than the pressure medium (e.g. pyrophyllite).

2.2.1. Electrical conductivity experiments

a. High-pressure assembly

Electrical conductivity measurements were performed using the 1500-Tons 6-8 split cylinder Kawai-type multi anvil apparatus operating at the *Laboratoire Magmas et Volcans* (Clermont-Ferrand, France). Quasi-hydrostatic pressures of 5, 10 and 20 GPa were provided by compressing octahedral pressure medium with edge length of 18, 14 or 10 mm between 8 tungsten carbide cubic anvils which edges truncated to 11, 8 or 4 mm, respectively. The sample pressure estimations were was based on room temperature pressure calibration of Bi (2.55, 7.7 GPa), ZnS (15.6 GPa), GaAs (18.3 GPa) and GaS (22 GPa) (Bean et al., 1986) and at high temperature using the phase transformation of quartz to coesite (Bose and Ganguly, 1995), $CaGeO_3$ garnet to perovskite (Susaki et al., 1985), coesite to stishovite (Zhang et al., 1996), forsterite to wadsleyite (Katsura et al., 2004), wadsleyite to ringwoodite (Suzuki et al., 2000) and majorite to perovskite (Hirose et al., 2001). The error in pressure determination at high temperature is of about 0.5-1 GPa.

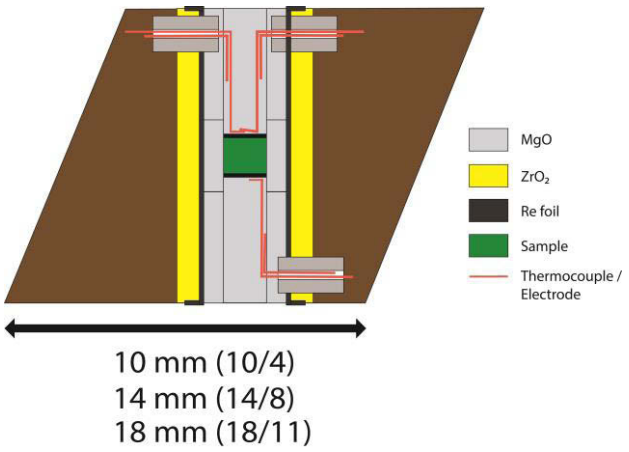

Figure 2.2. Schematic drawing of the high pressure assembly for electrical conductivity experiments.

A schematic view of our sample assembly is shown in Figure 2.2. We used octahedra made of semi-sintered MgO with 5% Cr_2O_3, which encompasses the interesting properties of low thermal conductivity, low electrical conductivity and high melting point. A ZrO_2 cylindrical sleeve was placed around the heater to enhance thermal insulation. The heater was made of a 50 µm thick rhenium foil folded into a cylindric shape and inserted within the ZrO_2 sleeve. Re provides very stable heating for temperatures up to more than 2273K. We kept

sample length to less than 1mm, in order to reduce the effect of temperature gradient during heating.. A cylindrical sleeve of MgO is inserted between the heater and the sample to (i) prevent chemical reactions with the Re heater, (ii) insure the electrical insulation of the sample and (iii) contain the sample upon melting.

The sample temperature was measured using type C thermocouple (W5%Re-W26%Re). Diameter of thermocouple wires were adapted the size of the octahedra (50 µm for 18/11 and 14/8, and 30 µm for 10/4 assemblies). The thermocouple was positioned on one side of the assembly. We added a third W5%Re wire on the other side of the cylindrical sample to allow measurements of the sample impedance. The Re disks placed either side of the sample facilitate the electrical connection between the sample and the electrode wires.

b. Temperature gradient

Because the temperature determination is major in this study, it is crucial to estimate the thermal gradient in our sample. We modelled the cell assembly used for electrical conductivity measurements based on the finite element method (Hernlund et al., 2006). The schematic cut of ¼ of the high pressure assembly was modelled for thermocouple temperatures between 1473 and 2273 K (Figure 2.3).

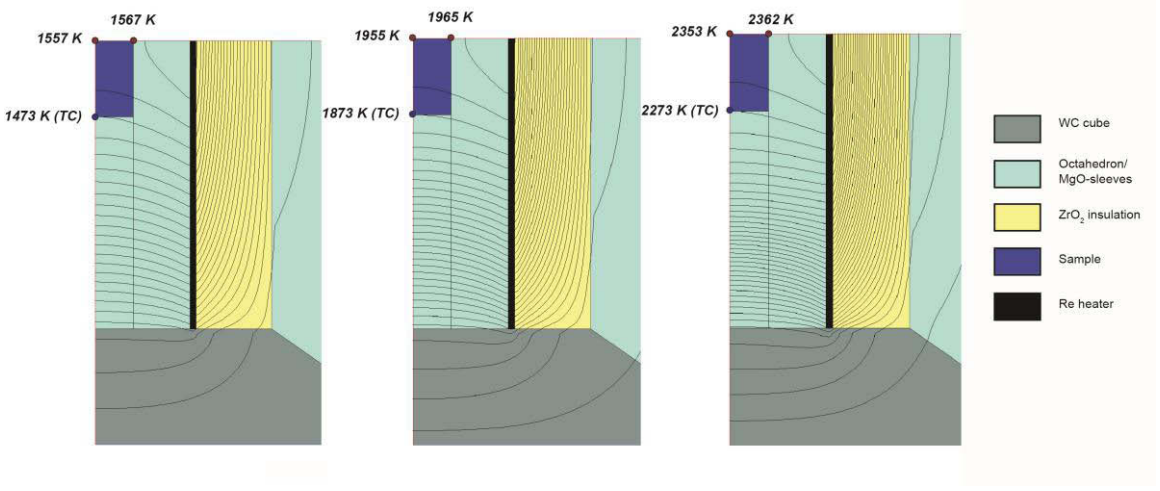

Figure 2.3. Thermal gradient simulations for the 18/11 mm assembly and for thermocouple temperatures of 1473 (left), 1873 (centre) and 2273 K (right). The sample size is 1.5mm (only half of its size is drawn here). The difference between the thermocouple reading and the sample temperature remains constant at 80 K.

As expected, the hottest part is found at the centre of the sample (extreme top-left position). The limited distance between sample and thermocouple (TC, blue dot) is achieved thanks to the penetration of thermocouple wires at the centre of the cylindrical Re-furnace (See

figure 2.2). Each temperature contour (thin black lines) represents a temperature interval of 50 K. In all simulations, the temperature difference (ΔT_{Simul}) between the sample centre and the thermocouple does not exceed 100 K. In this work, we apply a temperature correction ΔT_{Simul} to all our temperature measurements (see Table 2.2).

c. In situ impedance spectroscopy method

Impedance spectroscopy (IS) is a very well-known method of characterizing many of the electrical properties of materials, and it is an ideal technique in experimental petrology to monitor the evolution of a sample during experiments, since it can be used to investigate the changes in the conductance of solids (due to e.g. chemical reactions, defects, compositional changes). Generally, impedance spectroscopy is used to measure the total opposition that a material presents to a current flow when applying alternating (AC) signals of varying frequency. IS provides both a magnitude and a phase (|Z|, θ), and it can be described by a real and an imaginary component (Z', Z"). It is given by

$$Z(\omega) = Z' - jZ",$$

where Z(ω) is impedance as a function of frequency for alternating current, j is √-1, $Z' = |Z|cos\theta$ and $Z" = |Z|sin\theta$. The phase angle (θ) can be obtain from $\theta = tan^{-1}(Z"/Z')$. Impedance spectroscopy measurements are usually carried out by applying a single-frequency voltage (or current) to the interface and measuring the phase shift and amplitude (or real and imaginary parts) of the resulting current at that frequency.

Impedance data are plotted in the complex impedance plane (Z', $Z"$) as semi-circular arcs and the sample's resistance can be ideally given by the intersection between the real impedance Z' and the arc itself. Impedance arcs are characterized by a relaxation time ($\tau = R \times C$), and they are related to one or more distinct conduction processes taking place at a specific frequency range. Generally, a basic impedance arc is generated by an electrical circuit where a resistor is in parallel with a capacitor (RC circuit). In the case of a polycrystalline material, the single impedance arc is characteristic of conduction through the grain interior (Figure 2.4). In many cases however, since transport properties in polycrystalline solids are strongly affected by microstructure, and impedance spectra usually contain features that can be directly related to microstructure, a more complicated pattern can be observed when data are plotted in the complex impedance plane. A perfect example is given by the asymmetry of the

arc in complex plane, which is ideally centered on the real axis, but can be frequently displaced below it. This can be due to the presence of microstructures in the sample, which generally can result in the presence of multiple arcs at higher frequencies. Such complex datasets can be solved using the equivalent circuit model by replacing simple capacitor with a constant-phase-element (CPE). Equivalent circuits are electrical circuits made of resistors and capacitors in arrangement, which respond with frequency in the same manner as the sample. Each part of the circuit represents different processes taking place either in the sample. In their work, (Roberts and Tyburczy, 1991) provided an ideal example of a simple equivalent circuit, composed by three resistor-capacitor (RC) circuits. This RC circuit translate to the complex plane as three impedance arcs, corresponding to three distinct conductions media in the sample: conduction through grain interior (first arc), conduction through grain boundary (second arc), and reactions taking place at the sample-electrode interface (third arc), from the highest to the lowest frequency, respectively.

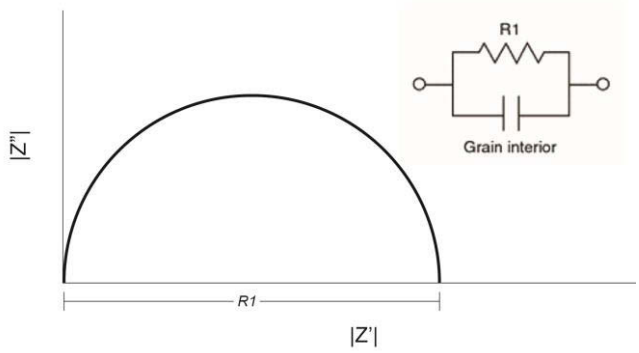

Figure 2.4. Schematization of a resistor-capacitor circuit representing conduction through grain interior in a polycrytalline material, and its representation on the complex impedance plane.

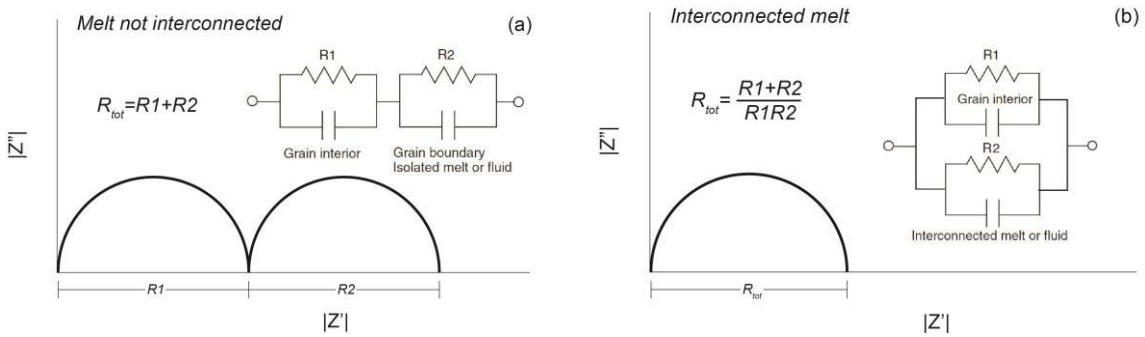

Figure 2.5. Schematization of IS models for melting experiments. (a) represents a model at the onset of melting, at a melt fraction low enough for melt to be stable in isolated pockets at the grain boundaries. (b) illustrate the change in conduction mechanism as soon as melt will interconnect within the sample.

d. Electrical conductivity measurements

Electrical conductivity was determined using impedance spectroscopy method in the frequency range of 10^{6} -10^{1} Hz (Figure 2.6). Insulation resistance (detection limit) of the assembly at similar pressure-temperature conditions was determined prior to the actual experiments. Polycrystalline samples are characterized by a combination of resister- / constant phase element (R-C/CPE) circuits and the resistance can be obtained by fitting the impedance spectra to appropriate equivalent circuits. Once the sample resistance is determined, conductivity can be calculated using the sample diameter and length measured after each experiment, assuming the sample geometry remained unchanged during the experiment using,

$$\sigma = \frac{l}{AR},$$

where l and A are sample length and area of the cross-section, respectively.

The activation enthalpy (ΔH) of each conduction mechanism can be obtained by fitting the data to Arrhenius equation, where σ is the electrical conductivity (S/m), T the absolute temperature, σ_0 the pre-exponential factor (S/m), and k the Boltzmann constant (J/K):

$$\sigma = \sigma_0 exp\left(\frac{-\Delta H}{kT}\right).$$

For each experiment, we performed a series of heating and cooling cycles, similar to previous works (e.g. (Manthilake et al., 2009), see figure 3.1.a). The low activation enthalpy observed in the first heating cycle below 573 K is likely to result from an extrinsic mechanism such as the presence of free protons. The adsorbed moisture in the assembly poses overestimation of the electrical conductivity due to current leakages through the surrounding ceramic components. We minimized such effects during our experiments by keeping the assembly at 500 K at desired pressure for more than 12 hours. While maintaining a temperature of 500 K, electrical resistance of the sample was measured at regular intervals until the sample resistance reached a steady value, often 1-2 orders of magnitude higher than the resistance measured at the beginning of the heating cycle. Sample resistance was usually measured in several heating-cooling cycles at temperature steps of 50-100 K until the heating and cooling paths were fully reproducible. Upon heating to higher temperatures, we observed a clear drop in the sample conductivity at around 1100 K, due to the glass transition in the sample. It induces the sample crystallization that was clearly observed during the *in situ* X-ray diffraction

experiments (see below, figure 2.10). The samples were kept between 1370 and 1570 K for ~3h, allowing the complete crystallization of initial glass, which is confirmed by the textural analysis of quenched experiments. Sample resistance was usually measured in several heating-cooling cycles at temperature steps of 50-100 K until the heating and cooling paths were reproducible. This minimizes the uncertainty of electrical conductivity measurements. Below the melting temperature of our sample impedance appears to vary exponentially with temperature with an activation energy of 1.02 eV (Figure 3.1.b, green line). This is typical of electron hole hopping between Fe^{2+} and Fe^{3+} conduction mechanism by small polarons (Yoshino, 2010).

For a nominal pressure of 5 GPa, we observed a clear change of slope in the conductivity profile at a temperature of ~1700 K, It can be interpreted as the onset of partial melting in the sample. At small melt fractions, the melt is likely found within grain boundaries and/or in isolated melt pockets and the total conductivity is weekly affected by their contribution. Thus, reaching the solidus temperature is not expected to produce a first order change in the overall sample conductivity. However, when temperature is further increased, progressive increase of the melt fraction induces more interconnection between the melt pockets. The conductivity is observed to increase up to ~10^2 S/m. At this temperature, the melt becomes the dominant conductive phase, interconnected between the two electrodes, with an ionic conduction mechanism (Gaillard et al., 2008). Similar evolutions of sample conductivity were already interpreted previously by the occurrence of an interconnected network of melt (Maumus et al., 2005; Partzsch et al., 2000; Sato and Ida, 1984).

As long as the sample is below solidus temperature, conduction will mostly happen through the grain interior (simple RC circuit, figure 2.4). At the onset of melting, however, isolated melt pockets will start to form within grain boundaries, and the sample electrical behaviour can be modelled by two RC circuit in series, one for conduction through grain interior and one for the contribution of the isolated melt pockets at the grain boundaries (Figure 2.5.a). The total resistance of the sample will therefore be equal to the sum of the individual resistances of the two circuits. With a melt fraction sufficiently high, melt pockets will interconnect within the sample, becoming the preferable medium for conduction. The sample can be modelled by two RC circuit in parallel (Figure 2.5.b), and total resistance is equal to the sum of the two resistances divided by their products.

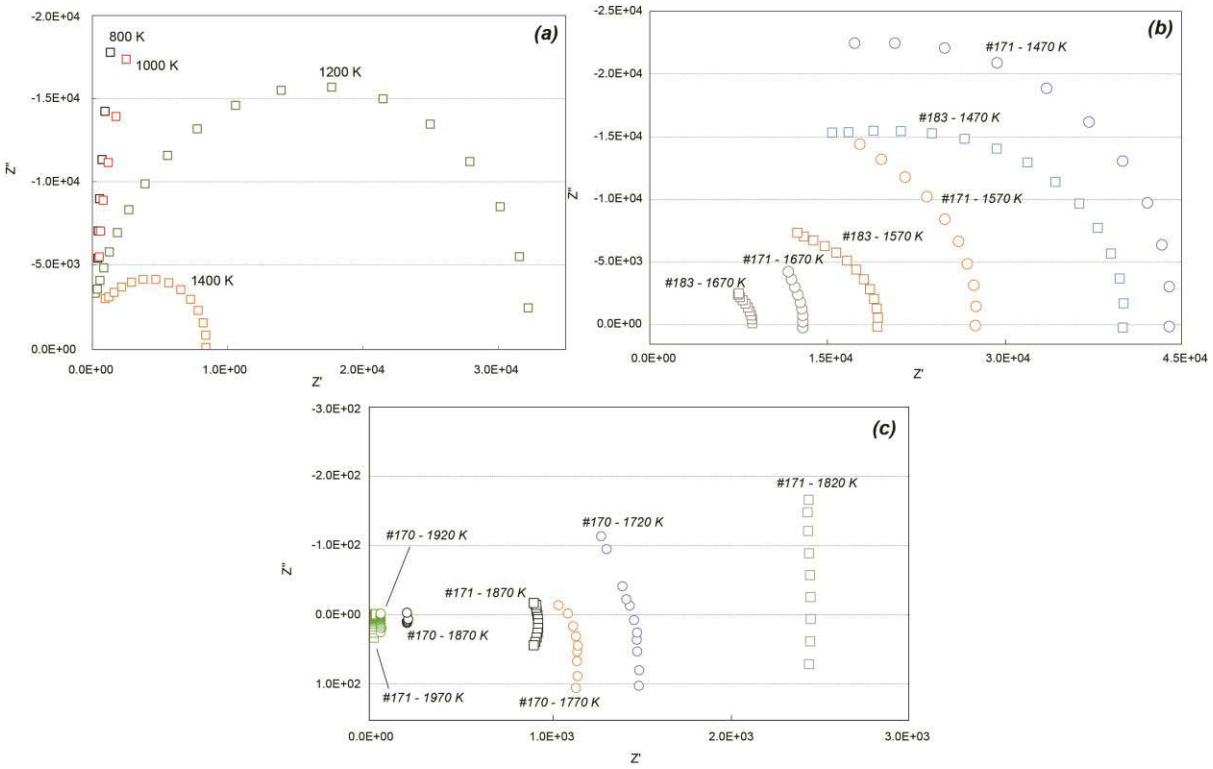

Figure 2.6. Impedance measurements performed at frequencies between 1 MHz and 1 Hz for chondritic samples **(a)** Low temperature conduction through grain interior modelled by simple RC circuit. **(b)** At solidus temperature, isolated melt pockets at the grain boundaries contribute to the total conduction in the sample, which can be schematized by RC circuits in series. **(c)** Once melt interconnect, very low resistances can be observed, and sample conduction can be modelled by a parallel circuit between the solid and molten sample fractions.

A typical impedance profiles obtained for chondritic samples during melting experiments is shown in figure 2.6. After compression, electrical conduction in our samples occurs through the grains interior, which can be modelled by as a simple RC circuit (Figure 2.6.a). Then, impedance appears to vary exponentially with temperature. Upon melting, electrical conduction also occurs through the melt pockets located at the grain boundaries. Insulated melt pockets could corresponds to a second RC circuit in series with that of grains interior (Figure 2.6.b). However, by further increasing the melt fraction, melt pockets eventually connect with each other, making the melt the predominant conductive phase (Figure 2.6.c). It yields the very low resistances observed at high temperatures. This behaviour can be modelled by a parallel circuit between the solid and molten sample fractions. During the measurement of impedance, these high-frequency low real Z arcs remain partial because of instrumentation limitations at high frequency.

2.2.2. Synchrotron X-ray diffraction experiments

In the interaction of an incident X-ray beam with the analysed material, some of the X-ray photon will be deflected from their original trajectory upon collision with electrons within the atoms. These scattered X-rays, carrying the information relative to the electronic distribution in the material, are what we study during diffraction experiments. Interaction between different diffraction waves can results in a constructive interference, where the intensity varies depending on the atomic arrangement. In the case of a crystal for example, where atoms are arranged in a periodic lattice, the intensity of the diffraction waves will reach maxima (so called "diffraction peaks") in correspondence to the location of the atoms in the crystalline structure. By collecting diffraction patterns of a material, one can therefore infer the atomic distribution in a material. The peaks in an X-ray diffraction pattern are directly related to the atomic distances, according to Bragg´s law

$$n\lambda = 2d_{hkl} \sin\theta$$

where n is the order of reflection, λ is the X-ray wavelength, d is the interplanar distance and the angle θ is the half of the so-called diffraction angle which represents the total deviation of the X-ray beam due to the diffraction process. The Bragg's law provides information on the inter-planar distances (d_{hkl}) and the relative positions of the planes. Such information permit to extrapolate the structure of the primitive cell. They, however, do not allow us to determine the position of the atoms in the cell, which can be extrapolated from the relative intensities of the peaks. The d-spacing of different lattice planes can be determined by angular dispersive X-ray diffraction (ADXD), which uses monochromatic X-radiation with a fixed λ, and records the diffraction rings on two-dimensional detectors from which different θ are measured. Energy dispersive X-ray diffraction (EDXD) an also be used to determine the interplanar distance, using a polychromatic (white) beam at a fixed angle, using a germanium detector to record patterns at different energies.

Powder X-ray Diffraction (XRD) is likely the most commonly used X-ray diffraction method used in the characterization of materials, which is generally in a powder form. This technique is based on the concept that the crystalline domain in the substance being analysed is randomly oriented. The recorded diffraction patterns will display the peaks corresponding to the d_{hkl} in the crystal structure. By analysing the position and the intensity of the peaks, one can then proceed to identify the phases in the material.

a. High-pressure assembly used for X-ray diffraction

In situ X-ray diffraction experiments were performed using the 1200 tonnes multi anvil press operating at PSICHÉ beamline in the SOLEIL synchrotron facility (Gif-sur-Yvette, France). To generate pressures up to 30 GPa, we used the DIA-geometry with secondary cubic anvils of 14 mm edges (Figure 2.7). High pressure assemblies consisted of cubes with 3mm truncation and 7 mm octahedron. We used similar assemblies than for electrical conductivity measurements, with octahedra made of semi-sintered MgO with 5% Cr_2O_3, a ZrO_2 cylindrical sleeve placed around the heater, itself made of a 50 µm thick rhenium foil. However, in this case, the Re furnace is horizontal (Figure 2.8), which allows an X-ray path parallel to the Re-tube. In order to supply current to the heater, two Re electrodes were place in contact with it. These donut-like electrodes are kept in position after folding several 500 µm long segments at the extremities of the heater, as shown in the drawing in figure 2.8. The glass sample was embedded into an MgO capsule, and its pressure during the experiments was determined based on the P-V-T equation of state of MgO, with an accuracy of about ~0.5 GPa at all P-T conditions.

Figure 2.7. Close-up of the 6-8 DIA set-up used for in-situ X-ray diffraction measurements in the Soleil synchrotron. The finger shows the X-ray path. The red wire is the thermocouple.

Electrical power to heat the Re-furnace was alternative current at 100 Hz frequency. Temperature was measured using a W/Re thermocouple touching the Re-furnace. The thermocouple signal was filtered to remove the common vibrating mode at 100 Hz. Consequently, the thermocouple emf could be measured up to the maximum temperature of 1700 K. We used gasket alternatively made of pyrophilite or a mixture of boron and epoxy.

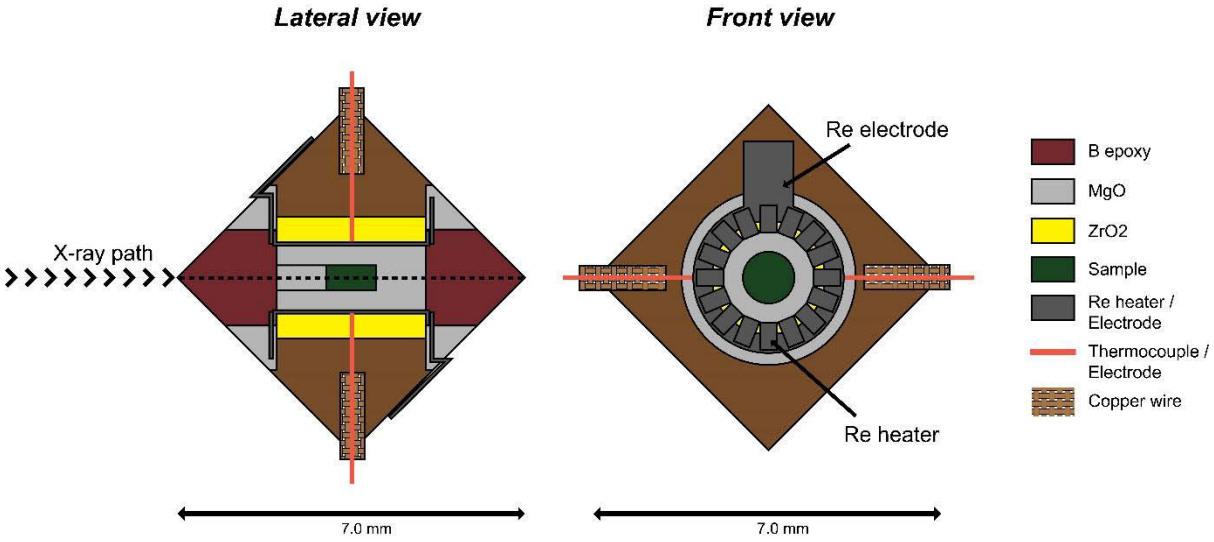

Figure 2.8. Schematic drawing of the 7/3 assembly used for X-ray diffraction experiments. The axis of the tubular Re furnace is parallel to the X-ray beam.

b. X-ray diffraction method

At the PSICHE beamline, an X-ray beam with energy range from 20 to ~100 keV is produced by an ondulator located on the synchrotron ring operating at 2.75 GeV. The whole X-ray flux is focussed vertically between the anvil gap of the MAA using a horizontal mirror located at 18.5 meters from the source and 4 meters from the sample. The resulting vertical FWHM of the beam at the sample position is approximately 20 μm, which corresponds to almost one order of magnitude flux gain compared to the unfocussed beam. The beam is collimated horizontally.

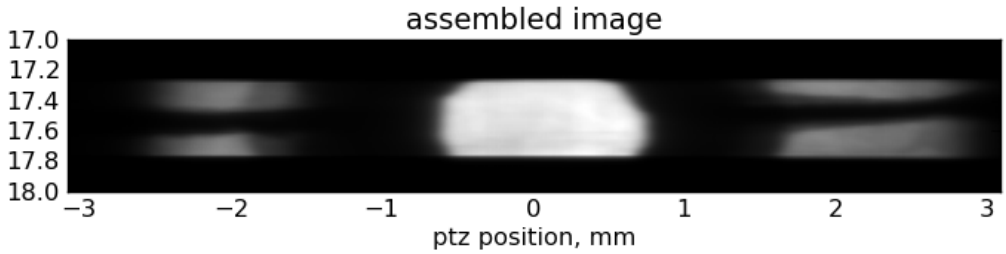

Figure 2.9. A typical X-ray radiography of our assembly after compression to ~15 GPa. The white circle at the center of the image corresponds to the tubular Re-furnace in which our sample is located. Further away from the sample after the Re-furnace (i.e. the darkest ring), the two wires of the W-Re thermocouple are clearly visible.

Two different modes where used: (i) samples were first aligned in the X-ray beam using X-ray radiography. For this, the press is scanned vertically in the X-ray beam, with the horizontal slits widely opened. The image is reconstructed numerically (Figure 2.9); (ii)

Diffraction was performed in energy dispersive mode using a Caesar-type diffractometer (Wang et al., 2004). A typical diffraction 2-theta angle of 8.0 degrees is convenient to register the major diffraction lines of our silicate samples. The best compromise between X-ray flux and resolution in d_{hkl} is achieved after the X-ray beam is collimated horizontally to a typical width of 50 µm, thanks to a system of slits located after and before the sample.

c. Crystallization in subsolidus conditions

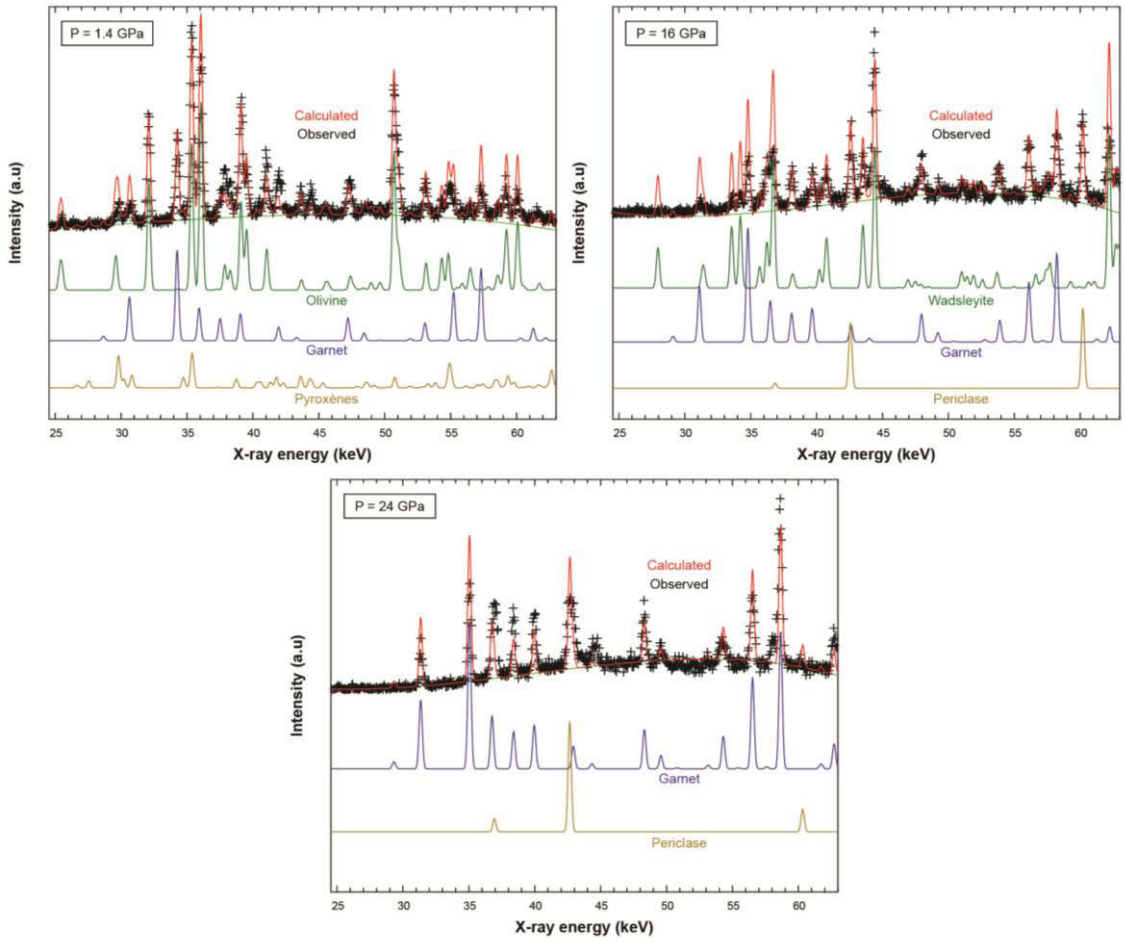

Figure 2.10. Example of diffraction patterns and the associated mineral contents. Experimental measurements (black crosses) are fitted using a Rietveld-type multiphase model (Red line). In this model, we fix the diffraction peaks intensities to the values expected from the atomic structure of each mineral. Only cell parameters and phase contents are adjusted. The theoretical model is the sum of the contributions of each phases (a sum of the yellow, blue and green profiles). Above the crystallization temperature, we could detect the mixture of olivine (or its high pressure polymorphs), garnet, OPx and/or CPx. Due to the limited sample size, diffraction peaks of the MgO capsule material arise sometimes. Higher pressures favour the dissolution of OPx and CPx in the majoritic garnet. At the maximum pressure of ~24 GPa, we observed a mixture of garnet plus ferropericlase, as previously reported for comparable sample composition (Litasov and Ohtani, 2002).

Upon heating, the sample temperature was maintained several minutes at 900 K to favour water loss in the transmitting media, to mimic the experimental procedure followed for electrical conductivity measurements. A sample crystallization becomes very fast at a sample temperature at least 300 K below the onset of sample melting (see Table 2.2). At this point, we wait several minutes to finalize grain growth, until no significant change is observed in any diffraction peak intensity between different patterns recorded at a few minutes interval. This evidences final sample crystallization (as evidenced from the analysis of the sample microstructure a posteriori, see figure 2.15), when the grain growth becomes extremely limited due to presence of grains with different compositions (i.e. the Ostwald ripening effect (Yamazaki et al., 1996)). At temperatures below the solidus, the absence of melt prevents sufficient atomic diffusion for additional grain growth in such multi-phasic system.

For each phase, the relative intensities between different diffraction peaks follow relatively well those theoretically calculated based on the atomic packing (Figure 2.10). Such achievement is typical of the absence of grains preferential orientation in a sample free of stresses. A noticeable feature is relatively lower intensities for diffraction peaks located at the lowest and the highest energies (i.e. highest or lowest d_{hkl}). This is due to absorption of low energy X-rays by the sample and the pressure medium, and an intrinsically limited amount of X-rays at high energies. For this reason, it is not possible to refine phase fractions of olivine (or its high pressure polymorphs), garnet and pyroxenes present in our samples. A second limitation is a relatively poor energy resolution in the Ge-detector. It favors peak overlapping and, for the case of minerals presenting numerous diffraction peaks, the identification of the minor phases is sometimes difficult. In particular, ortho- (OPx) and clino-pyroxenes (CPx) can be difficult to refine, while olivine (and its high pressure polymorphs) and garnet are always more visible. They are well-known limitations of the energy dispersive method. In contrast, this method enables acquisition of decent X-ray diffraction pattern every few seconds, which enables new criteria for the determination of the solidus temperature.

2.3. Diamond anvil cell (DAC)

Another essential tool to investigate matter at extreme condition is diamond anvil cell (DAC, figure 2.11). The principle behind the DAC is very simple. Pressure is defined as a ratio

of a force over the area over which it is applied. The smaller the surface (or the "anvil", in our case) in contact with the sample, the smaller is the applied force necessary to generate high pressure. Choosing the right material for the anvil, however, is the key to reaching extreme pressure. In fact, the anvil material should be hard enough, mechanically very stable, as incompressible as possible and it should not plastically deform during compression. The best material is single-crystal diamond, one of the hardest materials on Earth. The very high bulk modulus makes it perfect for high pressure experiments, and its transparency over a large range of wavelengths (from the ultraviolet up to the far infrared) allows us to use DAC with a wide range of in situ techniques, such as X-ray diffraction or X-ray fluorescence, for example.

In general, the central part of the DAC is composed by two gem-quality diamonds, which serve as pressure anvils on the sample. The three most common cuts used for anvils are a modified brilliant cut, Drucker standard cut, and Boehler-Almax cut. In our study, we mainly used Boehler-Almax conical diamond anvils. This design provides an optimised mechanical support for the anvil's crown section, and, compared to conventional anvils, offers a better alignment stability and a larger aperture. The tip of each diamond is truncated to form the so-called culet, an even surface that will compress the sample. The diamonds must therefore be perfectly aligned, and the culets parallel to each other, in order to avoid differential stresses on the sample during compressions. Diamond culet diameter can normally vary over a wide range, from 1 mm down to few tens of microns. In fact, the higher the desired pressure, the smaller the culet size and the sample volume. The diamonds are fixed by either epoxy, carbon glue or high temperature-resistant cement, on hard supports called seats, usually made of tungsten carbide. The seats can be moved by tightening a set of screws, in order to manually align the diamonds. The diamond alignment is probably the most crucial part of the cell preparation. The two diamonds must be aligned in the cell respectively to each other so that the two culets are facing each other perfectly. Any misalignment will cause the diamonds to fail at high pressure. It is important to first align the diamonds horizontally, matching the position of the two culets. A tilt alignment is then necessary in order to ensure that the culets are parallel to each other. The absence of interference fringes upon contact between the two diamonds indicates that the two culets are well aligned.

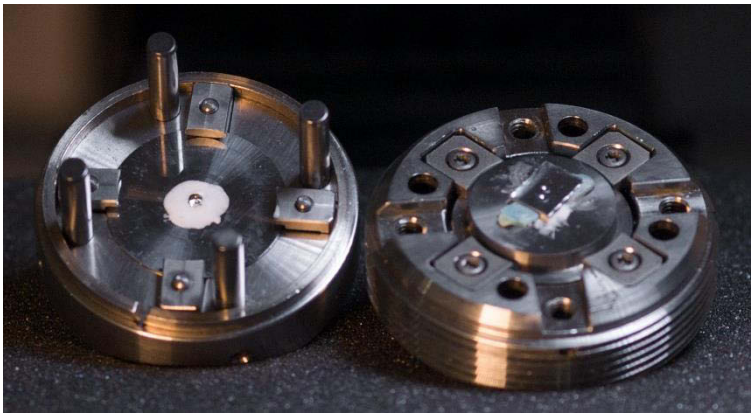

Figure 2.11. Picture of an opened diamond anvil cell (credit: ESRF)

In order to avoid contact at high pressure between diamonds and, therefore, their failure, a so-called gasket is place in the area between the culets. The gasket is usually a sheet of metal cut from a 250-300 μm foil of metal such as stainless steel, rhenium, or tungsten. The gasket material is chosen according to the type of experiment. In order to achieve the highest pressures, in fact, the gasket material should be as hard as possible but remaining compressible enough to allow the increase of pressure. Due to its very high melting temperature (above 3000°C), rhenium is the most commonly gasket material used to achieve extreme conditions.

By compressing the gasket between the two diamonds a pre-indentation is made, which supports the culets of the diamonds. Ideal pre-indentation thickness can range from ~30 μm up to ~50 μm. In the center of the pre-indentation, a hole is made either by spark erosion or by using a laser cutter, to form the sample chamber. The diameter of sample chamber is function of the culets size and target pressure. Ideally, the size of the hole ranges from one third to half of the culet size. Once the gasket is drilled, it is replaced into the DAC respecting its initial direction to minimize the risk of break diamonds at high pressure. The role of the gasket is in fact not only to laterally constrain the sample chamber, but also to support the diamond during compression and decompression. The diamonds will in fact deform largely at very high pressures, with the culets bending into a concave shape around the sample chamber, ultimately resulting in the formation of ring-cracks around the culet and, in many cases, in the breaking on the diamonds. In order to prevent the contact during deformation at high pressure, diamonds can be beveled by truncating the diamond edges at an angle. Usual inner culet diameter ranges from 50 to 150 μm, whereas external diameter is usually 300 μm. Beveled diamonds are usually adopted in order to perform experiments at Mbar pressures, as they reduce the risk of mechanical failure of the diamonds due to contact (Figure 2.12).

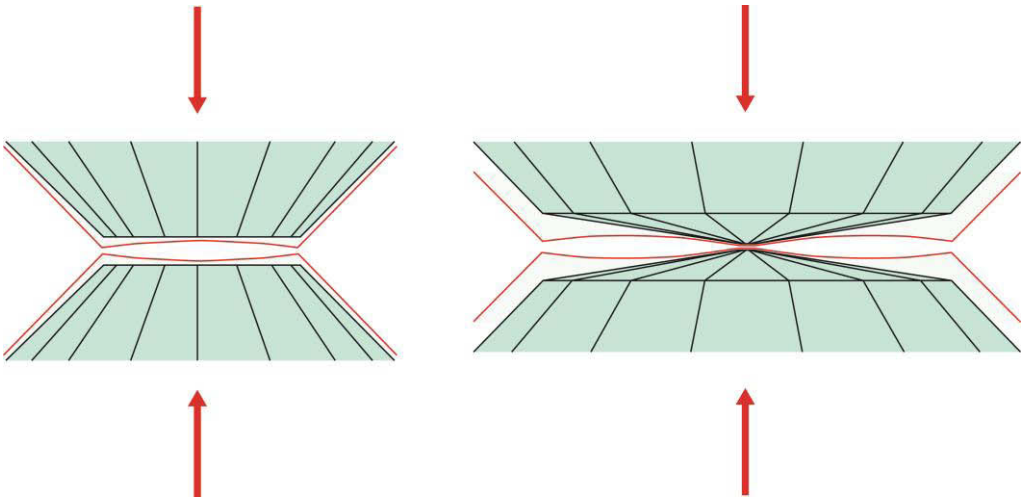

Figure 2.12. Schematic cartoon showing the deformation fo the culets upon compression. On the left, the edges of the culets in non-bevelled diamonds comes in contact at high pressures, resulting in ring-cracks and diamonds failure. Bevelled diamonds (right hand side), on the other hand, allow generation of much higher pressure, and reduce the risk of diamond failure at extreme conditions.

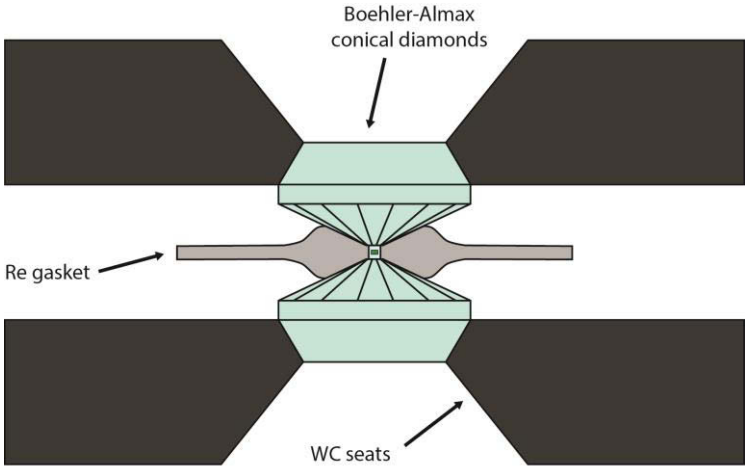

Figure 2.13. Schematic view of the Boehler-Almax diamonds with the conical crown design enclosing the Re gasket and the sample (in the center of the pressure chamber).

Once the hole that will form the pressure chamber is drilled and the gasket is placed back on the diamond, the cell is ready for the loading. The first step is load the pressure-transmitting medium. The pressure medium is required to obtain a (nearly) isotropic stress environment around the sample, and to prevent the gasket hole from collapsing around the sample. Ideally, in order to maintain a hydrostaticity during the experiment, the sample should be encased in a material that remains a fluid throughout the entire pressure range. Practically, perfect hydrostatic conditions are nearly impossible to achieve, and the choice of pressure-

transmitting medium depends on the nature of the experiments. Typical pressure media include liquids (methanol-ethanol or methanol-ethanol-water mixtures), soft solids (NaCl, KCl, KBr, etc), hard solids (MgO, Al_2O_3, etc) and rare gases (He, Ne, Ar, etc). The majority of our experiments were performed using KCl pressure medium, due to its extremely high melting point, which makes it ideal for melting experiments. Figure 2.13 offers a schematic view of the central part of the DAC, with the conical seats hosting the Boehler-Almax diamonds.

Different types of diamond anvil cells have been used during the last decades to perform high pressure experiments. In fact, because of its versatility, diamond anvil cell has seen many changes in the design through the years (see also review on EMU Notes n° 7: Mineral Behaviour at Extreme Conditions, 2005). The two most common designs, however, are the Merrill-Bassett-type design (Merrill and Bassett, 1974) and the Mao-Bell-type design (Mao and Bell, 1978). In the Merrill-Bassett design, the diamonds are mounted on triangular or circular plates, and compression is achieved by tightening screws. Even if the very simple design of the cell gives the possibility to have a better view of the central part of the sample, it does not provide a good alignment. In fact, when the screws are not equally tightened the seats with the diamonds will not be perfectly parallel, but slightly tilted. Such tilting determines differential stresses distribution on the sample surface during compressions, which can eventually end with diamonds failure. On the other side, Mao-Bell design provide a more strict control on the screw tightening. In fact, the alignment of the diamonds is ensured by the piston-cylinder system, in which one diamond is mounted on the hard metal cylinder. On the other side, the second diamond is mounted on a piston, which fit perfectly into the cylinder.

A variety of DACs in which the driving force is provided by inflating a steel membrane, rather than turning drive screws was introduced in the early 90s (Letoullec et al., 1988). In these "membrane DACs", the membrane is filled with pressurised gas, and, as it expands, it deforms its concave surface downwards, pushing one side of the DAC into the other, and pressing the diamonds together. The membrane DAC provides extremely accurate pressure control, and it is particularly advantageous since pressure can be changed remotely without dismounting the DAC from its support. This can be a great benefit for in situ experiments carried out at the synchrotron. Moreover, membrane cells are ideal when trying to reproduce the same pressurisation conditions in several experiments. These conditions can be difficult to achieve reproducibly using screw-driven DACs.

2.3.1. High temperature in the DAC

There are two major methods of heating in DACs, i.e. (i) laser heating and (ii) electrical resistive heating. In our study, high temperature experiments were performed using laser heating. The main advantage of this technique is that the sample can be heated to extreme high temperatures (>5000 K), still concentrating the heat only into a selected area of the sample, even at very high pressures. On the other hand, laser heating in the DAC presents some problems. Due to the very high temperature generated by the laser localized in a small area, an enormous thermal gradient, both vertically and horizontally, is produced throughout the sample. To minimize this thermal gradient, a double-sided laser heating system is normally used. Two types of laser are normally adopted, CO_2 or Nd:YAG, depending on the sample characteristic. CO_2 laser is very convenient for heating white oxides (e.g. MgO, Al_2O_3, etc.), due to the high absorption in the infrared region at the wavelength of 10.6 μm. Nd:YAG laser wavelength (1.06 μm), on the other hand, does not heat white oxides or compounds such as NaCl or KCl, as it interacts with the valence electrons of metals and transition elements, such as Pt or Fe in iron-rich silicate samples, and therefore is the preferred type of laser used in our study.

In laser-heating DAC (LH-DAC) experiments, the sample ideally needs to be thermally isolated from the diamonds. Diamonds are one of the best conductive material known, and without a proper thermal insulation, high temperature generation is made difficult by the heat transferred through the diamonds. The choice of the thermal insulator is therefore critical, especially during in situ X-ray diffraction experiments. Noble gases such are usually good pressure media (transparent, low thermal conductivity, chemically inert, simple diffraction pattern), but they presents problems at very high pressures and temperatures. Helium for instance, at high temperature starts to diffuse into the diamonds, causing catastrophic failure. KCl makes an excellent pressure medium for laser heating experiments, due to its transparency to YAG laser, its high melting point and its great thermal insulation properties.

Sample preparation is another key point in the success of a laser heating experiment. One must in fact use a proper thickness of sample to minimize the axial (parallel to the laser path) temperature gradient. Solid state chemical segregation by the effect of Soret diffusion can in fact be induced by the strong temperature gradient generated by the laser (Sinmyo and Hirose, 2010). Pressure was determined prior to LH based on the equation of state of KCl. A pressure correction of $0.5\ \alpha K \Delta T$ was performed to account for increase of pressure in the hot spot (Andrault et al., 1998).

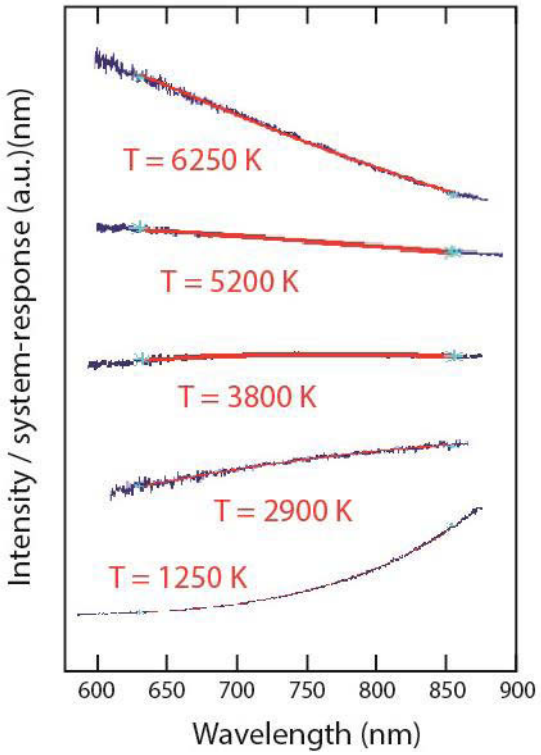

Figure 1.14. Thermal emission of the sample (blue) corrected to the system response and fitted by a plank function (red). The fits provide experimental temperatures with a precision of ±50 K.

Temperatures were determined on both sides of the sample from its thermal emission using reflective objectives with schwarzfield geometry. Such objectives prevent chromatic aberrations and allow temperature measurements up to more than 6000 K routinely (Figure 1.14). Temperature is measured by fitting the thermal radiation signals from the heated samples in a given wavelength range to the Planck radiation function assuming grey-body approximation with wavelength-dependent Planck emissivity. The system response is calibrated by a tungsten filament lamp with a known relationship between radiance and power setting.

2.3.2. In situ synchrotron X-Ray diffraction

Diamonds are almost transparent to X-rays, but the diamond support seats are usually not transparent, and the opening angle of seats and DAC limits the maximum 2θ angle. From Bragg's equation, it is obvious that short wavelengths should be used in order to observe the maximum number of reflections in the limited 2θ range. Synchrotron radiation sources have

many clear advantages with respect to conventional sources (e.g. X-ray tube). Firstly, the intensity of the X-ray beam is higher by several orders of magnitude, which allows very short exposure time (seconds) even for extremely small samples. Moreover, the wavelength can be tuned to the desired value and the X-ray beam can be strongly focused. On high-pressure diffraction beamlines such as ID27 from the European Synchrotron Research Facility (ESRF), a monochromatic X-ray beam of 0.3738 Å wavelength was focused using two Kirkpatrick-Baez mirrors onto a spot of less than 2*2 μm^2 at the sample position. Based on the optical image produced by fluorescence of irradiated KCl, the position of the entrance hole of the optical spectrometer used to measure the sample temperature was frequently adjusted on the position of the X-ray beam. Diffraction patterns were acquired using a MAR-160 CCD detector, before integration and analysis using the XRDUA (De Nolf et al., 2014) code.

2.4. Analytical techniques

2.4.1. Scanning Electron Microscopy

In the scanning electron microscope (SEM) a focused electron beam with an energy between 0.2 and 50 keV is scanned over the surface of a sample. The signal produces by the interaction between the electron beam and the sample is detected simultaneously to the scanning process, and it is displayed in form of a virtual image. When the accelerated beam electrons strike a specimen they penetrate inside it and interact both elastically and inelastically with the solid, forming a limiting interaction volume from which various types of radiation emerge. Among them, in this study we performed analysis using the followings.

(i) Backscattered electrons (BSE): they comprise the high-energy electrons reflected or back-scattered upon interaction with the sample. Elements with high atomic number will backscatter electrons more strongly than elements with low atomic number. This will results in a different in contrast between areas with different chemical composition.

(ii) Secondary electrons (SE): the secondary electrons are situated on the low end of the energy spectrum (<50 eV). They can either be electrons from the primary beam that have lost energy due to inelastic collisions, or electrons that originated from

the sample itself after interacting with the BSE. Due to their low energy, only electron close to the surface can escape, hence making the SE signal ideal for imaging the sample's surface.

(iii) X-ray fluorescence (XRF): the electron beam impinging on the sample's surface causes temporary charges in the electronic structure of the atoms, causing the electrons to jump into a different shell and then fall back into their original shell emitting characteristic X-rays. The X-rays can be recorded with energy-dispersive detectors (EDS) and the chemistry of the sample can be analysed.

The volume of interaction in which the incident electron beam interacts with the sample is controlled by the combined effect of elastic and inelastic scattering. The interaction volume is what determine the nature of imaging in the SEM, and it is influenced by a number of factors, namely the beam energy, the atomic number of the solid, the surface tilt, and the density of the solid. Overall, the interaction volume increases with increasing incident beam energy and decreases with increasing average atomic number of the specimen.

a. Textural and semi-quantitative analysis

In our study, we used a JEOL JSM-5910 LV SEM equipped with a PGT microanalysis system at the Laboratory of Magmas and Volcanoes, Clermont-Ferrand (France), and a Carl Zeiss SIGMA HD VP Field Emission (FEG) SEM with Oxford AZtec ED X-ray analysis operating at the University of Edinburgh (UK). Experimental charges were quenched at temperatures just below and just above (determined from the very beginning of change of slope in the conductivity curve) the onset of melting, in order to probe the textural evolution. The recovered samples were cut in two along the furnace axis using a diamond wire saw. Half of the sample was embedded in epoxy and polished to a mirror-like surface. Each sample is then coated with a thin layer of conducting material, typically carbon, using a low vacuum sputter coater machine. Creating a conductive layer of metal on the sample inhibits charging, reduces thermal damage and improves the secondary electron signal required for surface imaging in the SEM. Working conditions vary with the goal of analysis, and several parameters can be adjusted in order to provide optimal settings for the task, primarily the accelerating voltage of the electron gun, the working distance (WD), and the size of the objective aperture

Textural analysis with FEG-SEM were performed at high (15 kV) accelerating voltage and small WD (6 or 10 mm), yielding a smaller spot size, higher resolution, and, generally, a better BSE signal. These conditions are ideal to detect small features in samples that

encountered the lowest degree of partial melting, such as very thin films of melt along grain boundaries and nanometer-size melt pockets at the triple junctions (Figure 2.15). At subsolidus conditions after several hours of annealing, the homogeneous glass starting material has crystallized into grains of several microns and polygonal shape (Figure 2.15.b). Sharp grain boundary angles, often close to 120°, and linear grain boundaries in between junctions, evidence good textural equilibrium (e.g. (Laporte et al., 2004)).

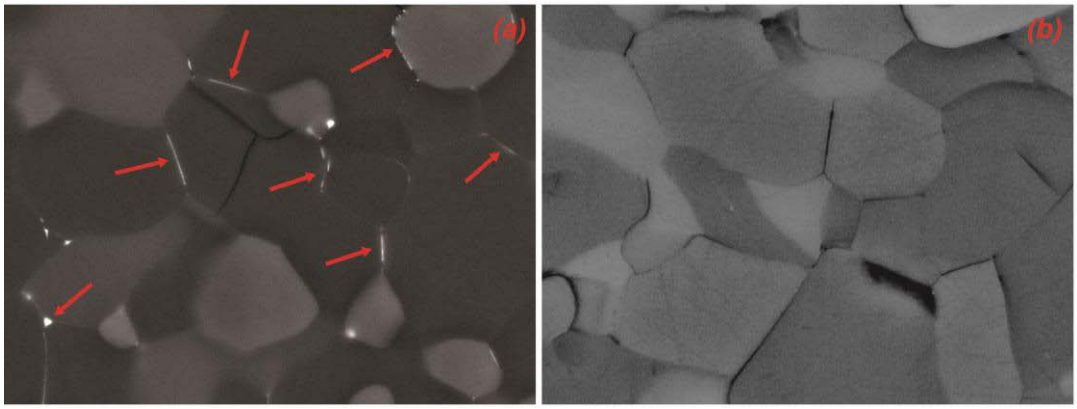

Figure 2.15. FEG-SEM images of two samples recovered after heating experiment **(a)** just above and **(b)** just below the solidus temperature. In both cases, pressure was 5 GPa.

Above the solidus, we observe melt as very thin films and nanometer-size pockets at triple junctions (Figure 2.15.a), as typically observed in partially molten systems (e.g. (Yoshino et al., 2010). These features are typical of very low degree of partial melting (e.g. (Hirose and Kushiro, 1993)). When quantifying the fraction of the sample surface covered by the melt (the most shiny regions), it correspond to a degree of partial melting of less than 0.5%.

Finally, we used the EDS detector to record chemical maps of the samples, from which we could verify their mineralogical content (Figure 2.16.a, 2.16.b). An intimate mixture of olivine, clinopyroxene, orthopyroxene and garnet minerals can, for example, be refined in a sample quenched from 5 GPa (Figure 2.16.d). Semi-quantitative chemical maps were generally recorded at a WD of 20 mm, to allow more X-rays (emitted by fluorescence) to reach the detector. In several cases, energy was lowered to 5 kV in order to obtain a good spatial resolution for chemical map and reduce the volume of interaction in the sample, and the WD was lowered to 6 mm so that mapping of smaller features and of samples with very small grain size (<10 μm) could also be performed. The melt composition is, however, difficult to measure accurately at such small scale, due to interferences with the surrounding minerals.

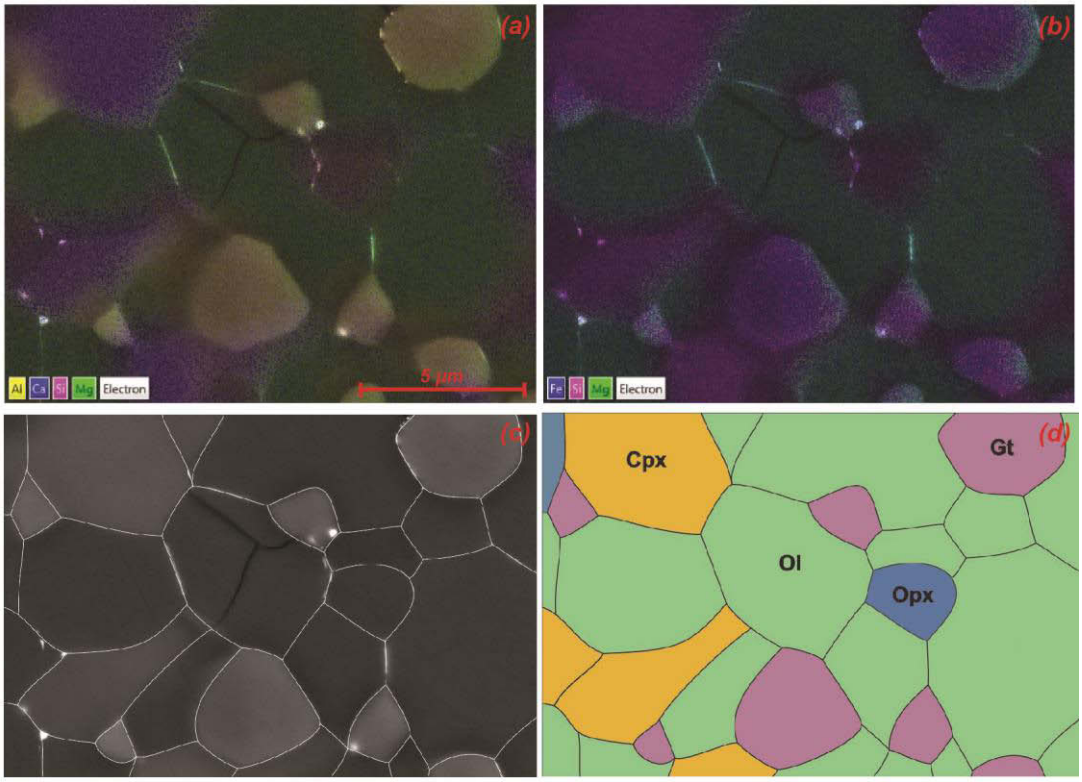

Figure 2.16. Results of the semi-quantitative chemical maps of a sample recovered after melting experiment. **(a)** and **(b)** show the combination of different elements (colour-coded), illustrating the difference in chemical composition for each grains, and, therefore, showing the different phases in the sample. Grain boundaries show the polygonal shape typical of good textural equilibrium **(c)**. *Ol*, *Cpx*, *Gt* and *Opx* stand for olivine, clinopyroxene, orthopyroxene and garnet, respectively **(d)**.

2.4.2. Determination of the water contents

We used infrared spectroscopy to determine the water content in our samples in the glass starting material as well as in the recovered samples. IR spectra were measured in air on double polished sections with thicknesses of 600 µm (for starting glass) or 900 µm (for recovered samples). Spectra were collected between 700-7000 cm^{-1}, with 2 cm^{-1} steps and 300 scans for the sample and 100 scans for the background.

On the recovered samples from HP-HT conditions, the grain size is significantly smaller (see for example figure 2.15) than the IR beam, and the several measurements performed within the same sample are consistent with each other. Measurements on such samples shows a water content of ~90 ppm of water, calculated from the broad asymmetric band centered at 3500 cm^{-1} and the OH peaks related to point defects in olivine (Ferot and Bolfan-Casanova, 2012), at 3572, 3527 and 3357 cm^{-1} (Figure 2.17.a).

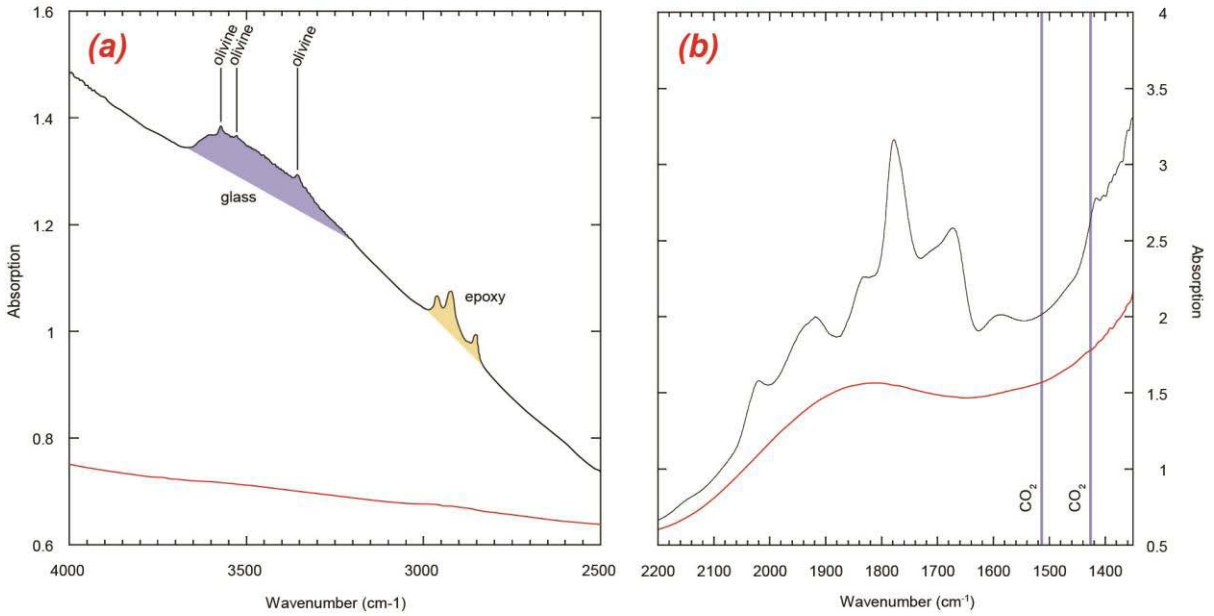

Figure 2.17. Fourier transform Infrared (FTIR) spectra of the glass starting material (in red) and of a sample after melting experiment (black line).

The triplet between 3000 and 2800 cm^{-1} is characteristic of the epoxy used to embed the sample for further analysis. The spectra also display the overtones of the silicate bands at 2200-1400 cm^{-1} (Figure 2.17.b). These observations confirm that H_2O contamination during the melting experiments was very limited. The H_2O content in the sample at the time of melting is critical because the presence of volatile elements can induce significant decrease of the melting temperature. We can also assess that no CO_2 was present during the experiments, as the spectra show no evidences of CO_3^{2-} bands at 1514-1427 cm^{-1}. On the starting glass, less than 1 ppb of water was measured, indicating that the starting material can be considered as nominally dry.

2.5. Cryoscopic relation

Effects of water on the melting properties have been investigated extensively at shallow mantle depths (Aubaud et al., 2004; Litasov and Ohtani, 2002; Novella and Frost, 2014). A depression of solidus temperature as a function of the water content was tentatively modelled by a cryoscopic relation from measurements available up to 3 GPa (Hirschmann et al., 1999). In this study, we modelled the solidus depression with increasing water content at different mantle depths using the cryoscopic relation (Tenner et al., 2012):

$$T^{hydrous} = \frac{T^{anhydrous}}{\left(1 - \frac{R}{\Delta\hat{S}^{fusion}} \ln\left(1 - X_{OH^-}^{melt}\right)\right)}$$

where $T^{hydrous}$ and $T^{anhyydrous}$ are the wet and dry melting temperatures, respectively, R is the gas constant, $\Delta\hat{S}^{fusion}$ is the molar entropy of fusion and $X_{OH^-}^{melt}$ is the mole fraction of dissolved OH^- in the melt (see e.g. (Aubaud et al., 2004; Hirschmann et al., 1999; Novella and Frost, 2014; Tenner et al., 2012)). Following Tenner et al. (2012), $\Delta\hat{S}^{fusion}$ was calculated using the equation:

$$\Delta\hat{S}^{fusion} = \Delta S^{fusion} * mol.wt._{silicate\ melt}$$

with ΔS^{fusion} = 0.4 J/K/g. This value is based on previous calorimetric measurement of melts from melting experiments performed in the CMAS (CaO-MgO-Al_2O_3-SiO_2) system (Kojitani and Akaogi, 1997). As all water can be assumed to be dissolved as OH^- in the melt (Tenner et al. 2012), $X_{OH^-}^{melt}$ is calculated by the equation:

$$X_{OH^-}^{melt} = \frac{(2 * wt.\%H_2O_{melt}/18.02)}{((2 * wt.\%H_2O_{melt}/18.02) + (100 - wt\%H_2O_{melt})/mol.wt_{silicate\ melt})}.$$

How to extrapolate this cryoscopic relation to deep mantle conditions remains uncertain. It partially relies on the pressure dependence of H partitioning between the peridotite and the melt $D_H^{peridotite/melt}$ used to calculate melt water contents, which could remain limited (Novella and Frost, 2014). Furthermore, because a strong data set of experimentally determined $D_H^{peridotite/melt}$ values was used to refine a self-consistent cryoscopic relation for pressures below 8 GPa, there are risks of inconsistency to use an independent measurement of the pressure dependency of the $D_H^{peridotite/melt}$ parameter alone at P>8 GPa. Hence, we adopted a constant bulk $D_H^{peridotite/melt}$ of 0.009 for extrapolations to the relevant upper mantle pressures.

3. RESULTS

3.1. Implications of a low solidus melting-temperature for the history of the Earth's upper mantle

3.1.1. Electrical conductivity measurements

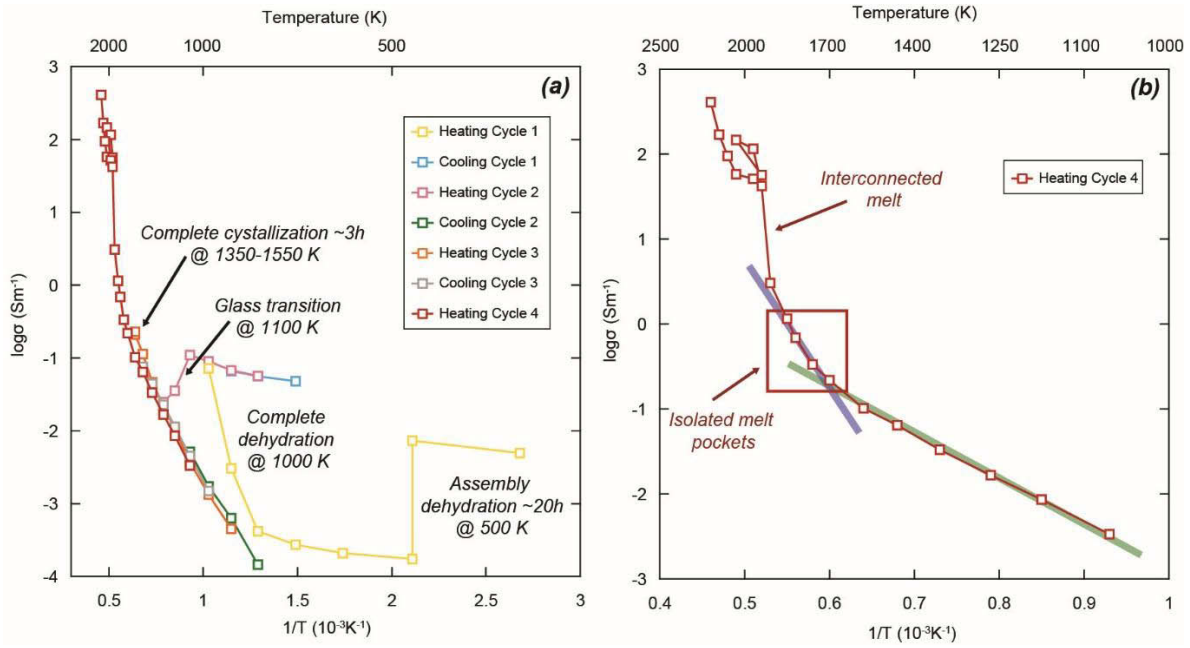

Figure 3.1. Arrhenius plot for one of the experiments at 5 GPa, showing the different heating and cooling cycles **(a)**, before the final heating cycle **(b)**.

We measured electrical conductivity of our chondritic silicate samples up to their melting point at pressures of 5, 10 and 20 GPa. A typical Arrhenius plot (Variation of log conductivity with respect to reciprocal temperature) of the electrical conductivity experiments is shown in figure 3.1.a. For each experiment, we performed a series of heating and cooling cycles, similar to other works on electrical conductivity (Manthilake et al., 2009). Initially, temperature was kept at 500 K overnight, in order to remove moisture from the surrounding assembly and from the environment in the press. In fact, drying proceeds progressively in different steps up to ~1100 K (heating cycle 1). The remaining presence of water (until the middle of heating cycle 2) is evidenced by a low slope in the conductivity profile, upon heating or cooling, because of the low activation enthalpies typical of proton conduction. During the second heating cycle, we can observe a clear drop in the sample conductivity at around 1100 K, due to the glass transition in the sample (glass transition and beginning of crystallization were also observed at the sample temperature in X-ray diffraction experiments performed at

synchrotron facility). After a time step of ~3h at temperatures between 1370 and 1570 K, we observed no discontinuous changes in the sample conductivity, nor in the activation energy, after performing various cycles of heating and cooling (from cooling cycle 2 to the end of the heating cycle 3), indicating that the crystallization process is completed in the sample. At this point, our sample impedance appears to vary exponentially with temperature with an activation energy of 1.02 eV (Figure 3.1.b green line). This is typical of electron hole hopping between Fe^{2+} and Fe^{3+} conduction mechanism by small polarons (Yoshino, 2010). At the onset of melting, a change in the conductivity slope can be observed. For a nominal pressure of 5 GPa, we observed a clear change of slope in the conductivity profile at a temperature of ~1700 K, with an activation energy of 2.5 eV (Figure 3.1.b, blue line). At small melt fractions, the melt is distributed in the form of isolated pockets between mineral grains, and total conductivity is affected by their contribution. However, the occurrence of melt will only effectively increase the overall conductivity when the melt phase is interconnected. When the melt fraction is large enough, the melt pockets will interconnect, and the melt network will control the overall sample conductivity. An abrupt jump in the conductivity by approximately one to two orders of magnitude can then be observed. The conductivity is observed to increase up to ~10^2 S/m. At this temperature, the melt becomes the dominant conductive phase, interconnected between the two electrodes, with an ionic conduction mechanism (Gaillard et al., 2008). Textural analysis of quenched experiments at each stage of the melting process confirmed the validity of our procedure (See figure 2.15). Similar evolutions of sample conductivity were already interpreted previously by the occurrence of an interconnected network of melt (Maumus et al., 2005; Partzsch et al., 2000; Sato and Ida, 1984).

Figure 3.2 shows the comparison between the last heating cycles of different experiments performed at 5 GPa, in comparison with electrical conductivity studies from the literature. A good agreement between electrical conductivity profiles measured in this study can be observed, confirming the reproducibility of our experimental method. Any minor differences between experiments are likely caused by small differences in sample geometry, taking into consideration by experimental uncertainties (temperature error is approximately ±25 degree, whereas pressure uncertainty can be up to 0.5 GPa at high P, yielding an overall error about 5% of the value). The lack of measurements at high pressure of the electric conductivity of partially molten rocks prevents a proper comparison with our results. Most of the studies in the literature, in fact, have been performed at either ambient pressure, or very low pressures (see Figure 3.2). Moreover, our experimental process aims at removing the greatest possible amount of water from the both the starting material and the experimental

assembly, allowing measurements of electrical conductivity of partially molten mantle rocks at the driest conditions achievable at the moment, which is one of the novelties of our study.

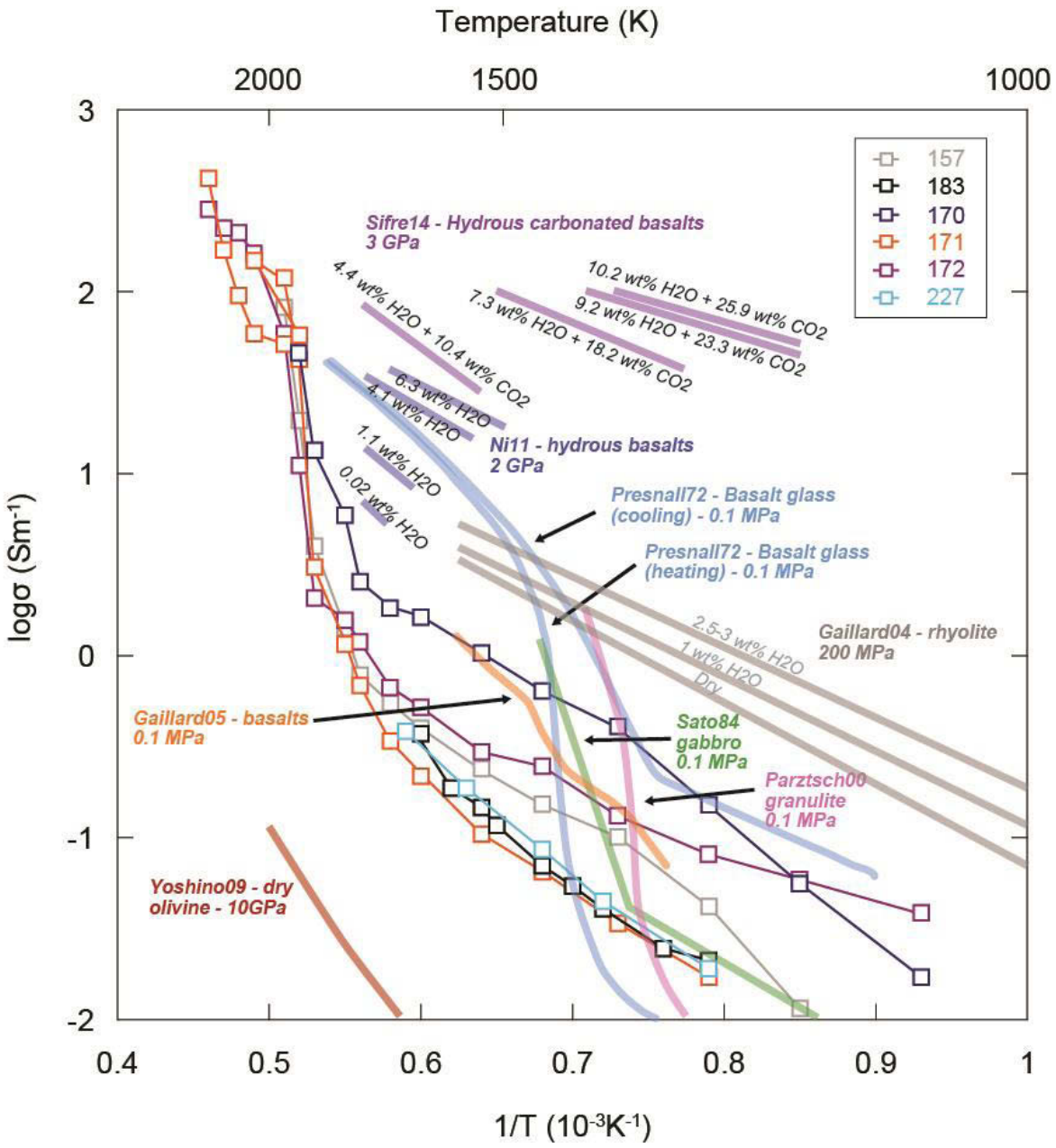

Figure 3.2. Comparison between our electrical conductivity experiments performed at 5 GPa and results from the literature (Gaillard, 2004; Gaillard and Marziano, 2005; Ni et al., 2011; Partzsch et al., 2000; Presnall et al., 1972; Sato and Ida, 1984; Sifre et al., 2014; Yoshino et al., 2009).

3.1.2. X-ray diffraction measurements

Temperature was further increased by steps of ~30 K while several diffraction patterns were recorded as a function of time (with varying acquisition times between a few seconds to about a minute). At each step, the intensity of diffraction peaks rapidly became constant with time after a short equilibration of the sample temperature. Above a threshold temperature, the sample behaviour became abruptly different: the diffraction peaks of the minerals suddenly underwent major changes of intensity with time. The large intensity variations at the time-scale of seconds could be seen on *real time* on the diffraction profiles recorded by the Ge-detector. These changes were also captured by recording several successive ten-seconds-long diffraction patterns (Figure 3.3). In several patterns, we observed the complete disappearance of one or more diffraction peaks, before the diffraction signal would eventually reappear on a next pattern. This phenomenon is produced by fast grain rotation relative to the X-ray beam. This abrupt change of sample behaviour denotes the onset of partial melting above the solidus temperature.

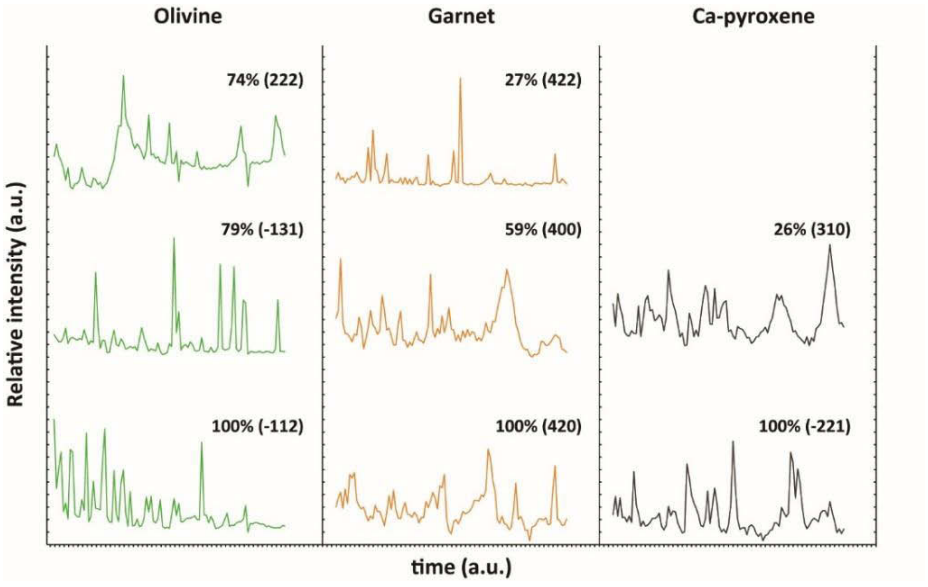

Figure 3.3. Fast variation of diffraction peaks intensity of the main phases as a function of time at constant temperature. Along the "time" axis, each point corresponds to a spectrum with an exposure time of 10 sec.

In presence of a small amount of melt, grain rotation is suddenly accelerated by a continuous process of dissolution, or growth, of grain surfaces. Grain growth is favored at some grain surfaces, while others are preferentially dissolved, and the rate of atomic diffusion at the grains interfaces is increased by orders of magnitudes due to presence of a thin film of melt. It

implies the modification of the grain shape and, thus, their rotation relative to the X-ray beam. Similar technique was used in a previous study using angle dispersive X-ray diffraction (Andrault et al., 2014). In the present study, based on the very good angle resolution of the CAESAR diffractometer (such as in (Wang et al., 2004)), we calculate that a grain found in a good orientation for diffraction of its given d_{hkl} plan would stop completely diffracting if its angle relative to the beam would be modified by ~10^{-3} degrees. Therefore, this method is extremely efficient to detect very small grain rotation associated to very low degree of partial melting.

3.1.3. The revisited solidus temperature: comparison with previous studies

Our two types of *in situ* measurements indicate both the mantle solidus on average 300 K lower than previously reported (Hirschmann, 2000; Litasov and Ohtani, 2002; Takahashi, 1986; Tronnes and Frost, 2002; Walter, 1998) (Figure 3.4).

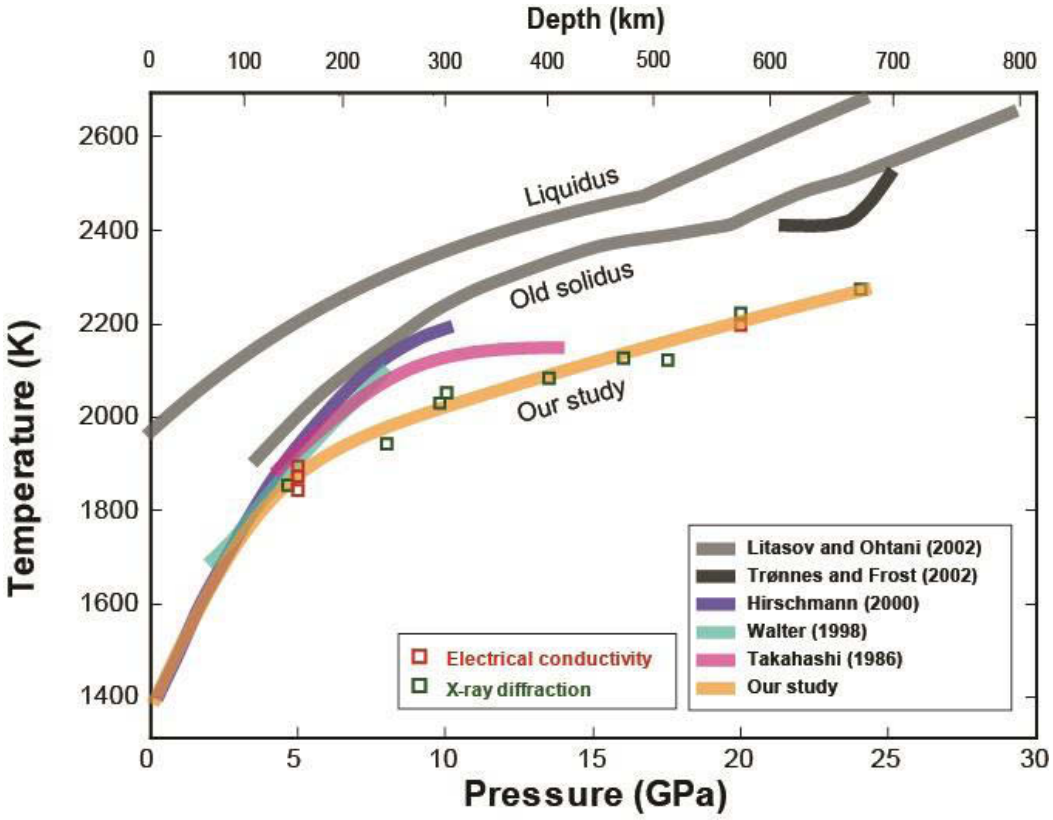

Figure 3.4. Solidus melting temperature obtained in this study from *in situ* electrical conductivity and X-ray diffraction, compared with previous works using the quench method (Litasov and Ohtani, 2002; Takahashi, 1986; Tronnes and Frost, 2002).

The reason for such a discrepancy with previous works can be manifolds: (i) In some previous studies, simplified compositions were used, sometimes without Fe (e.g. (Litasov and Ohtani, 2002)). A more geophysically-relevant composition used for our samples (see Table 2.1) is expected to lower the solidus. (ii) Previously, the melting criteria were most often based on the appearance of liquid pockets in the recovered sample. As mentioned above, low degree of partial melting can be difficult to detect, because of fast recrystallization of the melt at the grain interfaces upon quenching. Using the piston-cylinder apparatus, the solidus-melt can be trapped inside cracks that are previously made in the capsule walls. After several hours of sample equilibration, the melt can migrate into these cracks and remain protected against the rest of the sample during quenching (Laporte et al., 2004). None of the previous multi anvil experiments of mantle melting used this kind of technique. In our experiments, the use of *in situ* criteria to detect the onset of melting prevents these problems of quenching. (iii) Previously, melting criteria were based on the disappearance of one mineral from the phase assemblage (e.g. (Tronnes and Frost, 2002)). In complex chemical systems, there can be a significant temperature difference between the solidus, where a first liquid concentrates the fusible and incompatible elements, and the pseudo-eutectic temperature where a first mineral is entirely lost by dissolution in the liquid.

Another major difference between the previous experiments and ours is the nature of the starting material. Previous studies used mixture of oxide powders with typical grain sizes on the order of microns, while we used a glass, thus a material with an ideal chemical homogeneity at the atomic scale (as confirmed by electron microprobe analysis). The chemical heterogeneity intrinsically related to the mixture of powders could produce a kinetic effect, yielding to an overestimation of the solidus. The principle is that heterogeneous grain to grain configuration does not favour the occurrence of local regions (at the micron scale) where the chemical composition of the solidus melt would be achieved. Significant atomic diffusion, over a typical distance of the grain size, is needed to bring together the chemical elements that would produce the solidus liquid. Thus, melting is not occurring at the solidus temperature, but at temperatures above. Then, atomic diffusion because increasingly fast with the presence of a liquid phase, which results in an increasing degree of partial melting. This effect can be critical in multi anvil experiments because waiting-time is generally limited at high-temperature (less than 1 hour), in order to prevent loss of pressure after gasket flow. In contrast, the chemical interactions are much facilitated in a homogeneous glass, despite its crystallization upon heating to the solidus temperature, which produces a heterogeneous structure at the nanoscale.

3.1.4. Determination of the degree of partial melting in previous experiments

Based on our new determination of the mantle solidus, and using a fixed value of T_0=1373 K at room pressure (Hirschmann, 2000), we calculated an equation of melting using the modified Simon&Glatzel (SG) equation [$T_m(P)=T_0*(P/a+1)^{1/c}$] (Table 3.1).

SG-param.	$UM_{Solidus}$	A_{SG}	B_{SG}	$UM_{Liquidus}$	$LM_{Solidus}$	$LM_{Liquidus}$
T_0	1373.0	0.4450	0	1983.4	1335.7	1867.6
a	0.8225	2.8120	4.0792	6.4815	9.6535	21.150
c	6.9392	-0.35643	0.12750	5.3513	2.4070	2.1511

Table 3.1. Simon&Glatzel parameters refined for the upper mantle (columns between $UM_{Solidus}$ and $UM_{Liquidus}$) based on the generalized SG model defined in this work. We also provide S&G equations for the lower mantle, based on the 24 GPa data point of this study and a previous work (Andrault et al., 2011a).

In this equation, T_0, a and c are adjustable parameters and P is pressure (Simon and Glatzel, 1929). Same calculation was also performed for the dry liquidus, using previous work performed on KLB-1 peridotite (Herzberg and Zhang, 1996; Iwamori et al., 1995). At temperatures between the solidus and the liquidus, only a couple of works report the degree of partial melting (F) for pressures relevant to the upper mantle (Iwamori et al., 1995; Walter, 1998). Also, the covered pressure range do not extend above 10 GPa. Alternatively, several experimental works were performed below 3 GPa or with relatively large temperature gradients, which disables a proper determination of F. In many reports (e.g. (Herzberg and Zhang, 1996; Tronnes and Frost, 2002) the reported sample images evidence large amount of melting with segregation of the melt from the solid residue.

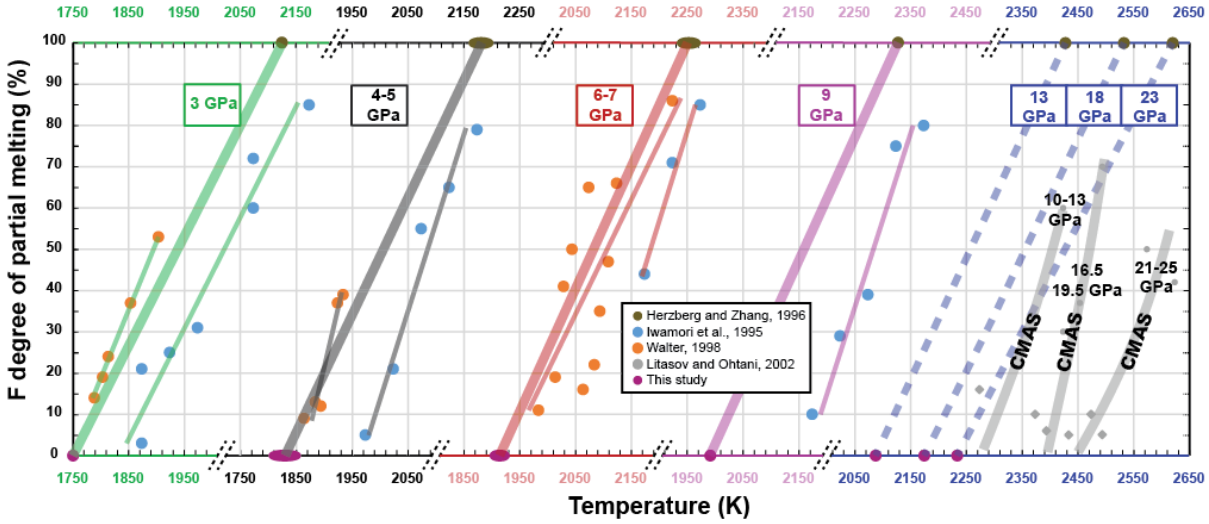

Figure 3.5. Degree of partial melting as a function of temperature and at different pressure ranges. Blue (Iwamori et al., 1995) and orange (Walter, 1998) and grey (Litasov and Ohtani, 2002)dots show linear trends. Linear trends are also drawn between the new solidus (purple dots) and the liquidus (Herzberg and Zhang, 1996; Iwamori et al., 1995). The CMAS composition is ~200K more refractory due to lack of Fe, Na, K, etc. in the experimental charge.

When reporting the value of F as a function of temperature at different pressure ranges (Figure 3.5), it first appears that the previous available trends do not agree well with each other. The disagreement could be come from slight difference in composition of the starting materials (peridotite (Iwamori et al., 1995) or garnet-peridotite (Walter, 1998)), as discussed in length in previous works (Herzberg et al., 2000a; Hirschmann, 2000), or to difference in the pressure calibration. Nevertheless, all trends taken one by one clearly show a linear variation of F with temperature, at least up to 9 GPa. This is also true for the data set available at pressures up to ~25 GPa for the more-refractory CMAS composition (free of Fe, Na, K, etc.). Accordingly, we draw linear trends between the new solidus and the liquidus temperatures (Figure 3.5). It happens that these trends plot in very good agreement with one of two available reports (Walter, 1998)).

There are different way to model these trends of F=(f(P,T) and, in this work, we propose to define a generalized Simon&Glatzel equations of melting that would take into account all the parameters. For this, we allowed the T_0, a and c parameters to be polynomial functions of F (order 2). The equation becomes:

$$T_m(P,F) = T_0^{sol} * (1 + A_T F + B_T F^2) * (P/(a^{sol}(1 + A_a F + B_a F^2)) + 1)\text{^}(1/(c^{sol}(1 + A_c F + A_c F^2)))$$

Where (T_0^{sol}, a^{sol}, c^{sol}) are the SG parameters of the solidus, and (A_T,B_T), (A_a,B_a), and (A_c,B_c), are refined based on the synthetic linear trends drawn in figure 3.5. Based on this model, SG-type melting curves (Figure 3.6) can be recalculated between the solidus and the liquidus for any given values of the melt fraction (Table 3.1).

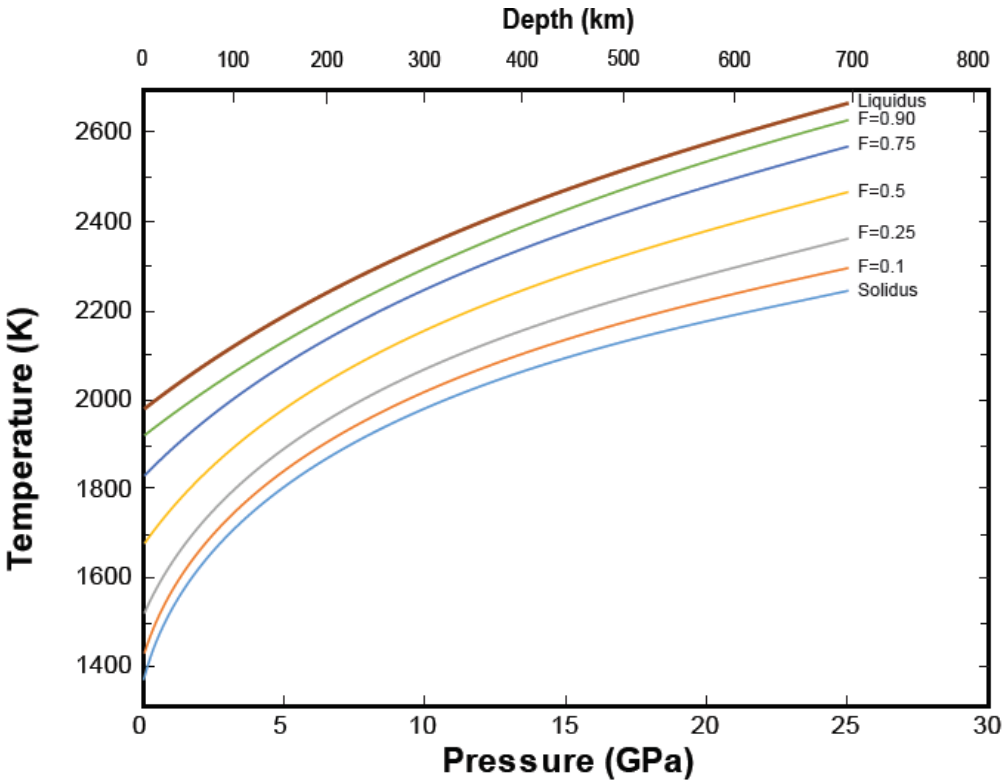

Figure 3.6. Simon&Glatzel equation of melting calculated for different degrees of partial melting between the solidus (F=0) and the liquidus (F=1) in the pressure range of the upper mantle. The data set is equivalent to the linear trends presented in figure 3.5.

3.1.5. Implications for the presence of water in the upper mantle today

The low mantle solidus temperature has major implications for our understanding of the mantle state today and, in particular, of the geophysical reports of seismic anomalies in the upper mantle, for both the LVZs and the LVL (e.g. (Romanowicz, 1995b; Tauzin et al., 2010)). We now compare our solidus measurements with the accepted geotherm for the first 500 km mantle depths, constrained by (i) the adiabatic temperature profile extrapolated to the surface from anchor points in the transition zone (Katsura et al., 2010) and (ii) the temperature profiles in (younger) oceanic crust or (older) cratonic lithosphere (Litasov et al., 2014) (Figure 3.7). A first conclusion is solidus temperatures higher than the geotherms at all mantle depths, showing

that the dry mantle should not experience melting (we note that our recovered samples contained in fact ~90 ppm water, an effect that is considered below). Thus, if partial melting should indeed occur today in the asthenosphere, it would evidence the presence of volatiles. Both water and CO_2 reduce significantly the mantle solidus temperature (Figure 1.4), however, our further discussions solely focus on the effect of water. The reason for that choice are manifolds: (i) H is more abundant than C in the upper mantle, (ii) while CO_2 could definitely induce seismic anomalies (Dasgupta and Hirschmann, 2006; Ghosh et al., 2009; Litasov et al., 2014), carbonates fluids might be non-ubiquitously distributed in the upper mantle, in contrast with some seismic features (Romanowicz, 1995b; Tauzin et al., 2010), and (iii) H can be homogeneously inserted as a defect in the nominally anhydrous minerals, or eventually released above a saturation limit (Ferot and Bolfan-Casanova, 2012), at all mantle depths.

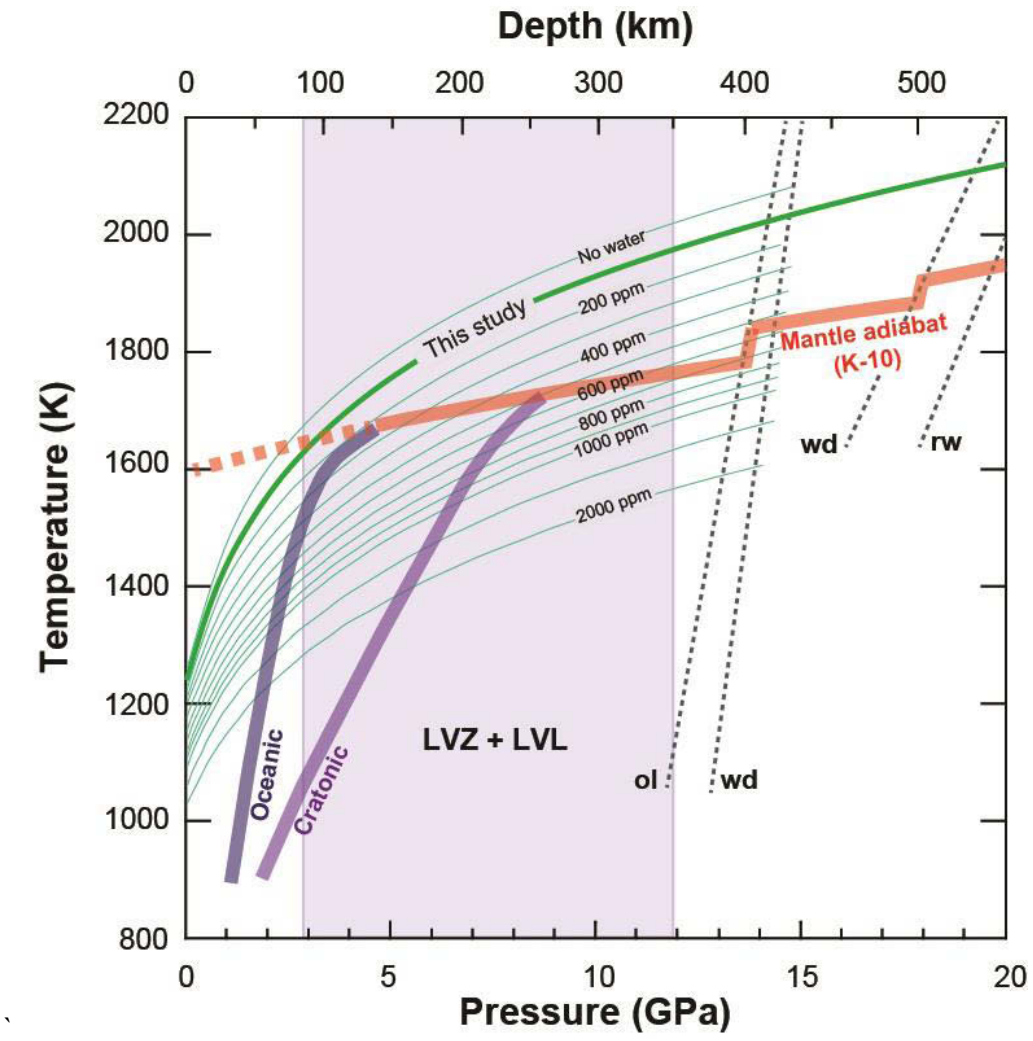

Figure 3.7. Upper mantle solidus profiles calculated as a function of water content using the cryoscopic relation (see text) (Hirschmann et al., 1999). We also report the mantle geotherms estimated for oceanic and cratonic regions (Litasov et al., 2014). The present-day mantle adiabat (K-10) correspond to a potential surface

temperature of ~1600 K (Katsura et al., 2010). Dashed grey lines represent the phase transition between olivine (ol), wadsleyite (wd), and ringwoodite (rw), including depth intervals for the progressive transitions. The purple shadow region corresponds to mantle depths where seismic anomalies have been reported.

The effects of water on the melting properties have been investigated extensively at shallow mantle depths (Aubaud et al., 2004; Litasov and Ohtani, 2002; Novella and Frost, 2014). In particular, the depletion of solidus temperature to be expected as a function of the water content was tentatively modelled by a cryoscopic relation from precise measurements performed up to 3 GPa (Hirschmann et al., 1999). Using our measurements as a new solidus reference for a ~90 ppm water content, we extrapolated the cryoscopic relation to higher mantle depths (Figure 3.7). Compared with the mantle geotherm, this calculation shows that the presence of 500-600 ppm of water are sufficient to induce mantle melting at mid upper-mantle depths where the LVL are reported. This amount of water is very consistent with the maximum water storage capacity of the mantle, of ~500 ppm at depths of 200-250 km (Ferot and Bolfan-Casanova, 2012). For a given water content, higher degree of partial melting should be expected at shallower depth, due to the fact that the mantle geotherm gets closer to the temperature of the dry solidus, until the stepper temperature profile typical of the crust is reached. This line of reasoning is perfectly compatible with more pronounced seismic anomalies reported at shallower depths, up to above a depth of 80 km where the LVZ disappear.

3.1.6. Implications for state and dynamics of the early upper mantle

Concerning mantle temperatures earlier in the Earth's history, studies of komatiitic lavas with Archaean and Proterozoic ages have revealed that the surface potential temperature (T_s, temperature of the mantle adiabatic profile extrapolated to the surface) was 200-300 K higher about 3.5 Gy ago, at a value of 1800-1900 K, compared to the current value of ~1600 K (Herzberg et al., 2010). For T_s temperature higher than 1900 K (300 K higher than the present-day T_s), the mantle should be largely molten with both a high degree of partial melting at mid mantle depths and in a large range of depths extending deep into the lower mantle (Figure 3.8). Here, we do not include the possible role of the volatiles elements early in the Earth's history. The initial absence of deep subduction probably favoured a deep mantle relatively depleted in volatiles (Magni et al., 2014). Assuming a moderate amount of H_2O and CO_2 in the primitive mantle would not change largely our conclusion). The degree of partial melting F is difficult to define precisely, however, it could be easily reach the threshold value

40% between liquid and viscid mantle behaviour (Abe, 1997) (i.e. for F < 40%, the viscosity of the mixture is controlled by that of the solid particles while for F >40%, the viscosity is controlled by that of the melt). In such a liquid regime, one should expect rapid mantle cooling below 1900 K, in a similar manner than reported for the magma ocean (Abe, 1997; Solomatov, 2015).

For T_s below 1900 K, in fact, despite some remaining partial melting at mid-mantle depth, achievement of a viscous mantle (below F=0.4) would be compatible with a much slower mantle cooling. At T_s of ~200 K above the current temperature (thus ~1800 K), partial melting is expected to be restricted at depths ranging between ~200 and ~350 km. This region could be extended to shallower mantle depths, if the cold superficial front of the thermal boundary layer would be thinner in the ancient crust.

At T_s of 200 K above the current temperature, partial melting is expected at depths ranging between ~200 and ~400 km. We note that this region could easily extend to shallower mantle depths, if the cold superficial front of the thermal boundary layer would be thinner in the ancient crust. This mantle state including a partially molten shell at mid upper-mantle depths could be responsible for eruption of magmas with a high-pressure origin, such as carbonatitic lavas (Herzberg et al., 2010; Vinnik and Farra, 2007). Even more importantly, such layer would present much weaker mechanical properties compared to the crust and the lower mantle. It could induce the dynamical decoupling of the upper and lower parts of the mantle (Bercovici and Karato, 2003b), preventing a global mantle convection and instead favour independent upper and lower convective dynamism, in full agreement with geodynamical modelling (Gerya, 2014). It was suggested that the melts could remain neutrally buoyant at mid-mantle depths, producing a kind of melt trap (Matsukage et al., 2005; Sakamaki et al., 2006). Still, some of the melt could eventually rise toward the Earth's surface, which could be responsible for the eruption of magmas with a high-pressure origin (Herzberg et al., 2010; Vinnik and Farra, 2007). After the removal of some melt, the introduction at mid upper-mantle depth of any new pyrolitic material would induce melting again, due to a local temperature higher than the solidus.

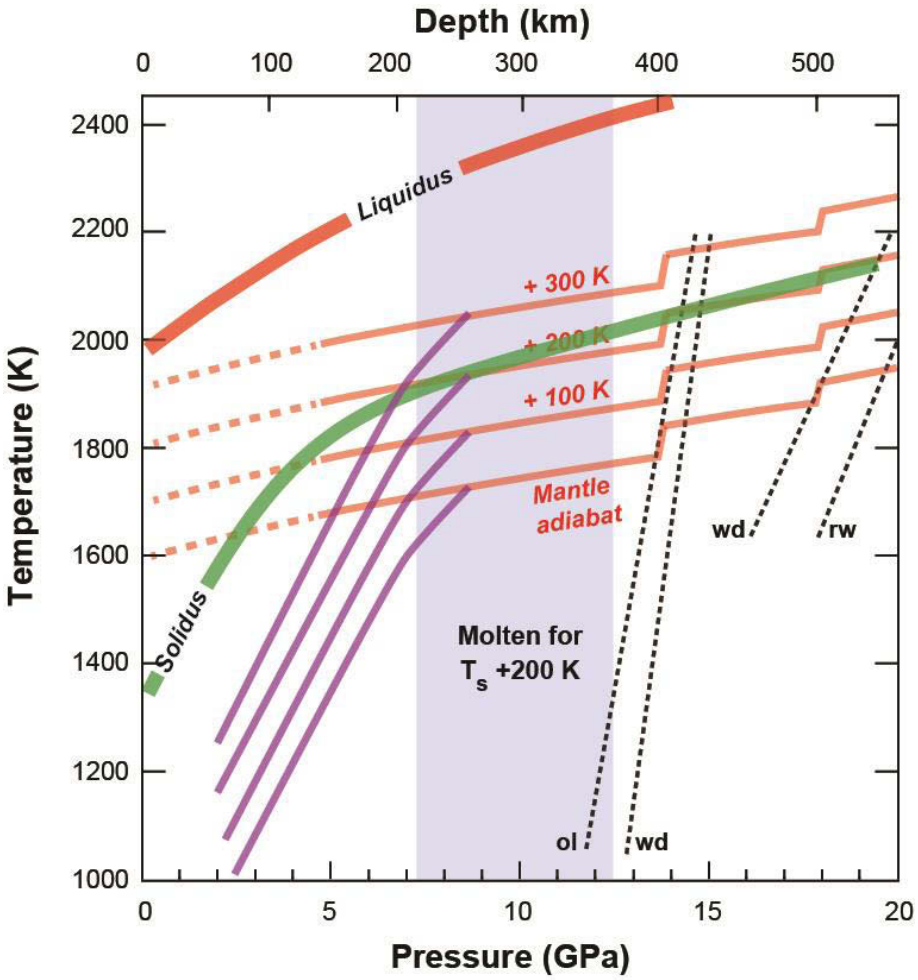

Figure 3.8. Present day temperature profiles (cratonic region + mantle adiabat) together with the ancient temperature profiles when the potential temperature was from 100 to 300 K higher. We compare this profiles with a dry-solidus (corrected for the ~90 ppm water present in our samples, see main text) and the liquidus previously reported for peridotite (Litasov and Ohtani, 2002). The purple shadow region correspond to a range of depths where the "+200 K" temperature profile is above the solidus.

With secular cooling, T_s has eventually decreased below the threshold value of ~1750 K when the geotherm becomes lower than the dry solidus at all mantle depths. This would correspond to the disappearance of the partially-molten weak layer. It would induce a drastic change in the mantle dynamics, enabling the mechanical coupling between the two previously independent mantle reservoirs (Foley et al., 2014; Gerya, 2014; Kamber, 2015; van Hunen and Moyen, 2012). This transition would make possible the entrainment of slabs deep into the mantle and produce crustal tectonics within a similar regime than observed today. This transition formally related to final crystallization of the upper mantle could have happened at the transition between Archaean and Proterozoic ages, about 2.5 Gy ago.

3.1.7. Implications for Magma Ocean crystallization

The newly measured solidus curve has another direct implication on the mechanism of magma ocean crystallization, in the context primitive Earth. Indeed, due to the large amount of energy released by giant meteoritic impacts, the mantle temperature had likely exceeded the solidus and liquidus temperatures by a few thousand Kelvins (Melosh, 1990), at least for the depth corresponding to the current upper mantle. Cooling of the magma ocean is mainly controlled by two factors: (i) the possible presence of an atmosphere controlling the surface heat flux (discussed below); (ii) the magma ocean viscosity (Abe, 1997). Low viscosity induce vigorous and turbulent convective flows, which favour thin thermal boundaries and large heat flux at the magma ocean surface. Under such regime of convection, the magma ocean surface temperature is expected to decrease fast, in a few thousand years (e.g. (Solomatov, 2007)). Upon cooling, the magma ocean temperature will eventually reach the liquidus, which induces fractional crystallization. When the melt fraction becomes lower than threshold value of 40%, there is a definite rheological change from liquid to viscous behaviour, due to the unavoidable contact between grains. In a viscous mantle, the thermal boundaries get larger and the Earth's cooling is slowed down. At this point, chemical fractionation can take place between the different mantle reservoirs, due to longer time scales allowing liquid-solid gravitational segregation, before the mantle solidification is eventually completed.

In order to define solidus and liquidus profiles valid at all mantle depths, we have associated together our results on the solidus together with (i) the liquidus profile reported for pyrolite at depths corresponding to upper mantle and transition zone (Litasov and Ohtani, 2002) and (ii) solidus and liquidus curves of a chondritic-type mantle determined at lower mantle conditions (Andrault et al., 2011b). The difference in chemical composition between the different starting materials used in these studies should represent a minor effect on melting temperature, in a range probably similar to the experimental uncertainties, especially for the measurements performed at lower mantle conditions. The composite solidus and liquidus profiles were fitted using the modified Simon and Glatzel equation [T=T0 (P/ a+1)1 / c] with T_0=1464 K, a=15 GPa and c=2.25 for the solidus, T_0=2018 K, a=34.7 GPa and c=1.9 for the liquidus (Simon and Glatzel, 1929). Then, we estimated the 40% melt fraction curve, based on a linear interpolation between the solidus and the liquidus (Simon and Glatzel equation values: T_0=1718.5 K, a=22.7 GPa and c=2.1). For high mantle depth, we are aware that choosing the melting curves reported by one group, instead of those from another group (Andrault et al., 2011b; Fiquet et al., 2010), could affect slightly the conclusions. However, the effect should

remain minor for the determination of the mechanism of magma ocean crystallization at shallow mantle depth, because the major differences between these studies concern the liquidus profile at high depths.

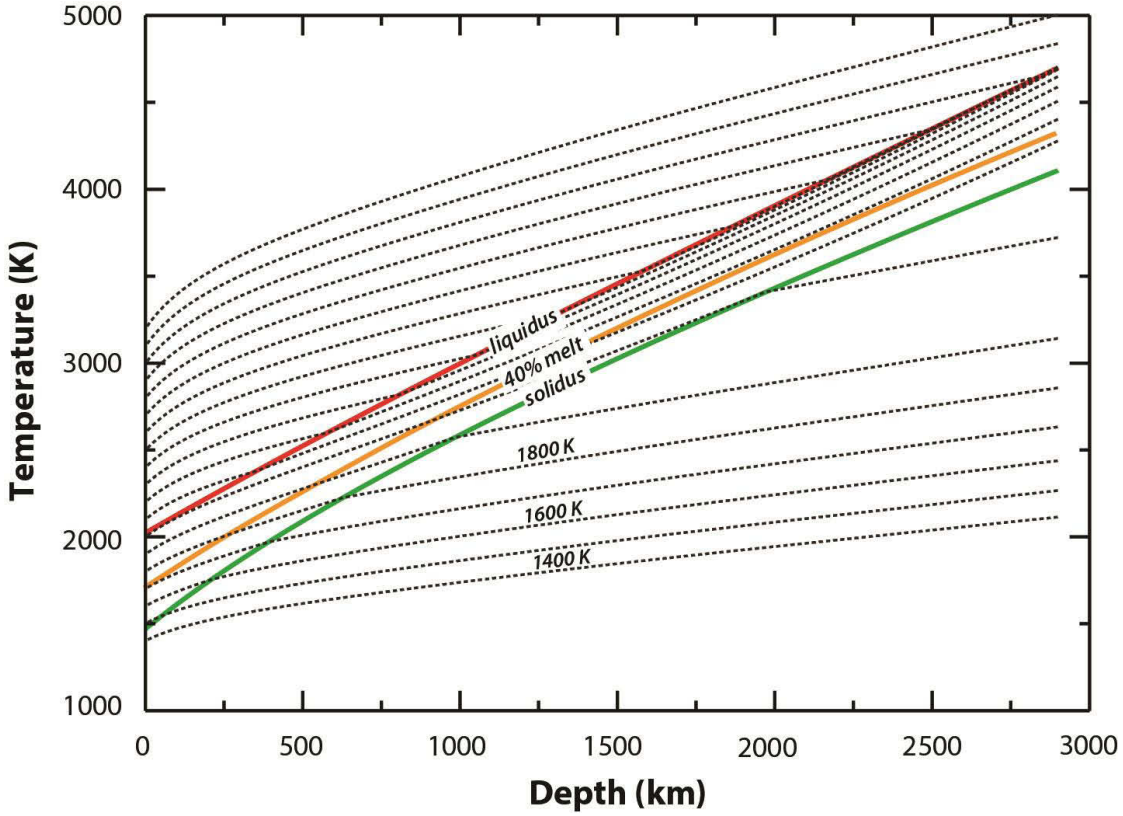

Figure 3.10. Isentropic profile of the mantle based on our new melting curves. The 40% melt represents the viscosity threshold at 60% of crystallization.

In addition, the equation of state of a chondritic-type primitive mantle (Mosenfelder et al., 2009; Thomas and Asimow, 2013) was used to calculate the isentropic temperature profiles in the magma ocean, for various potential surface temperature (*Tp*) (Figure 3.10). The intersection between the adiabatic profiles in one hand, and the liquidus, the line of 40% melt fraction and the solidus in the other hand, yields original information on the mechanisms of magma ocean crystallization as a function of mantle depth (Figure 3.11.a). It appears that 100% of partial melting at the core-mantle boundary (CMB), or at the Earth's surface, are achieved when *Tp* is higher than ~3100 K, or ~2000 K, respectively. For *Tp* values in between, only the shallower part of the mantle is fully molten. Same reasoning is valid for the highest mantle depth encountering 40% of partial melting, which limits range from ~2400 K (more than 40%

of partial melting at all mantle depth) and ~1700 K (less than 40% of partial melting at all mantle depth), as well as for the solidus.

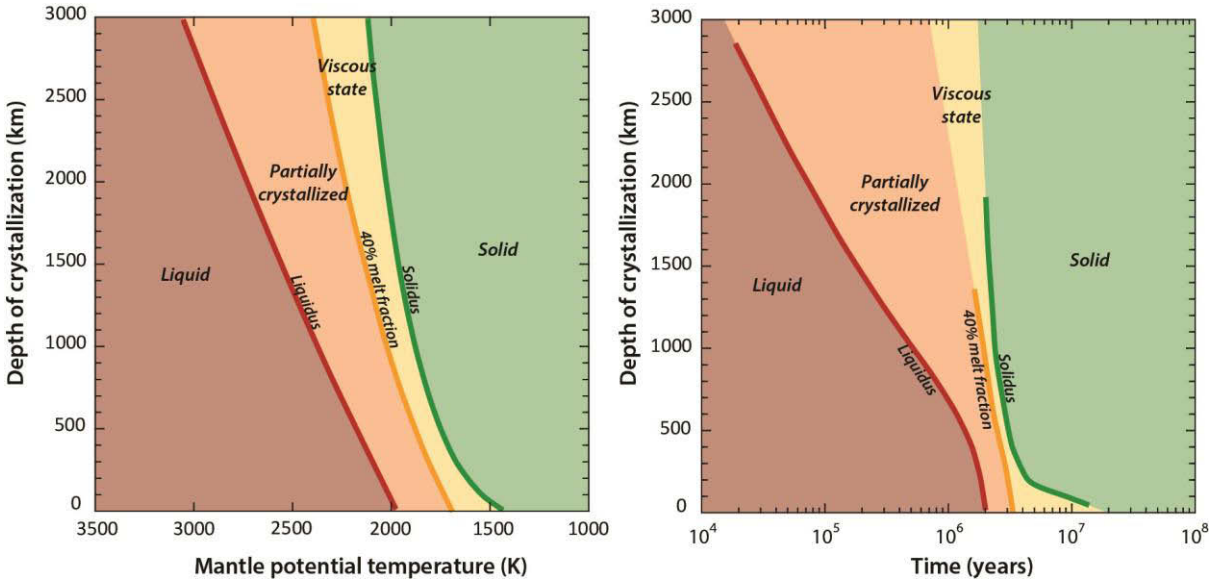

Figure 3.11. Variation with (**a**) potential temperature or (**b**) time of the depth of mantle crystallization at liquidus (red line), achieving 40% melt fraction (yellow line) and solidus (green line), where the magma ocean starts crystallizing, becomes viscous and complete its crystallisation, respectively. The solidus and liquidus temperatures are taken from (Andrault et al., 2011b; Litasov and Ohtani, 2002) and this study (see text). The evolution with time of the potential surface temperature is taken from (Lupu et al., 2014).

Previous studies report the timing of Magma Ocean cooling in the Earth after a giant Moon-forming impact (e.g. (Hamano et al., 2013). It was shown that the presence, or absence, of an atmosphere controls the surface temperature and thus the heat flux escaping into space. Without an atmosphere creating a greenhouse effect, the mantle crystallizing could be completed in a matter of a few thousand years (e.g. (Abe, 1997)). With an early gaseous atmosphere in equilibrium with the magma ocean, as suggested by recent references, a blanketing effect (of a 100 bar atmosphere in equilibrium with the magma ocean, for example) could delay the crystallization for approximately 1 My (Lebrun et al., 2013). We use the reported correlation between *Tp* and time (Lupu et al., 2014; Sleep et al., 2014) to address the thermal history of the early Earth after a giant impact, with a model for the depth of crystallization as a function of time (Figure 3.11.b). Following the time evolution of *Tp* published elsewhere, the magma ocean should be solidifying at all mantle depth after a couple of My, due to a temperature profile lower than the solidus. We note that this time would be even shorter if we would use the liquidus profile published by another group that plots at higher

temperature (Fiquet et al., 2010). Not much later, the whole magma ocean would cross the rheological threshold corresponding to 60% of crystallization. At this point, the mantle becomes viscous and the convection rate is significantly reduced. Complete crystallization of the magma ocean could take up to 10 My, due to a persistent molten region at the top of the mantle. However, this value may be a higher limit, since the occurrence of a relatively thick thermal boundary layer at the Earth's surface should help to finalize the crystallization.

3.2. Melting of subducted basalt at the core-mantle boundary (CMB)

DEEP EARTH

Melting of subducted basalt at the core-mantle boundary

Denis Andrault,[1]* Giacomo Pesce,[1] Mohamed Ali Bouhifd,[1] Nathalie Bolfan-Casanova,[1] Jean-Marc Hénot,[1] Mohamed Mezouar[2]

The geological materials in Earth's lowermost mantle control the characteristics and interpretation of seismic ultra–low velocity zones at the base of the core-mantle boundary. Partial melting of the bulk lower mantle is often advocated as the cause, but this does not explain the nonubiquitous character of these regional seismic features. We explored the melting properties of mid-oceanic ridge basalt (MORB), which can reach the lowermost mantle after subduction of oceanic crust. At a pressure representative of the core-mantle boundary (135 gigapascals), the onset of melting occurs at ~3800 kelvin, which is ~350 kelvin below the mantle solidus. The SiO_2-rich liquid generated either remains trapped in the MORB material or solidifies after reacting with the surrounding MgO-rich mantle, remixing subducted MORB with the lowermost mantle.

Numerous seismological studies have demonstrated the complexity of the lowest 150- to 300-km-thick mantle layer situated just above the core-mantle boundary (CMB). In many areas, there is an intermittent stratification, with 1.5 to 3% velocity discontinuities, as well as lateral shear-wave anisotropy (*1*). These anomalies could arise from mineralogical heterogeneities (*2*), magma ocean crystallization (*3*), the descent of subducted slabs deep into the lower mantle (*4*), and/or chemical reactions with the outer core. In addition, ultra–low velocity zones (ULVZs), with shear-wave velocity reduction of more than 10%, have been detected in specific mantle regions (*5*). Their size is limited to ~40 km thickness and ~100 km across, and they are ~10% denser than the surrounding mantle. These ULVZs could be due to partial melting occurring in a steep temperature gradient when approaching a very hot outer core. Between 5 and 30% partial melting could attenuate *P* and *S* seismic wave velocities to a similar amplitude as that reported for ULVZs (*6*). However, it was recently shown that partial melting of the bulk lower mantle cannot produce a residue with an equilibrium partial melt that is sufficiently dense to adequately represent the ULVZ mush (*7*).

Partial melting of pyrolitic or chondritic mantle would be possible if the CMB temperature were higher than ~4150 K (*8*, *9*). Although such a high temperature is not precluded, it would require a very hot core. It is more than 1000 K above the most recent determination of the mantle adiabat extrapolated to the CMB (*10*). Moreover, the presence of a very hot core today makes it difficult to explain how a geodynamo could have been maintained for prolonged geological periods: An even hotter core would be required in the past, or an extremely high concentration [400 to 800 parts per million (ppm)] of K in the core (*11*). Alternatively, partial melting in the lowermost mantle could occur below 4150 K if the mantle composition were drastically altered. Chemical differences between peridotite, pyrolite, and chondritic-type mantle would produce only minor variations, because they contain similar mineralogical assemblages. However, a local concentration of fusible (such as alkalis) or volatile (H_2O or CO_2) elements, together with a change in mineralogy, could have a marked effect on the solidus temperature. In particular, a small water concentration can be enough to reach the saturation limit of the bulk mantle (*12*). Consequently, the melting curve of hydrous pyrolite has much lower melting temperatures (*13*).

We investigated the melting behavior of a natural mid-oceanic ridge basalt (MORB) collected at a 2800-m depth during the Searise-1 research cruise (table S1). When a MORB eventually reaches Earth's lower mantle, it is composed of four coexisting phases: (i) Fe-rich silicate perovskite (Mg-Pv); (ii) free silica, in contrast with free (Mg, Fe)O ferropericlase (Fp) in the bulk mantle (fig. S1); (iii) Ca-bearing silicate perovskite (Ca-Pv); and (iv) enough Al, Ca, Na, and K to generate cage structures such as calcium ferrite (CF), hollandite, or an aluminous phase (*14*–*16*). Our starting material contained ~0.3 weight % H_2O and traces of CO_2 (fig. S9), which are common volatile concentrations for natural MORBs. At lower mantle pressures, the basaltic portion of the slab contains minerals that can carry water, such as the Al-bearing stishovite (*17*), δ-AlOOH (*18*), and phase H (*19*).

High pressures and temperatures were provided by a laser-heated diamond anvil cell [fig. S2 (*8*)]. The sample behavior was followed continuously using in situ x-ray diffraction (Fig. 1 and supplementary materials). Upon heating, we first observed the appearance of a continuous diffraction ring on the charge-coupled device detector, at d_{hkl} distances typical of Mg-Pv. This

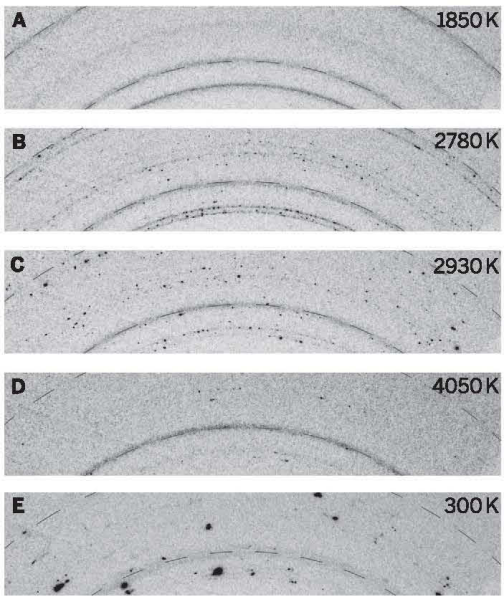

Fig. 1. Sequence of x-ray diffractions recorded with increasing temperatures from 1850 to 4050 K at 56 GPa. Diffraction peaks of the KCl pressure medium are superimposed in blue. Upon heating, (**A**) we first observed the appearance of weak Mg-Pv diffraction peaks, (**B**) followed by crystallization of all other phases, including Ca-Pv and stishovite. Above 2930 K, (**C**) diffraction peaks become suddenly much sharper. Also, all diffraction peaks for a given sample drastically change position on images recorded successively at the same pressure and temperature conditions. Above 4050 K, (**D**) only a few diffraction peaks remain visible. The quench image (**E**) contains several new peaks, showing that the lack of diffraction peaks at the highest temperature was not due to a loss of sample, but rather to complete sample melting.

[1]Laboratoire Magmas et Volcans, Université Blaise Pascal, CNRS, IRD, Clermont-Ferrand, France. [2]European Synchrotron Radiation Facility, Grenoble, France.
*Corresponding author. E-mail: denis.andrault@univ-bpclermont.fr

ring occurred above 1800 and 2500 K, at 40 and 135 GPa, respectively. The relatively large peak profile is typical of a powder with very small grain size (Fig. 1A). At higher temperatures, Ca-Pv and silica appeared simultaneously (fig. S3 and table S2). The latter adopts either the structure of rutile (stishovite), $CaCl_2$, or α-PbO_2 (seifertite), as a function of pressure (fig. S4). Diffraction peaks of the post-perovskite phase of $MgSiO_3$ also appeared above 115 GPa. Diffraction features typical of CF and/or the so-called new aluminous phase remained weak because of major overlaps of their diffraction peaks with those from the other phases present in the sample (*15*).

Less than 100 K above the temperature at which Ca-Pv and silica crystallized from the glass, the initially continuous diffraction rings evolved suddenly into a discontinuous juxtaposition of spots (Fig. 1B), and the peak shape sharpened drastically, showing a net discontinuity in the rate of grain growth. At slightly higher temperatures, diffraction images acquired repeatedly at the same temperature, with a time interval of 20 s (acquisition time), showed large diffraction spots in totally different positions, indicating fast grain rotation. These changes in the sample properties were associated with a flattened temperature profile, although laser power was increased continuously (fig. S5). This effect could result from a change in laser absorption due to the structural transformation (*20*). Our results show that the temperature gap between rapid grain growth and fast grain rotation is less than 200 K (fig. S3). In theory, the extensive grain rotation should take place close to the solidus temperature. The sudden change in sample behavior is most probably due to the appearance of a small amount of liquid at grain boundaries. Because the very first degree of melting can be difficult to detect, we bracketed the solidus using these two major criteria—rapid grain growth and fast grain rotation—where the solidus temperature profile should plot (fig. S3).

The solidus increases continuously from about 2100 (±150) to 3200 (±150) K with an increase in pressure from 20 to 80 GPa (Fig. 2). At the latter pressure, which corresponds to a mantle depth of 1900 km, the MORB solidus is identical to that of a chondritic-type mantle (*8*). With a further increase in pressure to 135 GPa, the MORB solidus temperature increased to 3800 (±150) K, whereas that of the bulk mantle increased to 4150 (±150) K. The flattening of the MORB solidus could be linked to a change in liquid composition with pressure. Extrapolation of our solidus melting curve to ambient pressure yields a melting temperature of ~1300 K, in agreement with previous studies (*21*). However, we could not reproduce the rapid increase of solidus temperature at the low pressures observed in previous studies using a large-volume press (*21*, *22*). Because analyses were performed on quenched samples, for which it is difficult to observe low degrees of partial melting, we believe that the solidus temperature was possibly overestimated in these previous studies. Our solidus curve also plots at much lower temperatures than a previous study performed up to 65 GPa, using a laser-heated diamond anvil cell (*22*). In that study, the melting criterion based on the change of temperature with laser power, for a MORB sample sandwiched between two Re foils, may have hampered detection of the solidus. The maximum discrepancy between the different studies is ~400 K and tends to decrease with increasing pressure above 20 GPa. At 60 GPa, the discrepancy is down to ~250 K between the previous optical (*22*) and our in situ measurements.

To verify that the 350 K melting temperature reduction between MORB and the chondritic-type mantle was not an experimental artifact, we loaded both compositions in the same pressure chamber (fig. S2). Using the same melting criteria as in a previous study of mantle melting (*8*), we observed the solidus of chondritic mantle at temperatures of 2980 (±150), 3450 (±150), and 3680 (±150) K, for pressures of 58, 85, and 107 GPa, respectively, falling within ±60 K of our previous study (*8*). Given the higher amount of fusible elements in MORB, one could have expected a lower solidus temperature as compared to chondritic mantle. However, the role of SiO_2 excess in MORB and Fp excess in the mantle cannot be neglected (fig. S1).

Upon further increase of the laser power, the sample temperature eventually rose above the plateau temperature, allowing us to record diffraction patterns up to ~5000 K. We rarely observed the total disappearance of all diffraction peaks from the sample. Instead, diffraction images often contained a couple of diffraction peaks appearing at random azimuthal positions on the images (Fig. 1D). Convection in the liquid sample could have induced some crystallization at the sample/KCl interface over a very short time scale. Also, the sample temperature was probably slightly below the liquidus temperature, because we observed a clear rim of solid phase just around the melt. We define the liquidus as the temperature at which complete loss of the continuous structure of the diffraction lines was achieved. This temperature corresponds to a clear loss of the three-dimensional solid structure of the sample, with free rotation of a couple of grains in a predominantly liquid fraction.

The temperature gap between the solidus and liquidus is found to increase progressively from 1500 to 2500 K with increasing pressure from 40 to 140 GPa. This gap is much larger than that reported for the chondritic-type mantle. It results in a liquid composition at the solidus, which is very different from the bulk MORB composition (*23*).

Three lines of evidence point to an increase of the SiO_2 content in the liquid with increasing pressure during partial melting of MORB. First, the MORB solidus curve always plots 1000 to 1500 K below the lowest melting curve for pure $CaSiO_3$, $MgSiO_3$, or SiO_2 phases (*24*–*26*) (Fig. 2). Although SiO_2 is the most refractory of these MORB phases at low pressures, it becomes the least refractory above 60 GPa. This suggests a displacement of the pseudo-eutectic composition from Mg-rich liquid (with silica phase on the liquidus) toward Si-rich liquid (with Ca-Pv and/or Mg-Pv on the liquidus) in the (Mg-Pv,

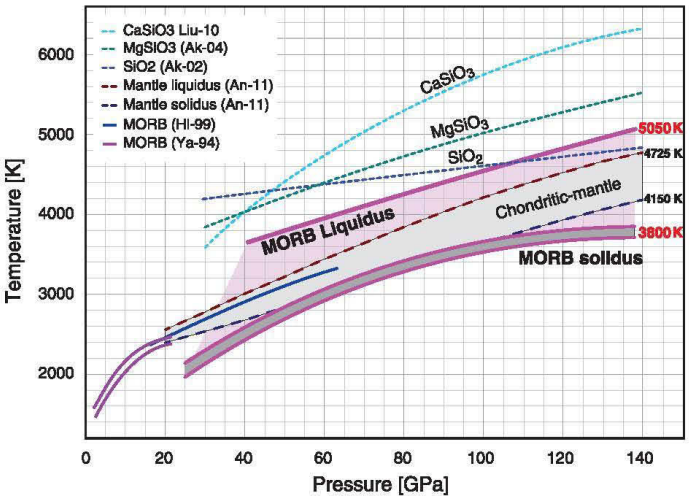

Fig. 2. The MORB solidus and liquidus compared with melting curves of the bulk mantle. At the CMB boundary, the MORB solidus and liquidus reach 3800 (±150) K and 5050 (±300) K, respectively (fig. S3). The curvature of the MORB solidus is much more pronounced than that of chondritic-type mantle (*8*), which induces a lower melting point for the former at 135 GPa, the CMB pressure. The MORB solidus also plots 1000 to 1500 K below the melting curves of pure SiO_2 and $MgSiO_3$, as determined from shockwave experiments (*21*, *22*, *24*–*26*).

Ca-Pv, SiO_2) ternary diagram (fig. S1). A second argument is based on the last phase(s) to disappear from the diffraction patterns at temperatures approaching those of the liquidus. At pressures lower than ~70 GPa, clear peaks of SiO_2 and $CaSiO_3$ remained visible on the diffraction patterns at temperatures between the solidus and liquidus. At higher pressures, SiO_2 peaks disappeared and instead those of Mg-Pv appeared (fig. S6). This indicates a sample undersaturated in SiO_2, with Mg-Pv and Ca-Pv grains coexisting with the liquid at the highest pressures.

A third argument comes from mineralogical and chemical analyses of the recovered samples. After the laser was shut down, we maintained the pressure and made diffraction maps of the quenched molten region of the samples. This corresponds to regions of 30 × 30 or 40 × 40 μm^2, with step resolutions of 2 or 3 μm. The diffraction maps can be treated in series to extract the phase content as a function of the position within the sample (fig. S7). This type of quenched sample generally shows a rim of liquidus phase(s) around the quenched liquid (*13*, *27*). The mineralogical maps of our samples show clearly that the quenched liquid was depleted in the SiO_2 phase and concentrated in Mg-Pv at pressures below ~70 GPa, and the opposite at higher pressures. This indicates an increasing SiO_2 content in the liquid with increasing pressure (fig. S1).

We then made chemical maps of our recovered samples, using a scanning electron microscope (SEM) (supplementary materials, Fig. 3, and fig. S8). At pressures below ~70 GPa, we observed a large amount of MgO in the center of the sample where the liquid had solidified, and the liquid was surrounded by a SiO_2-rich rim. At intermediate pressures, the maps showed similar MgO and SiO_2 content in the liquid as compared to the unheated part of the sample. At the highest pressures, the quenched liquid was enriched in SiO_2 whereas the outer rim was enriched in MgO (fig. S8). MORB partial melting in the lower mantle should always produce liquids with (Mg + Fe + Ca)/Si ratios less than 1, because MORB contains free SiO_2 in addition to Mg-Pv and Ca-Pv refractory phases.

Following the hypothesis that the ULVZ at the D″ layer is associated with partial melting, our experimental results provide explanations for the seismological features. First of all, the nonubiquitous nature of the ULVZ could be due to specific regions where MORB slabs have reached the CMB. The thicknesses of the ULVZ (~40 km) and MORB portion of the subducted slabs [~6 km (*28*)] are of the same order of magnitude. Mantle resistance to the slab penetration, or folding and piling-up at the CMB, could certainly induce thickening of the MORB layer. If temperature in the D″ region is between 3800 and 4150 K, the MORB should be the only material to undergo partial melting (the harzburgitic layer of the subducted slab being more refractory than the pyrolitic or chondritic-type mantle). Because of the large temperature gap found between the MORB solidus and liquidus, low degrees of partial melting are expected in the D″ temperature range. If such liquid eventually percolates and diffuses out of the MORB pile, it will react with the excess (MgFe)O Fp present in the surrounding lower mantle to form $(Mg,Fe)SiO_3$ Mg-Pv. For this reason, the mobility of the liquids extracted from the MORB piles must be extremely limited. Thus, it is not likely that large-scale pockets of liquid will form. It would also explain why seismic shear waves (*Vs*) can propagate through the partially molten ULVZ (*5*).

Also, the decrease of Fp content in the lowermost mantle, resulting from reaction between the bulk mantle and SiO_2-rich liquid, would drive mantle composition toward the perovskitic end-members, in agreement with a recent report (*29*). The loss of Si from the MORB would drive it toward perovskitic end-members (fig. S1). The reaction would eventually stop when the SiO_2 excess in the MORB was exhausted. This would result in the disappearance of the MORB signature, except for minor and trace elements, which could remain concentrated around the ULVZ. This scenario would lead to lower mantle homogenization, in contrast to the chemical segregation generally induced by mantle partial melting. Alternatively, if the MORB proportion is high, Fp could become reactively exhausted, which would imply a lowermost mantle saturated in SiO_2. The answer to these two alternative scenarios depends on how well the underlying harzburgite remains attached to the MORB layer and is entrained into the lowermost mantle. If it is sufficiently abundant, then its reaction with the liquid originating from MORB melting should produce a typical mantle composition such as pyrolite.

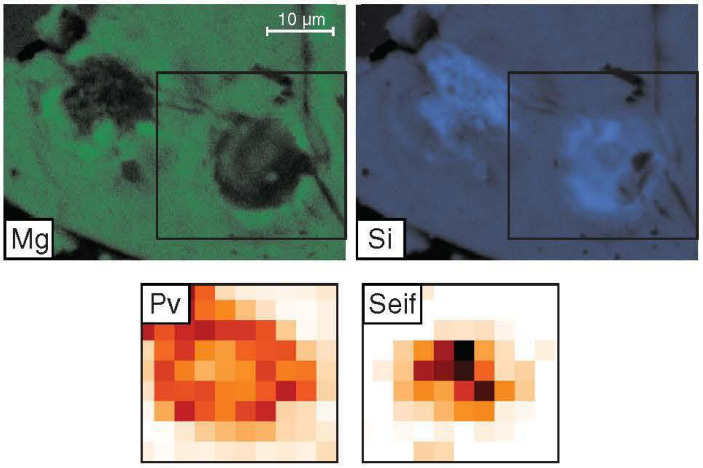

Fig. 3. Phase relations in the sample recovered after partial melting at 120 GPa. The chemical maps (Mg and Si) and mineralogical maps [Mg-Pv and seifertite (Seif)] measured by SEM and x-ray diffraction, respectively, show higher SiO_2 and seifertite contents and lower MgO and Mg-Pv contents in the sample region corresponding to the quenched liquid.

REFERENCES AND NOTES

1. T. Lay, Q. Williams, E. J. Garnero, *Nature* **392**, 461–468 (1998).
2. M. Murakami, K. Hirose, N. Sata, Y. Ohishi, *Geophys. Res. Lett.* **32**, L03304 (2005).
3. S. Labrosse, J. W. Hernlund, N. Coltice, *Nature* **450**, 866–869 (2007).
4. R. D. van der Hilst, H. Karason, *Science* **283**, 1885–1888 (1999).
5. L. Wen, D. V. Helmberger, *Science* **279**, 1701–1703 (1998).
6. S. Rost, E. J. Garnero, Q. Williams, M. Manga, *Nature* **435**, 666–669 (2005).
7. C. W. Thomas, P. D. Asimow, *J. Geophys. Res. Solid Earth* **118**, 5738–5752 (2013).
8. D. Andrault *et al.*, *Earth Planet. Sci. Lett.* **304**, 251–259 (2011).
9. G. Fiquet *et al.*, *Science* **329**, 1516–1518 (2010).
10. T. Katsura, A. Yoneda, D. Yamazaki, T. Yoshino, E. Ito, *Phys. Earth Planet. Inter.* **183**, 212–218 (2010).
11. T. Nakagawa, P. J. Tackley, *Geochem. Geophys. Geosyst.* **11**, Q06001 (2010).
12. N. Bolfan-Casanova, H. Keppler, D. C. Rubie, *Geophys. Res. Lett.* **30**, 1905 (2003).
13. R. Nomura *et al.*, *Science* **343**, 522–525 (2014).
14. T. Irifune, A. E. Ringwood, *Earth Planet. Sci. Lett.* **117**, 101–110 (1993).
15. A. Ricolleau *et al.*, *J. Geophys. Res. Solid Earth* **115**, B08202 (2010).
16. N. Miyajima *et al.*, *Am. Mineral.* **86**, 740–746 (2001).
17. A. R. Pawley, P. F. McMillan, J. R. Holloway, *Science* **261**, 1024–1026 (1993).
18. A. Sano *et al.*, *Geophys. Res. Lett.* **35**, L03303 (2008).
19. M. Nishi *et al.*, *Nat. Geosci.* **7**, 224–227 (2014).
20. Z. M. Geballe, R. Jeanloz, *J. Appl. Phys.* **111**, 123518 (2012).
21. A. Yasuda, T. Fujii, K. Kurita, *J. Geophys. Res. Solid Earth* **99**, 9401 (1994).
22. K. Hirose, Y. W. Fei, Y. Z. Ma, H. K. Mao, *Nature* **397**, 53–56 (1999).
23. P. D. Asimow, M. M. Hirschmann, E. M. Stolper, *Philos. Trans. R. Soc. A Math. Phys. Eng. Sci.* **355**, 255–281 (1997).

24. J. A. Akins, S. N. Luo, P. D. Asimow, T. J. Ahrens, *Geophys. Res. Lett.* **31**, L14612 (2004).
25. J. A. Akins, T. J. Ahrens, *Geophys. Res. Lett.* **29**, 31-1–31-4 (2002).
26. Z. J. Liu *et al.*, *Solid State Commun.* **150**, 590–593 (2010).
27. D. Andrault *et al.*, *Nature* **487**, 354–357 (2012).
28. R. S. White, T. A. Minshull, M. J. Bickle, C. J. Robinson, *J. Petrol.* **42**, 1171–1196 (2001).
29. M. Murakami, Y. Ohishi, N. Hirao, K. Hirose, *Nature* **485**, 90–94 (2012).

ACKNOWLEDGMENTS

We thank M. Benbakkar, J. L. Devidal, A. Fabbrizio, G. Garbarino, P. Parisiadis, V. Svitlyk, and F. van Wyk de Vries for their help and three anonymous reviewers for fruitful comments. The MORB starting material was kindly provided by P. Schiano. This work is supported by Institut National des Sciences de l'Univers, l'European Synchrotron Radiation Facility, and the project Oxydeep of the Agence Nationale de la Recherche. This is Laboratory of Excellence ClerVolc contribution no. 99. All experimental data are presented in the supplementary materials.

SUPPLEMENTARY MATERIALS

www.sciencemag.org/content/344/6186/892/suppl/DC1
Materials and Methods
Supplementary Text
Figs. S1 to S9
Tables S1 and S2
References (*30*–*34*)

6 January 2014; accepted 3 April 2014
10.1126/science.1250466

CORALS AND CLIMATE

Mechanisms of reef coral resistance to future climate change

Stephen R. Palumbi,* Daniel J. Barshis,† Nikki Traylor-Knowles, Rachael A. Bay

Reef corals are highly sensitive to heat, yet populations resistant to climate change have recently been identified. To determine the mechanisms of temperature tolerance, we reciprocally transplanted corals between reef sites experiencing distinct temperature regimes and tested subsequent physiological and gene expression profiles. Local acclimatization and fixed effects, such as adaptation, contributed about equally to heat tolerance and are reflected in patterns of gene expression. In less than 2 years, acclimatization achieves the same heat tolerance that we would expect from strong natural selection over many generations for these long-lived organisms. Our results show both short-term acclimatory and longer-term adaptive acquisition of climate resistance. Adding these adaptive abilities to ecosystem models is likely to slow predictions of demise for coral reef ecosystems.

Reef-building corals have experienced global declines resulting from bleaching events sparked by pulses of warm-water exposure (*1*–*4*). However, corals in naturally warm environments can have high resistance to bleaching temperatures and can survive heat exposure that would bleach conspecifics in cooler microclimates (*5*, *6*). Similarly, recent discovery of populations of acidification-resistant corals show that physiological or evolutionary mechanisms of environmental accommodation exist (*7*, *8*). Such populations are ideal test sites for research into the mechanisms of coral response to climate change.

Corals in adjacent backreef pools in the U.S. National Park of American Samoa on Ofu Island experience strong differences in temperature (*9*, *10*). In the highly variable (HV) pool, temperatures often exceed the local critical bleaching temperature of 30°C, reaching 35°C during strong noontime low tides (*6*). By contrast, the moderately bariable (MV) pool rarely experiences temperatures above 32°C. Corals in the HV Pool have higher growth rates (*9*, *10*), higher survivorship, and higher symbiont photosynthetic efficiency during experimental heat stress than conspecifics from the MV pool (*6*). These pools provide a powerful system to test the speed and extent of coral acclimatization and adaptation to warm-water conditions in the context of future climate change.

Department of Biology, Stanford University, Hopkins Marine Station, Pacific Grove, CA 93950, USA.
*Corresponding author. E-mail: spalumbi@stanford.edu †Present address: Department of Biological Sciences, Old Dominion University, Norfolk, VA 23529, USA.

To test corals in their native habitats for physiological resistance to heat stress, we collected branches of the tabletop coral *Acropora hyacinthus* [cryptic species E (*11*)] and exposed them to experimental bleaching conditions. *A. hyacinthus* is a cosmopolitan species that constitutes a large percentage of hard coral cover on Pacific reefs and shows high levels of bleaching and mortality during large-scale bleaching events (*4*). We chose *A. hyacinthus* for this study because it is a dominant reef-builder and is especially sensitive to environmental stress, making its relative ability to acclimate or adapt extremely important to the future of coral reef ecosystems as climate change proceeds. We subjected branches of corals to a prescribed ramp in water temperature of 29° to 34°C for 3 hours, followed by an incubation for 3 hours at 34°C. These conditions mimic the natural increase in temperature observed in the HV pool during a tidal cycle. Experiments on fragments of tagged and monitored colonies showed that individuals native to the HV pool exhibit higher resistance to thermal stress, measured by retention of chlorophyll derived from photosynthetic symbionts, than corals from the MV pool (Fig. 1). The average retention of chlorophyll a after experimental heat stress was 80% in HV pool corals (Fig. 1C) but only 45% in MV pool corals (Fig. 1A, *t* test, $P < 0.00001$) compared with controls.

To test for acclimatization, we transplanted coral colonies of *A. hyacinthus* reciprocally from their native locations in the HV and MV pools to three transplant sites within each pool. We transplanted 6 colonies from the HV pool and 12 from the MV pool. After 12, 19, and 27 months, we tested transplanted colonies for thermal resistance. For 11 separate colonies, 22 of 23 paired bleaching

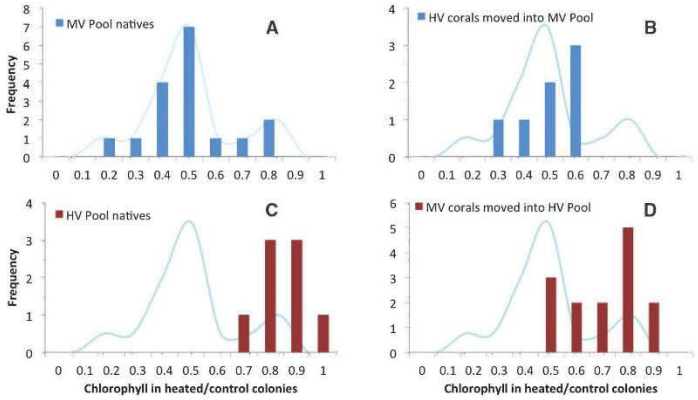

Fig. 1. Chlorophyll retention in coral colonies exposed to experimental heat stress compared with nonstressed controls. Upper panels show results from corals native to the moderately variable (MV) pool (**A**) and from corals moved into the MV pool (**B**). The lower panels are from corals native to the highly variable (HV) pool (**C**) and from corals moved into the HV pool (**D**). The smoothed curve reflects the distribution in (A) and is included in other panels for reference.

Science
AAAS

Supplementary Materials for

Melting of subducted basalt at the core-mantle boundary

Denis Andrault, Giacomo Pesce, Mohamed Ali Bouhifd, Nathalie Bolfan-Casanova, Jean-Marc Hénot, Mohamed Mezouar.

Correspondence to: denis.andrault@univ-bpclermont.fr

This PDF file includes:

Materials and Methods

Methods

We used beveled diamond anvils to achieve pressures from 20 to 135 GPa. Very thin (5-10 μm) flakes of MORB glass were loaded between two KCl pellets of 5 to 10 μm thickness each. Pellets of such thickness minimize axial temperature gradients. No chemical reactions between KCl and our samples could be detected by X-ray diffraction. The glass composition was determined for major and minor elements and for H_2O and CO_2, using an electron microprobe, inductively coupled plasma atomic emission spectroscopy and infrared spectroscopy (Table S1, Fig. S9). To avoid moisture adsorption, all loadings were done using dry powders under N_2-flux in a glove-bag. The data set presented here includes 20 successful high-pressure loadings. The samples were slowly compressed to the target pressure, and heated progressively to the melting temperature. Pressure was determined based on the P-V-T equation of state of Ca-Pv (*30*) or stishovite (*31*) or seifertite above 110 GPa (with similar elastic parameters than stishovite), assuming a negligible effect of Al on volumes (*32*). All phases provide pressure values within the experimental uncertainties of 5%.

Two infrared fiber-lasers produced hot spots 20 μm in diameter on the sample. Temperatures were determined from the sample thermal emission using reflective lenses to prevent any chromatic aberration. Temperature stability was better than 20 K during the 20 seconds of data collection. Temperature reproducibility was estimated at better than 30 K. The total temperature uncertainty was estimated to be 50 K. The solidus temperature is bracketed between the temperatures of rapid grain growth and fast grain

rotation, whose difference remained within 200 K at all pressures investigated in this study. We therefore give the mean temperature between the two values, with an uncertainty of 150 K. Experimental uncertainty of liquidus temperature is higher (±300 K) due to a less precise melting criterion. Each melting point has been determined from the analysis of at least two fresh pieces of sample.

We used X-rays of 0.3738 Å wavelength provided by the ID-27 beamline (ESRF). Two Kirkpatrick-Baez mirrors focused X-rays to a spot of less than 2*2 μm^2 onto the sample. Position of the X-ray beam could be located by the KCl fluorescence. Therefore, combined images of X-ray beam and fiber-lasers could be perfectly positioned on the entrance pinhole of the spectrometer used for temperature measurements. We used the MAR-160 CCD detector. Diffraction patterns were integrated and analyzed using the Fit2d and XRDUA codes, respectively. Before heating, the diffraction patterns did not present a broad band of diffuse scattering as might be expected for the amorphous structure of the compressed MORB. This lack of signal is due to a high diversity of interatomic bonds in this natural glass and because of the thin sample size, which was intentional in order to minimize axial thermal gradients at high temperature.

SEM analyses were performed at 15 keV with a pixel size of less than 0.1x0.1 μm^2. However, due to scattering of the incident electron beam inside the sample, spatial resolution of the chemical analysis is ~1 μm^2. Acquisition time was 20x512µs for each pixel.

Supplementary Text

Chemical segregation in our laser-heated samples

Artefacts generated by chemical diffusion induced by strong thermal gradient such as those generated in the LH-DAC must also be considered. When a silicate sample is subject to excessive thermal gradients, the Soret effect generally induces diffusion of Fe away from the peak temperature. Observation of our chemical maps shows that Fe does not systematically concentrate on the border of the hot spot (Fig. S8), suggesting that Soret diffusion is not dominant in our samples. On the other hand, we are not aware of studies showing significant Soret diffusion for MgO and SiO_2 in mantle silicates. In particular, the low thermal expansion coefficient of SiO_2 suggests a very limited effect of the thermal gradient. We also took great care to minimize axial and vertical temperature gradients in our experimental set-up by the use of relatively thick KCl insulating layers. Therefore, Soret diffusion should not have induced major SiO_2 chemical segregation in our samples. Also, we do not see a reason why the Soret effect would reverse as pressure goes up.

What the geometry of the recovered samples shows instead is that once a large degree of partial melting is achieved (when approaching the liquidus temperature), the liquidus solid phase tends to crystallize at the border of the liquid chamber to form a rim. It implies a drift of the chemical composition of the liquid toward the pseudo-eutectic composition. This compositional drift could be even accentuated by recrystallization of the liquidus phase at the border of the melt pocket when the temperature is rapidly decreased from liquidus to solidus upon quenching. It yields a clear chemical contrast in the recovered samples (Figs. 3, S7 and S8).

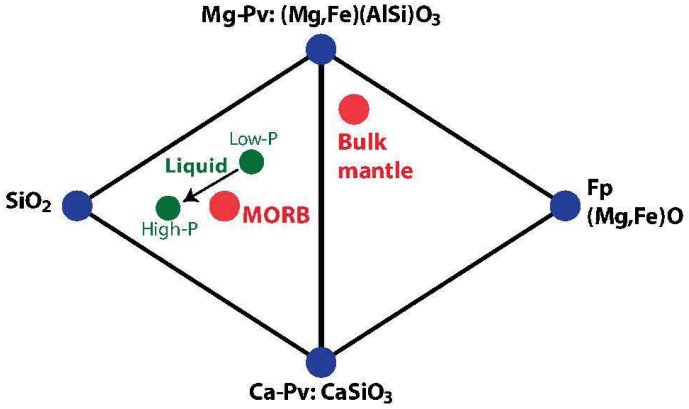

Fig. S1

Adjacent ternary diagrams relevant to bulk-mantle and MORB compositions in the lower mantle. Above 25 GPa, the MORB and bulk-mantle (pyrolitic or chondritic-type) lithologies present (i) common Mg-Pv and Ca-Pv end-member phases, and (ii) opposite SiO_2-phase or Fp end-members, respectively. We represent approximate positions of the MORB, the bulk-mantle, and of the liquid produced by MORB partial melting in the deep mantle. The liquid composition evolves toward the SiO_2 end-member with increasing pressure from 25 to 135 GPa.

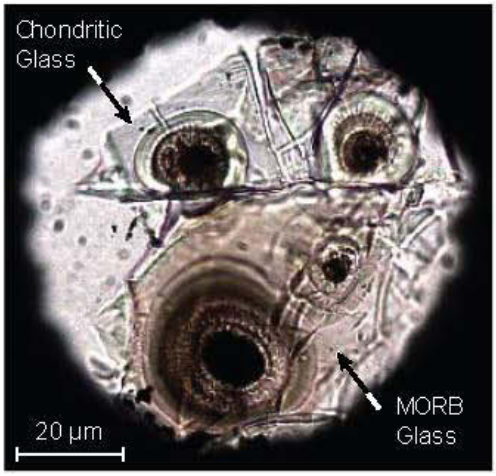

Fig. S2.

Photomicrograph of a sample recovered after partial melting at 46 GPa. Thin flakes of sample are embedded into KCl pellets, which serve as a pressure transmitting medium and thermal insulator against the colder diamonds. Here, we loaded two samples of MORB (lower chip) and chondritic-type mantle (upper chip) compositions, into the same pressure chamber, in order to compare the melting temperature of both materials under the same conditions.

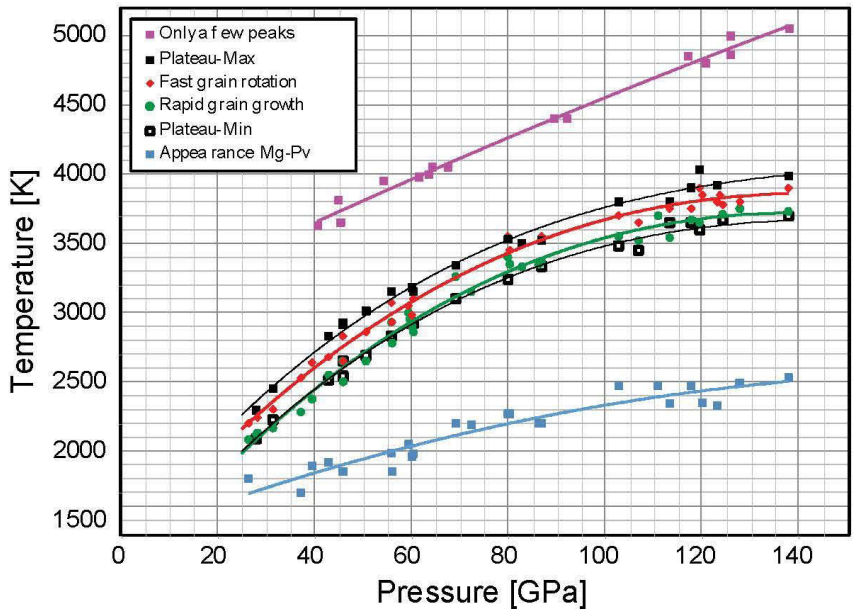

Fig. S3

Experimental criteria used to refine the MORB solidus and liquidus. We report temperatures at which our samples encountered definite structural transformations with increasing temperature (see Table S2). We bracket the MORB solidus between temperatures of appearance of rapid grain growth and fast rotation of large diffraction spots as a function of time. Temperature values for the plateau minimum and maximum are illustrated in Fig. S5.

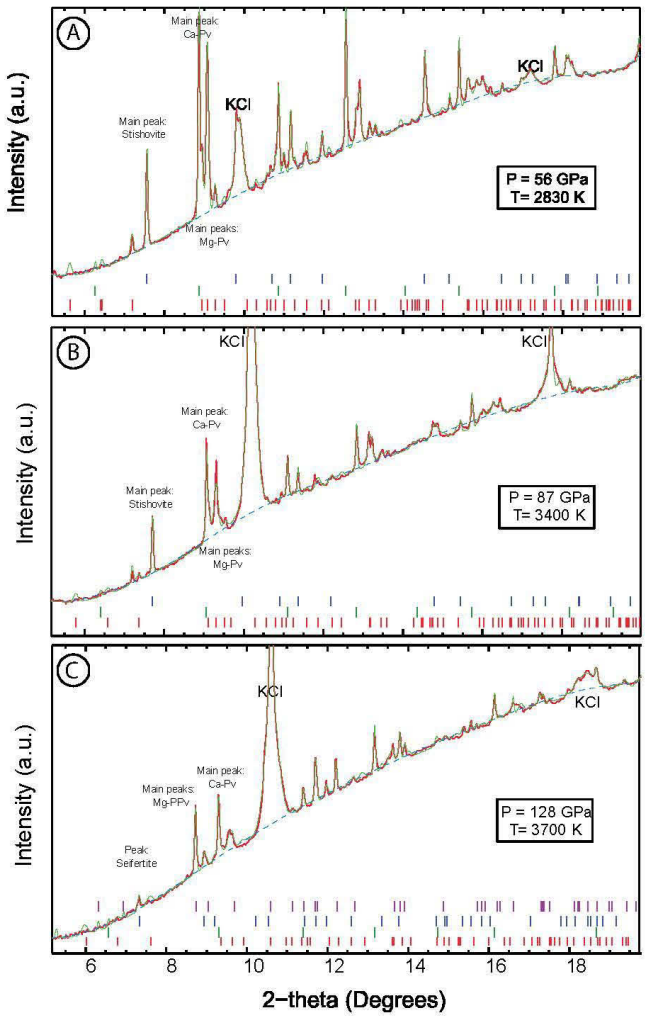

Fig. S4

Sample mineralogy at sub-solidus conditions. We represent typical diffraction patterns recorded at pressures of (a) 56 GPa, (b) 87 GPa and (c) 128 GPa. Red, green and dashed blue curves represent experimental data, Lebail-type refinements and background, respectively. Colored ticks at the bottom of each frame indicate positions of the diffraction peaks for (from bottom to top) Mg-Pv (red), Ca-Pv (green), silica (blue) and Mg-PPv (purple). Above 110 GPa, we observe the occurrence of seifertite (α-PbO_2 form of SiO_2) and post-perovskite ($CaIrO_3$-form of $MgSiO_3$).

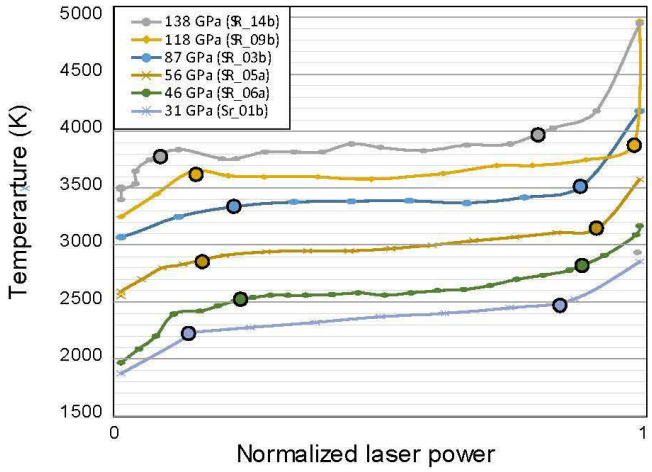

Fig. S5

Temperature plateau observed around solidus temperatures. We report the sample temperature as a function of the laser's power in the temperature domain where the sample encounters major structural changes. There is a clear temperature plateau compatible with onset of partial melting. Large dots correspond to minimum and maximum temperatures on the plateau. Minimum and maximum of the plateau are located at the intersections between straight lines drawn through data points found at temperatures lower, above, and on the plateau.

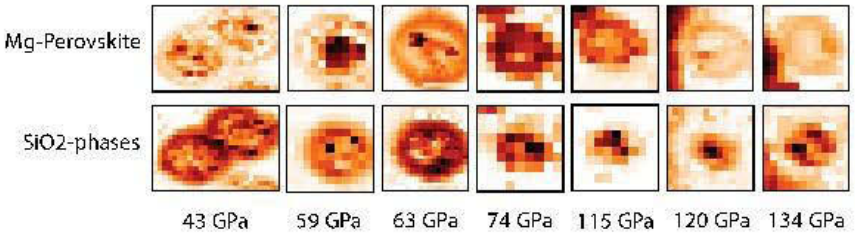

Fig. S7

Mineralogical maps of the recovered samples. The maps show amounts of Mg-perovskite (upper frames) and silica (lower frames) as a function of sample position with increasing pressure. The total height of the frames corresponds to sample sizes of 51, 33, 38, 27, 30, 26, 22 µm with increasing pressure from 43 GPa to 134 GPa. Darker colors represent higher phase contents. In the central part of the circular spots, the quenched liquid appears depleted below 63 GPa, then enriched above 47 GPa, in SiO_2. This is particularly visible for the SiO_2 phase, which spatial repartition in the sample evolves from an external ring to a central spot with increasing pressure. Around the heated zones, the MORB remained a glass, except when other sample regions have also been laser-heated.

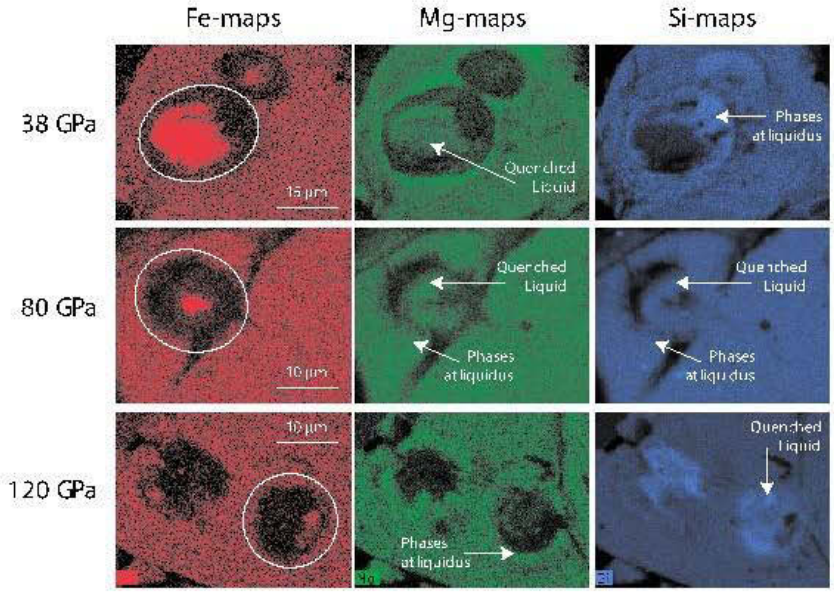

Fig. S8

Chemical maps of the recovered samples. We present the Fe, Mg and Si maps measured on samples recovered after partial melting at 38, 80 and 120 GPa using SEM. Circles indicate the sample region that underwent partially melting. The Si maps show a clear increase of the SiO_2-content in the liquid with increasing pressure. Fe maps show a rather homogeneous liquid (P~38 GPa), a Fp grain which recrystallized after laser shutdown (P~80 GPa), and a poor Fe-concentration in the center, probably due to Fp grains hidden below the sample surface (P~120 GPa).

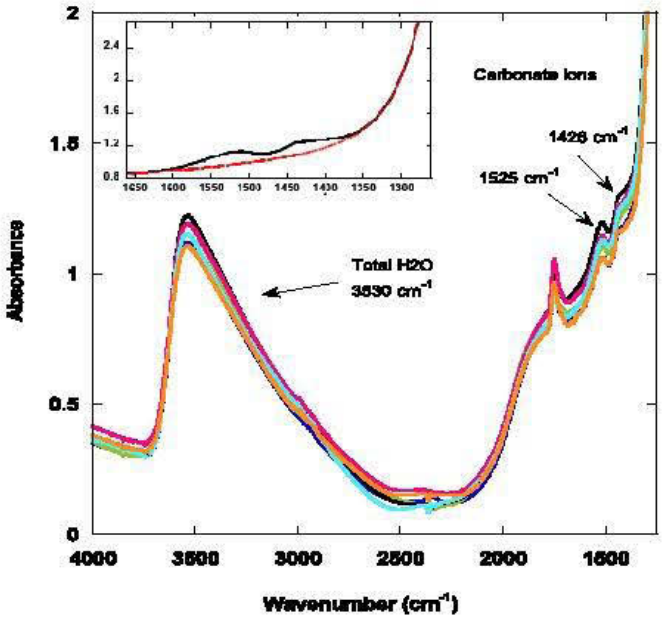

Fig. S9

H_2O and CO_2 content in our natural MORB glass. A glass chip of 270 µm thick of our starting material was analyzed with a Bruker Vertex 70 infrared spectrometer couple to a Hyperion microscope. The water content was determined using the band at 3530 cm^{-1} after subtraction of a linear baseline from 2400 to 3800 cm^{-1}. Applying an extinction coefficient of 78 l/mole/cm (*33*) yields 2730(±140) ppm wt of H_2O averaged over six measurements performed on different sample locations. The CO_2 content was calculated using the bands at 1525 and 1326 cm^{-1} after applying a Voigt +linear baseline (see inset). Using an extinction coefficient of 398 l/mole/cm (*33*), the average intensity over the two bands yields 165(±40) ppm wt CO_2.

Table S1.

Composition of the natural MORB used in this study. We chose a natural glass (DR04) collected at location 6°44' N, 102°36'W during the Searise-1 research cruise as a model composition for MORB (*34*). Upper and lower sub-tables present our chemical analyses using the electron microprobe (except for the S-content taken from (*34*)) and the inductively coupled plasma atomic emission spectroscopy (ICPAES), respectively. Columns "100°C" and "1000°C" correspond to weight loss after 2 hours at 110°C and 1 hour at 1000°C, respectively. The negative value of -0.9% for "1000°C" indicates an increase of the mass related to the oxidation of the Fe-content in this MORB. If we assume ~90% of Fe^{2+} in the starting material (potentially oxidized in Fe^{3+} at high temperature), the sum of H_2O and CO_2 contents should be lower than 3000 ppm (consistent with the following FTIR measurements). Water and CO_2 contents were measured independently using infrared spectroscopy (FTIR) and yield 2730(±140) ppm wt H_2O and 165(±40) ppm wt CO_2 (Fig. S9).

Electron microprobe analyses (wt%; average of 12 points; Numbers in parenthesis are uncertainties):

Na_2O	MgO	Al_2O_3	SiO_2	K_2O	CaO	TiO_2	MnO	FeO	S	Total
2.83 (7)	6.76 (12)	13.73 (18)	50.73 (28)	0.15 (8)	10.94 (22)	2.00 (5)	0.20 (2)	11.29 (13)	0.15	98.79 (50)

Inductively coupled plasma atomic emission spectroscopy. The Total is 98.83(±30):

Na_2O	MgO	Al_2O_3	SiO_2	K_2O	CaO	TiO_2	MnO
2.88 (1)	6.64 (2)	13.51 (20)	49.87 (27)	0.25 (3)	10.73 (2)	2.28 (11)	0.22 (1)
Fe_2O_3	P_2O_5	Ba	Sr	Cr	Ni	110°C	1000°C
13.47 (1)	0.22 (1)	0.0040 (2)	0.0124 (2)	0.0106 (1)	0.0010 (5)	0.66	-0.92

Table S2.

X-ray diffraction results. We report the temperatures (in K) at which the MORB samples encountered definite structural modifications, based on the analysis of the diffraction images. As discussed above, the pressure and temperature uncertainties are 5% of the experimental pressure and 50 K, respectively. See text, Fig. S3 and Fig. 2 for determination of the solidus and liquidus temperatures based on these experimental observations.

Pressure (GPa)	Appearance of Mg-Pv	Rapid grain growth	Fast grain rotation	Minimum of T-plateau	Maximum of T-plateau	Only a few peaks
26,5	1800	2080	2200			
28,1		2120	2280	2090	2295	
28,3		2130	2240			
31,5		2165	2300	2225	2450	3630
37,3	1700	2280	2530			3810
39,6	1890	2375	2640			3650
43,0	1920	2550	2680	2515	2830	
45,9	1850	2650	2830	2650	2925	
46,0		2500	2650	2540	2910	3950
50,7		2650	2860	2690	3010	
56,0	1985	2930	3070	2830	3150	4000
56,1	1850	2780	2930			4050
59,5	2050	3000	3050			
59,8		2950				
60,2	1960	2900	2980	2920	3180	4050
60,5	1980	2860	3100	2925	3150	
69,2	2200	3260		3100	3340	
72,5	2190	3150				
80,0	2270	3400	3550	3240	3530	4400
80,4	2270	3350	3450			
83,0		3330			3500	
86,4	2200	3350				
87,0	2200	3370	3550	3340	3520	4400
102,9	2470	3550	3700	3480	3800	
107,0		3520	3650	3450		
111,1	2470	3700				
113,4	2340	3540	3750	3650	3800	4800
118,0	2470	3670	3750	3650	3900	5000
119,6		3650	3900	3600	4030	
120,2	2350		3850			
123,3	2330		3800		3920	4850
123,9			3850			
128,0	2490	3750	3800			
138,0	2530	3730	3900	3720	3960	5050

References

1. T. Lay, Q. Williams, E. J. Garnero, The core–mantle boundary layer and deep Earth dynamics. *Nature* **392**, 461–468 (1998). doi:10.1038/33083

2. M. Murakami, K. Hirose, N. Sata, Y. Ohishi, Post-perovskite phase transition and mineral chemistry in the pyrolitic lowermost mantle. *Geophys. Res. Lett.* **32**, L03304 (2005). doi:10.1029/2004GL021956

3. S. Labrosse, J. W. Hernlund, N. Coltice, A crystallizing dense magma ocean at the base of the Earth's mantle. *Nature* **450**, 866–869 (2007). doi:10.1038/nature06355 Medline

4. R. D. van der Hilst, H. Karason, Compositional heterogeneity in the bottom 1000 kilometers of Earth's mantle: Toward a hybrid convection model. *Science* **283**, 1885–1888 (1999). doi:10.1126/science.283.5409.1885 Medline

5. L. Wen, D. V. Helmberger, Ultra-low velocity zones near the core-mantle boundary from broadband PKP precursors. *Science* **279**, 1701–1703 (1998). doi:10.1126/science.279.5357.1701 Medline

6. S. Rost, E. J. Garnero, Q. Williams, M. Manga, Seismological constraints on a possible plume root at the core-mantle boundary. *Nature* **435**, 666–669 (2005). doi:10.1038/nature03620 Medline

7. C. W. Thomas, P. D. Asimow, Direct shock compression experiments on premolten forsterite and progress toward a consistent high-pressure equation of state for CaO-MgO-Al_2O_3 - SiO_2-FeO liquids. *J. Geophys. Res. Solid Earth* **118**, 5738–5752 (2013). doi:10.1002/jgrb.50374

8. D. Andrault, N. Bolfan-Casanova, G. L. Nigro, M. A. Bouhifd, G. Garbarino, M. Mezouar, Solidus and liquidus profiles of chondritic mantle: Implication for melting of the Earth across its history. *Earth Planet. Sci. Lett.* **304**, 251–259 (2011). doi:10.1016/j.epsl.2011.02.006

9. G. Fiquet, A. L. Auzende, J. Siebert, A. Corgne, H. Bureau, H. Ozawa, G. Garbarino, Melting of peridotite to 140 gigapascals. *Science* **329**, 1516–1518 (2010). doi:10.1126/science.1192448 Medline

10. T. Katsura, A. Yoneda, D. Yamazaki, T. Yoshino, E. Ito, Adiabatic temperature profile in the mantle. *Phys. Earth Planet. Inter.* **183**, 212–218 (2010). doi:10.1016/j.pepi.2010.07.001

11. T. Nakagawa, P. J. Tackley, Influence of initial CMB temperature and other parameters on the thermal evolution of Earth's core resulting from thermochemical spherical mantle convection. *Geochem. Geophys. Geosyst.* **11**, Q06001 (2010). doi:10.1029/2010GC003031

12. N. Bolfan-Casanova, H. Keppler, D. C. Rubie, Water partitioning at 660 km depth and evidence for very low water solubility in magnesium silicate perovskite. *Geophys. Res. Lett.* **30**, 1905 (2003). doi:10.1029/2003GL017182

13. R. Nomura, K. Hirose, K. Uesugi, Y. Ohishi, A. Tsuchiyama, A. Miyake, Y. Ueno, Low core-mantle boundary temperature inferred from the solidus of pyrolite. *Science* **343**, 522–525 (2014). doi:10.1126/science.1248186 Medline

14. T. Irifune, A. E. Ringwood, Phase transformations in subducted oceanic crust and buoyancy relationships at depths of 600–800 km in the mantle. *Earth Planet. Sci. Lett.* **117**, 101–110 (1993). doi:10.1016/0012-821X(93)90120-X

15. A. Ricolleau, J.-P. Perrillat, G. Fiquet, I. Daniel, J. Matas, A. Addad, N. Menguy, H. Cardon, M. Mezouar, N. Guignot, Phase relations and equation of state of a natural MORB: Implications for the density profile of subducted oceanic crust in the Earth's lower mantle. *J. Geophys. Res. Solid Earth* **115**, B08202 (2010). doi:10.1029/2009JB006709

16. N. Miyajima, T. Yagi, K. Hirose, T. Kondo, K. Fujino, H. Miura, Potential host phase of aluminum and potassium in the Earth's lower mantle. *Am. Mineral.* **86**, 740–746 (2001).

17. A. R. Pawley, P. F. McMillan, J. R. Holloway, Hydrogen in stishovite, with implications for mantle water content. *Science* **261**, 1024–1026 (1993). doi:10.1126/science.261.5124.1024 Medline

18. A. Sano, E. Ohtani, T. Kondo, N. Hirao, T. Sakai, N. Sata, Y. Ohishi, T. Kikegawa, Aluminous hydrous mineral δ-AlOOH as a carrier of hydrogen into the core-mantle boundary. *Geophys. Res. Lett.* **35**, L03303 (2008). doi:10.1029/2007GL031718

19. M. Nishi, T. Irifune, J. Tsuchiya, Y. Tange, Y. Nishihara, K. Fujino, Y. Higo, Stability of hydrous silicate at high pressures and water transport to the deep lower mantle. *Nat. Geosci.* **7**, 224–227 (2014). doi:10.1038/ngeo2074

20. Z. M. Geballe, R. Jeanloz, Origin of temperature plateaus in laser-heated diamond anvil cell experiments. *J. Appl. Phys.* **111**, 123518 (2012). doi:10.1063/1.4729905

21. A. Yasuda, T. Fujii, K. Kurita, Melting phase relations of an anhydrous mid-ocean ridge basalt from 3 to 20 GPa: Implications for the behavior of subducted oceanic crust in the mantle. *J. Geophys. Res. Solid Earth* **99**, 9401 (1994). doi:10.1029/93JB03205

22. K. Hirose, Y. W. Fei, Y. Z. Ma, H. K. Mao, The fate of subducted basaltic crust in the Earth's lower mantle. *Nature* **397**, 53–56 (1999). doi:10.1038/16225

23. P. D. Asimow, M. M. Hirschmann, E. M. Stolper, An analysis of variations in isentropic melt productivity. *Philos. Trans. R. Soc. A Math. Phys. Eng. Sci.* **355**, 255–281 (1997). doi:10.1098/rsta.1997.0009

24. J. A. Akins, S. N. Luo, P. D. Asimow, T. J. Ahrens, Shock-induced melting of $MgSiO_3$ perovskite and implications for melts in Earth's lowermost mantle. *Geophys. Res. Lett.* **31**, L14612 (2004). doi:10.1029/2004GL020237

25. J. A. Akins, T. J. Ahrens, Dynamic compression of SiO_2: A new interpretation. *Geophys. Res. Lett.* **29**, 31-1–31-4 (2002). doi:10.1029/2002GL014806

26. Z. J. Liu, J. Yan, S.-Q. Duan, X.-W. Sun, C.-R. Zhang, Y. Guo, The melting curve of perovskite under lower mantle pressures. *Solid State Commun.* **150**, 590–593 (2010). doi:10.1016/j.ssc.2009.12.038

27. D. Andrault, S. Petitgirard, G. Lo Nigro, J. L. Devidal, G. Veronesi, G. Garbarino, M. Mezouar, Solid-liquid iron partitioning in Earth's deep mantle. *Nature* **487**, 354–357 (2012). doi:10.1038/nature11294 Medline

28. R. S. White, T. A. Minshull, M. J. Bickle, C. J. Robinson, Melt generation at very slow-spreading oceanic ridges: Constraints from geochemical and geophysical data. *J. Petrol.* **42**, 1171–1196 (2001). doi:10.1093/petrology/42.6.1171

29. M. Murakami, Y. Ohishi, N. Hirao, K. Hirose, A perovskitic lower mantle inferred from high-pressure, high-temperature sound velocity data. *Nature* **485**, 90–94 (2012). doi:10.1038/nature11004 Medline

30. S. H. Shim, T. S. Duffy, G. Y. Shen, The stability and P–V–T equation of state of $CaSiO_3$ perovskite in the Earth's lower mantle. *J. Geophys. Res. Solid Earth* **105**, 25955 (2000). doi:10.1029/2000JB900183

31. F. L. Wang, Y. Tange, T. Irifune, K. Funakoshi, *J. Geophys. Res. Solid Earth* **117**, B06209 (2012).

32. N. Bolfan-Casanova, D. Andrault, E. Amiguet, N. Guignot, Equation of state and post-stishovite transformation of Al-bearing silica up to 100GPa and 3000K. *Phys. Earth Planet. Inter.* **174**, 70–77 (2009). doi:10.1016/j.pepi.2008.06.024

33. N. Jendrzejewski, M. Javoy, T. Trull, *C. R. Acad. Sci. Ser. II A* **322**, 645; 735 (1996).

34. P. Schiano, J. L. Birck, C. J. Allegre, Osmium-strontium-neodymium-lead isotopic covariations in mid-ocean ridge basalt glasses and the heterogeneity of the upper mantle. *Earth Planet. Sci. Lett.* **150**, 363–379 (1997). doi:10.1016/S0012-821X(97)00098-8

4. CONCLUSIONS

The present study shows several new important results of melting experiments carried out at pressure and temperature conditions representative of the Earth's mantle. A large variety of both experimental and analytical techniques has been used in this study, in order to properly evaluate how the melting processes affects the dynamics of the mantle, both today and in the early days of our planet's life. High pressure experiments were performed using a multi anvil apparatus (MAA), as well as a diamond anvil cell (DAC) apparatus, allowing coverage of the whole range of pressures of the Earth's mantle.

In particular, we performed melting experiments of a chondritic mantle at pressures up to 25 GPa using MAA. The MAA assemblies used in this study were modified to match the innovative use of in situ X-ray diffraction and in situ electrical conductivity measurements during melting experiment at high pressure. This work demonstrates that both techniques allow detection of very small degrees of partial melting, by monitoring the evolution of the sample in situ during the experiments. A new solidus curve is hence refined from the in situ measurements of electrical conductivity and X-ray diffraction. This study shows that previous experimental reports overestimated solidus temperatures by ~250 K, due to the use of heterogeneous samples and *post mortem* criteria to determine the onset of melting. Namely, (i) the use of a homogeneous glass starting material (contrary to a mixture of oxides), which allows the occurrence of low-degree of partial melting without significant atomic diffusion; (ii) previous studies were based on analysis of recovered samples after "quenched-experiments, leading to the incorrect determination of the solidus temperature due to impossibility of monitoring the experimental process, unlike in situ techniques. Furthermore, the melting criteria of previous studies were based on the disappearance of one mineral from the phase assemblage, which is not necessarily indicative of the solidus temperature of complex chemical systems. My results have two major implications:

i. Firstly, it could help to explain the nature of the low velocity layer (LVL) reported by seismic and magneto-telluric observation in the upper mantle above the 410 km seismic discontinuity (e.g. (Tauzin et al., 2010)). Such anomaly, much alike the low velocity zones (LVZ) in the shallow upper mantle (Lambert and Wyllie, 1970; Romanowicz, 1995a), has long been attributed to the presence of partially molten material, affecting S-wave velocity. The present-day mantle geotherm suggests temperatures well below both the recognised dry upper mantle solidus (see for example (Herzberg and Zhang, 1996; Litasov and Ohtani, 2002)) and the new solidus presented in this study. Therefore, no

major mantle melting can occur today at such mantle depths. The presence of volatiles, known to depress the melting temperature of the mantle (e.g. (Litasov et al., 2014; Tenner et al., 2012)), is therefore required to connect the seismic observations in the upper mantle to the presence of molten material. In this section, the cryoscopic relation reported previously in the literature (Aubaud et al., 2004; Hirschmann et al., 1999) was used in order to model the depression of the new solidus temperatures as a function of the water content. The results shown in this study demonstrate that the presence of as little as 500 ppm of water are sufficient to induce mantle melting at mid upper-mantle depths where the LVL are reported, which is consistent with the maximum water storage capacity of the mantle calculated previously (Ferot and Bolfan-Casanova, 2012).

ii. The second major implication concerns the early state of the Earth's upper mantle. Archean mantle temperatures have been reported to be 200-300 K higher than today, as suggested from the composition of ancient non-arc basalts and komatiites (Herzberg et al., 2010). The higher mantle temperatures would induce partial melting at at mantle depths ranging from ~200 to ~400 km. This persistent shell of partially molten material likely produced a weak layer, which could have disabled the mechanical coupling at the lithosphere–asthenosphere interface (Craig and McKenzie, 1986; Doglioni et al., 2011). This effect would explain absence of deep slab subduction early in the Earth's history. Then, at the Archaean to Proterozoic transition ~2.5 Ga ago, secular mantle cooling had induced a much lower degree of partial melting, eventually enabling global mantle convection and modern plate tectonics.

The new mantle solidus presented in this study has implications on the late crystallization processes in the early magma ocean. Here, the isentropic temperature profile of the mantle was recalculated based on the newly fitted solidus and liquidus temperatures presented in this work. By combining the evolution of the surface potential temperature *Tp* at all mantle depths obtained from our results with an existing relation between time and potential temperature, a model of the cooling of the magma ocean with time was constructed. Our results show that complete crystallization of the magma ocean could take up to 10 My, due to a persistent molten region at the top of the mantle. Additional calculations are however required in order to properly evaluate the effects that external factors (presence of proto-atmosphere, thickness of the thermal boundary layer, and heat flux from the core) on the thermal evolution of the magma ocean through time.

This manuscript also presents the results from in situ synchrotron X-ray diffraction melting experiments on mid-ocean ridge basalts (MORB) using a diamond anvil cell. We determined the MORB solidus and liquidus temperatures at pressures up to ~140 GPa. Our results show that at CMB pressures, the onset of melting occurs at temperatures below the mantle solidus (~350 K). Because of the large temperature gap found between the MORB solidus and liquidus, low degrees of partial melting are expected in the D″ temperature range. Following the hypothesis that the ultra-low velocity zones (ULVZ) observed at the D″ layer are associated to the presence of partial melting, our experimental results provide explanations for these seismological features. The SiO_2-rich liquid generated by the melting of the subducted slab, in fact, would either remain trapped in the MORB material or it would solidify after reacting with the surrounding MgO-rich mantle. Such process would then cause a remixing of the subducted MORB with the lowermost mantle.

REFERENCES

Abe, Y., 1997. Thermal and chemical evolution of the terrestrial magma ocean. Phys. Earth Planet. Inter. 100, 27-39.

Amelin, Y., Krot, A.N., Hutcheon, I.D., Ulyanov, A.A., 2002. Lead isotopic ages of chondrules and calcium-aluminum-rich inclusions. Science 297, 1678-1683.

Anderson, D.L., Sammis, C., 1970. Partial melting in the upper mantle. Phys. Earth Planet. Inter. 3, 41-50.

Andrault, D., Bolfan-Casanova, N., Lo Nigro, G., Bouhifd, M.A., Garbarino, G., Mezouar, M., 2011a. Melting curve of the deep mantle applied to properties of early magma ocean and actual core-mantle boundary. Earth Planet. Sci. Lett. 304, 251-259.

Andrault, D., Bolfan-Casanova, N., Nigro, G.L., Bouhifd, M.A., Garbarino, G., Mezouar, M., 2011b. Solidus and liquidus profiles of chondritic mantle: Implication for melting of the Earth across its history. Earth Planet. Sci. Lett. 304, 251-259.

Andrault, D., Fiquet, G., Itié, J.P., Richet, P., Gillet, P., Häusermann, D., Hanfland, M., 1998. Thermal pressure in a laser-heated diamond-anvil cell: An x-ray diffraction study. European Journal of Mineralogy 10, 931-940.

Andrault, D., Pesce, G., Bouhifd, M.A., Bolfan-Casanova, N., Henot, J.M., Mezouar, M., 2014. Melting of subducted basalt at the core-mantle boundary. Science 344, 892-895.

Andrault, D., Petitgirard, S., Lo Nigro, G., Devidal, J.L., Veronesi, G., Garbarino, G., Mezouar, M., 2012. Solid-liquid iron partitioning in Earth's deep mantle. Nature 487, 354-357.

Aubaud, C., Hauri, E.H., Hirschmann, M.M., 2004. Hydrogen partition coefficients between nominally anhydrous minerals and basaltic melts. Geophys. Res. Lett. 31.

Bean, V., Akimoto, S., Bell, P., Block, S., Holzapfel, W., Manghnani, M., Nicol, M., Stishov, S., 1986. Another step toward an international practical pressure scale: 2nd AIRAPT IPPS task group report. Physica B+ C 139, 52-54.

Bercovici, D., Karato, S.-i., 2003a. Whole-mantle convection and the transition-zone water filter. Nature 425, 39-44.

Bercovici, D., Karato, S., 2003b. Whole-mantle convection and the transition-zone water filter. Nature 425, 39-44.

Bose, K., Ganguly, J., 1995. Quartz-coesite transition revisited: Reversed experimental determination at 500-1200 ºC and retrieved thermochemical properties. Am. Miner. 80, 231-238.

Boujibar, A., Andrault, D., Bolfan-Casanova, N., Bouhifd, M.A., Monteux, J., 2015. Cosmochemical fractionation by collisional erosion during the Earth's accretion. Nat. Commun. 6.

Boyet, M., Carlson, R.W., 2005. Nd-142 evidence for early (> 4.53 Ga) global differentiation of the silicate Earth. Science 309, 576-581.

Burkhardt, C., Borg, L.E., Brennecka, G.A., Shollenberger, Q.R., Dauphas, N., Kleine, T., 2016. A nucleosynthetic origin for the Earth's anomalous 142Nd composition. Nature 537, 394-398.

Campbell, I.H., O'Neill, H.S.C., 2012. Evidence against a chondritic Earth. Nature 483, 553-558.

Caro, G., Bourdon, B., Halliday, A.N., Quitte, G., 2008. Super-chondritic Sm/Nd ratios in Mars, the Earth and the Moon. Nature 452, 336-339.

Corgne, A., Allan, N.L., Wood, B.J., 2003. Atomistic simulations of trace element incorporation into the large site of MgSiO3 and CaSiO3 perovskites. Phys. Earth Planet. Inter. 139, 113-127.

Craig, C.H., McKenzie, D., 1986. The existence of a thin low-viscosity layer beneath the lithosphere. Earth Planet. Sci. Lett. 78, 420-426.

Dasgupta, R., Hirschmann, M.M., 2006. Melting in the Earth's deep upper mantle caused by carbon dioxide. Nature 440, 659-662.

Dasgupta, R., Hirschmann, M.M., 2010. The deep carbon cycle and melting in Earth's interior. Earth Planet. Sci. Lett. 298, 1-13.

Davaille, A., 1999. A simultaneous generation of hotpots and superswells by convection in a heterogeneous planetary mantle. Nature 402, 756-760.

Davies, C., Pozzo, M., Gubbins, D., Alfe, D., 2015. Constraints from material properties on the dynamics and evolution of Earth[rsquor]s core. Nature Geosci 8, 678-685.

Davis, F.A., Hirschmann, M.M., Humayun, M., 2011. The composition of the incipient partial melt of garnet peridotite at 3 GPa and the origin of OIB. Earth Planet. Sci. Lett. 308, 380-390.

De Nolf, W., Vanmeert, F., Janssens, K., 2014. XRDUA: crystalline phase distribution maps by two-dimensional scanning and tomographic (micro) X-ray powder diffraction. Journal of Applied Crystallography 47, 1107-1117.

Doglioni, C., Ismail-Zadeh, A., Panza, G., Riguzzi, F., 2011. Lithosphere-asthenosphere viscosity contrast and decoupling. Phys. Earth Planet. Inter. 189, 1-8.

Drake, M.J., Righter, K., 2002. Determining the composition of the Earth. Nature 416, 39-44.

Dziewonski, A., Anderson, D., 1981. Preliminary reference Earth model. Phys. Earth Planet. Inter. 25, 297-356.

Ferot, A., Bolfan-Casanova, N., 2012. Water storage capacity in olivine and pyroxene to 14 GPa: Implications for the water content of the Earth's upper mantle and nature of seismic discontinuities. Earth Planet. Sci. Lett. 349, 218-230.

Fiquet, G., Auzende, A.L., Siebert, J., Corgne, A., Bureau, H., Ozawa, H., Garbarino, G., 2010. Melting of Peridotite to 140 Gigapascals. Science 329, 1516-1518.

Foley, B.J., Bercovici, D., Elkins-Tanton, L.T., 2014. Initiation of plate tectonics from post-magma ocean thermochemical convection. J. Geophys. Res.: Solid Earth 119, 8538-8561.

Frost, D.J., 2008. The upper mantle and transition zone. Elements 4, 171-176.

Gaillard, F., 2004. Laboratory measurements of electrical conductivity of hydrous and dry silicic melts under pressure. Earth Planet. Sci. Lett. 218, 215-228.

Gaillard, F., Malki, M., Iacono-Marziano, G., Pichavant, M., Scaillet, B., 2008. Carbonatite Melts and Electrical Conductivity in the Asthenosphere. Science 322, 1363-1365.

Gaillard, F., Marziano, G.I., 2005. Electrical conductivity of magma in the course of crystallization controlled by their residual liquid composition. Journal of Geophysical Research: Solid Earth 110.

Garnero, E.J., McNamara, A.K., 2008. Structure and dynamics of Earth's lower mantle. Science 320, 626-628.

Gerya, T., 2014. Precambrian geodynamics: Concepts and models. Gondwana Research 25, 442-463.

Gessmann, C.K., Wood, B.J., Rubie, D.C., Kilburn, M.R., 2001. Solubility of silicon in liquid metal at high pressure: implications for the composition of the Earth's core. Earth Planet. Sci. Lett. 184, 367-376.

Ghosh, S., Ohtani, E., Litasov, K.D., Terasaki, H., 2009. Solidus of carbonated peridotite from 10 to 20 GPa and origin of magnesiocarbonatite melt in the Earth's deep mantle. Chemical Geology 262, 17-28.

Green, D.H., Hibberson, W.O., Rosenthal, A., Kovács, I., Yaxley, G.M., Falloon, T.J., Brink, F., 2014. Experimental study of the influence of water on melting and phase assemblages in the upper mantle. Journal of Petrology 55, 2067-2096.

Hall, H.T., 1958. Some High-Pressure, High-Temperature Apparatus Design Considerations: Equipment for Use at 100 000 Atmospheres and 3000°C. Review of Scientific Instruments 29, 267.

Hamano, K., Abe, Y., Genda, H., 2013. Emergence of two types of terrestrial planet on solidification of magma ocean. Nature 497, 607-610.

Hennet, L., Cristiglio, V., Kozaily, J., Pozdnyakova, I., Fischer, H.E., Bytchkov, A., Drewitt, J.W.E., Leydier, M., Thiaudiere, D., Gruner, S., Brassamin, S., Zanghi, D., Cuello, G.J., Koza, M., Magazu, S., Greaves, G.N., Price, D.L., 2011. Aerodynamic levitation and laser heating: Applications at synchrotron and neutron sources. Eur. Phys. J.-Spec. Top. 196, 151-165.

Hennet, L., Pozdnyakova, I., Bytchkov, A., Cristiglio, V., Palleau, P., Fischer, H.E., Cuello, G.J., Johnson, M., Melin, P., Zanghi, D., Brassamin, S., Brun, J.F., Price, D.L., Saboungi, M.L., 2006. Levitation apparatus for neutron diffraction investigations on high temperature liquids. Review of Scientific Instruments 77.

Hernlund, J., Leinenweber, K., Locke, D., Tyburczy, J.A., 2006. A numerical model for steady-state temperature distributions in solid-medium high-pressure cell assemblies. Am. Miner. 91, 295-305.

Herzberg, C., Condie, K., Korenaga, J., 2010. Thermal history of the Earth and its petrological expression. Earth Planet. Sci. Lett. 292, 79-88.

Herzberg, C., Raterron, P., Zhang, J., 2000a. New experimental observations on the anhydrous solidus for peridotite KLB-1. Geochem., Geophys., Geosyst. 1.

Herzberg, C., Raterron, P., Zhang, J., 2000b. New experimental observations on the anhydrous solidus for peridotite KLB-1. Geochemistry, Geophysics, Geosystems 1.

Herzberg, C., Zhang, J., 1996. Melting experiments on anhydrous peridotite KLB-1: compositions of magmas in the upper mantle and transition zone. 101, 8271-8295.

Hirano, N., Takahashi, E., Yamamoto, J., Abe, N., Ingle, S.P., Kaneoka, I., Hirata, T., Kimura, J.-I., Ishii, T., Ogawa, Y., Machida, S., Suyehiro, K., 2006. Volcanism in response to plate flexure. Science 313, 1426-1428.

Hirose, K., Komabayashi, T., Murakami, M., Funakoshi, K.i., 2001. In situ measurements of the majorite-akimotoite-perovskite phase transition boundaries in MgSiO3. Geophys. Res. Lett. 28, 4351-4354.

Hirose, K., Kushiro, I., 1993. Partial melting of dry peridotite at high-pressures - Determination of compositions of melts segregated from peridotite using aggregates of diamonds. Earth Planet. Sci. Lett. 114, 477-489.

Hirschmann, M.M., 2000. Mantle solidus: Experimental constraints and the effects of peridotite composition. Geochem., Geophys., Geosyst. 1.

Hirschmann, M.M., 2010. Partial melt in the oceanic low velocity zone. Phys. Earth Planet. Inter. 179, 60-71.

Hirschmann, M.M., Asimow, P.D., Ghiorso, M.S., Stolper, E.M., 1999. Calculation of peridotite partial melting from thermodynamic models of minerals and melts. III. Controls on isobaric melt production and the effect of water on melt production. Journal of Petrology 40, 831-851.

Ito, E., 2007. 2.08 - Theory and Practice – Multianvil Cells and High-Pressure Experimental Methods, in: Schubert, G. (Ed.), Treatise on Geophysics. Elsevier, Amsterdam, pp. 197-230.

Iwamori, H., McKenzie, D., Takahashi, E., 1995. Melt generation by isentropic mantle upwelling. Earth Planet. Sci. Lett. 134, 253-266.

Jeffreys, H., Bullen, K., 1940. Seismological Tables. British Association for the Advancement of Science. Gray Milne Trust.

Kamber, B.S., 2015. The evolving nature of terrestrial crust from the Hadean, through the Archaean, into the Proterozoic. Precambrian Research 258, 48-82.

Karato, S.-I., 2014. Does partial melting explain geophysical anomalies? Phys. Earth Planet. Inter. 228, 300-306.

Katsura, T., Yamada, H., Nishikawa, O., Song, M., Kubo, A., Shinmei, T., Yokoshi, S., Aizawa, Y., Yoshino, T., Walter, M.J., Ito, E., Funakoshi, K., 2004. Olivine-wadsleyite transition in the system (Mg,Fe)2SiO4. Journal of Geophysical Research 109, B2.

Katsura, T., Yoneda, A., Yamazaki, D., Yoshino, T., Ito, E., 2010. Adiabatic temperature profile in the mantle. Phys. Earth Planet. Inter. 183, 212-218.

Kawai, N., Endo, S., 1970. The Generation of Ultrahigh Hydrostatic Pressures by a Split Sphere Apparatus. Review of Scientific Instruments 41, 1178-1181.

Kawakatsu, H., Kumar, P., Takei, Y., Shinohara, M., Kanazawa, T., Araki, E., Suyehiro, K., 2009. Seismic Evidence for Sharp Lithosphere-Asthenosphere Boundaries of Oceanic Plates. Science 324, 499-502.

Kellogg, L.H., Hager, B.H., van der Hilst, R.D., 1999. Compositional Stratification in the Deep Mantle. Science 283, 1881-1884.

Kojitani, H., Akaogi, M., 1997. Melting enthalpies of mantle peridotite: calorimetric determinations in the system CaO-MgO-Al2O3-SiO2 and application to magma generation. Earth Planet. Sci. Lett. 153, 209-222.

Labrosse, S., 2015. Thermal evolution of the core with a high thermal conductivity. Phys. Earth Planet. Inter. 247, 36-55.

Labrosse, S., Hernlund, J.W., Coltice, N., 2007. A crystallizing dense magma ocean at the base of the Earth's mantle. Nature 450, 866-869.

Lambert, I.B., Wyllie, P.J., 1970. Melting in the deep crust and upper mantle and the nature of the low velocity layer. Phys. Earth Planet. Inter. 3, 316-322.

Laporte, D., Toplis, M.J., Seyler, M., Devidal, J.L., 2004. A new experimental technique for extracting liquids from peridotite at very low degrees of melting: application to partial melting of depleted peridotite. Contributions to Mineralogy and Petrology 146, 463-484.

Lay, T., Garnero, E.J., Williams, Q., 2004. Partial melting in a thermo-chemical boundary layer at the base of the mantle. Physics of the Earth and Planetary Interior 146, 441-467.

Lebrun, T., Massol, H., Chassefiere, E., Davaille, A., Marcq, E., Sarda, P., Leblanc, F., Brandeis, G., 2013. Thermal evolution of an early magma ocean in interaction with the atmosphere. J. Geophys. Res.: Planets 118, 1155-1176.

Letoullec, R., Pinceaux, J.P., Loubeyre, P., 1988. The membrane diamond anvil cell: A new device for generating continuous pressure and temperature variations. High Pressure Research 1, 77-90.

Litasov, K., Ohtani, E., 2002. Phase relations and melt compositions in CMAS–pyrolite–H2O system up to 25 GPa. Phys. Earth Planet. Inter. 134, 105-127.

Litasov, K.D., Ohtani, E., 2009. Solidus and phase relations of carbonated peridotite in the system CaO–Al 2 O 3–MgO–SiO 2–Na 2 O–CO 2 to the lower mantle depths. Phys. Earth Planet. Inter. 177, 46-58.

Litasov, K.D., Shatskiy, A., Ohtani, E., 2014. Melting and subsolidus phase relations in peridotite and eclogite systems with reduced C-O-H fluid at 3-16 GPa. Earth Planet. Sci. Lett. 391, 87-99.

Lupu, R.E., Zahnle, K., Marley, M.S., Schaefer, L., Fegley, B., Morley, C., Cahoy, K., Freedman, R., Fortney, J.J., 2014. THE ATMOSPHERES OF EARTHLIKE PLANETS AFTER GIANT IMPACT EVENTS. Astrophysical Journal 784.

Magni, V., Bouilhol, P., van Hunen, J., 2014. Deep water recycling through time. Geochem., Geophys., Geosyst. 15, 4203-4216.

Manthilake, M., Matsuzaki, T., Yoshino, T., Yamashita, S., Ito, E., Katsura, T., 2009. Electrical conductivity of wadsleyite as a function of temperature and water content. Phys. Earth Planet. Inter. 174, 10-18.

Mao, H.K., Bell, P.M., 1978. HIGH-PRESSURE PHYSICS - SUSTAINED STATIC GENERATION OF 1.36 TO 1.72 MEGABARS. Science 200, 1145-1147.

Martin, H., Moyen, J.F., 2002. Secular changes in tonalite-trondhjemite-granodiorite composition as markers of the progressive cooling of Earth. Geology 30, 319-322.

Martin, H., Moyen, J.F., Guitreau, M., Blichert-Toft, J., Le Pennec, J.L., 2014. Why Archaean TTG cannot be generated by MORB melting in subduction zones. Lithos 198, 1-13.

Matsukage, K.N., Jing, Z.C., Karato, S., 2005. Density of hydrous silicate melt at the conditions of Earth's deep upper mantle. Nature 438, 488-491.

Maumus, J., Bagdassarov, N., Schmeling, H., 2005. Electrical conductivity and partial melting of mafic rocks under pressure. Geochim. Cosmochim. Acta 69, 4703-4718.

Melosh, H.J., 1990. Giant impacts and the thermal state of the early Earth. Oxford University Press, New York.

Merrill, L., Bassett, W.A., 1974. MINIATURE DIAMOND ANVIL PRESSURE CELL FOR SINGLE-CRYSTAL X-RAY-DIFFRACTION STUDIES. Review of Scientific Instruments 45, 290-294.

Mierdel, K., Keppler, H., Smyth, J.R., Langenhorst, F., 2007. Water solubility in aluminous orthopyroxene and the origin of Earth's asthenosphere. Science 315, 364-368.

Monteux, J., Andrault, D., Samuel, H., 2016. On the cooling of a deep terrestrial magma ocean. Earth Planet. Sci. Lett. submitted.

Mosenfelder, J.L., Asimow, P.D., Frost, D.J., Rubie, D.C., Ahrens, T.J., 2009. The $MgSiO_3$ system at high pressure: Thermodynamic properties of perovskite, postperovskite, and melt from global inversion of shock and static compression data. J. Geophys. Res.: Solid Earth 114, B01203.

Mukhopadhyay, S., 2012. Early differentiation and volatile accretion recorded in deep-mantle neon and xenon. Nature 486, 101-104.

Murakami, M., Hirose, K., Kawamura, K., Sata, N., Ohishi, Y., 2004. Post-perovskite phase transition in MgSiO3. Science 304, 855-858.

Nakagawa, T., Tackley, P.J., 2010. Influence of initial CMB temperature and other parameters on the thermal evolution of Earth's core resulting from thermochemical spherical mantle convection. Geochem., Geophys., Geosyst. 11, Q06001.

Nakajima, M., Stevenson, D.J., 2015. Melting and Mixing States of the Earth's Mantle after the Moon-Forming Impact. Earth Planet. Sci. Lett., in press.

Ni, H., Keppler, H., Behrens, H., 2011. Electrical conductivity of hydrous basaltic melts: implications for partial melting in the upper mantle. Contributions to Mineralogy and Petrology 162, 637-650.

Nomura, R., Hirose, K., Uesugi, K., Ohishi, Y., Tsuchiyama, A., Miyake, A., Ueno, Y., 2014. Low Core-Mantle Boundary Temperature Inferred from the Solidus of Pyrolite. Science 343, 522-525.

Nomura, R., Ozawa, H., Tateno, S., Hirose, K., Hernlund, J.W., Muto, S., Ishii, H., Hiraoka, N., 2011. Spin crossover and iron-rich silicate melt in the Earth's deep mantle. Nature 473, 199-202.

Novella, D., Frost, D.J., 2014. The Composition of Hydrous Partial Melts of Garnet Peridotite at 6 GPa: Implications for the Origin of Group II Kimberlites. Journal of Petrology 55, 2097-2123.

Partzsch, G.M., Schilling, F.R., Arndt, J., 2000. The influence of partial melting on the electrical behavior of crustal rocks: laboratory examinations, model calculations and geological interpretations. Tectonophysics 317, 189-203.

Pearson, D., Brenker, F., Nestola, F., McNeill, J., Nasdala, L., Hutchison, M., Matveev, S., Mather, K., Silversmit, G., Schmitz, S., 2014. Hydrous mantle transition zone indicated by ringwoodite included within diamond. Nature 507, 221-224.

Presnall, D., Simmons, C., Porath, H., 1972. Changes in electrical conductivity of a synthetic basalt during melting. Journal of Geophysical Research 77, 5665-5672.

Priestley, K., McKenzie, D., 2013. The relationship between shear wave velocity, temperature, attenuation and viscosity in the shallow part of the mantle. Earth Planet. Sci. Lett. 381, 78-91.

Revenaugh, J., Sipkin, S.A., 1994. SEISMIC EVIDENCE FOR SILICATE MELT ATOP THE 410 KM MANTLE DISCONTINUITY. Nature 369, 474-476.

Ringwood, A.E., 1970. Phase Transformations and the Constitution of the Mantle. Phys. Earth Planet. Inter. 3, 109-155.

Roberts, J.J., Tyburczy, J.A., 1991. Frequency dependent electrical properties of polycrystalline olivine compacts. Journal of Geophysical Research: Solid Earth 96, 16205-16222.

Romanowicz, B., 1995a. A global tomographic model of shear attenuation in the upper mantle. Journal of Geophysical Research: Solid Earth 100, 12375-12394.

Romanowicz, B., 1995b. A global tomographic model of the shear attenuation in the upper mantle. J. Geophys. Res.: Solid Earth 100, 12375-12394.

Rost, S., Garnero, E.J., Williams, Q., Manga, M., 2005. Seismological constraints on a possible plume root at the core-mantle boundary. Nature 435, 666-669.

Rubie, D.C., Nimmo, F., Melosh, H.J., 2015. 9.03 - Formation of the Earth's Core A2 - Schubert, Gerald, Treatise on Geophysics (Second Edition). Elsevier, Oxford, pp. 43-79.

Sakamaki, T., Suzuki, A., Ohtani, E., 2006. Stability of hydrous melt at the base of the Earth's upper mantle. Nature 439, 192-194.

Sato, H., Ida, Y., 1984. Low frequency electrical impedance of partially molten gabbro: The effect of melt geometry on electrical properties. Tectonophysics 107, 105-134.

Sato, H., Sacks, I.S., Murase, T., 1989. The use of laboratory velocity data for estimating temperature and partial melt fraction in the low-velocity zone: Comparison with heat flow and electrical conductivity studies. Journal of Geophysical Research: Solid Earth 94, 5689-5704.

Sifre, D., Gardes, E., Massuyeau, M., Hashim, L., Hier-Majumder, S., Gaillard, F., 2014. Electrical conductivity during incipient melting in the oceanic low-velocity zone. Nature 509, 81-85.

Simon, F., Glatzel, G., 1929. Fusion-pressure curve. Zeitschrift für anorganische und allgemeine Chemie 178, 309-316.

Sinmyo, R., Hirose, K., 2010. The Soret diffusion in laser-heated diamond-anvil cell. Phys. Earth Planet. Inter., doi:10.1016/j.pepi.2009.1010.1011.

Sleep, N.H., Zahnle, K.J., Lupu, R.E., 2014. Terrestrial aftermath of the Moon-forming impact. Philos. Trans. R. Soc., A 372.

Solomatov, V., 2007. Magma Oceans and Primordial Mantle Differentiation, in: Schubert, G. (Ed.), Treatise on Geophysics. Elsevier, Amsterdam, pp. 91-119.

Solomatov, V.S., 2015. Magma Oceans and Primordial Mantle Differentiation, in: Schubert, G. (Ed.), Treatise on Geophysics, 2 ed. Elsevier, Amsterdam, pp. 81-104.

Solomon, S.C., 1972. Seismic-wave attenuation and partial melting in the upper mantle of North America. Journal of Geophysical Research 77, 1483-1502.

Song, T.R.A., Helmberger, D.V., Grand, S.P., 2004. Low-velocity zone atop the 410-km seismic discontinuity in the northwestern United States. Nature 427, 530-533.

Stixrude, L., Lithgow-Bertelloni, C., 2005. Mineralogy and elasticity of the oceanic upper mantle: Origin of the low-velocity zone. J. Geophys. Res.: Solid Earth 110.

Stutzmann, E., Vinnik, L., Ferreira, A., Singh, S., 2000. Constraint on the S-wave velocity at the base of the mantle. Geophys. Res. Lett. 27, 1571-1574.

Susaki, J.-l., Akaogi, M., Akimoto, S., Shimomura, O., 1985. Garnet-perovskite transformation in CaGeO3: In-situ X-ray measurements using synchrotron radiation. Geophys. Res. Lett. 12, 729-732.

Suzuki, A., Ohtani, E., Morishima, H., Kubo, T., Kanbe, Y., Kondo, T., Okada, T., Terasaki, H., Kato, T., Kikegawa, T., 2000. In situ determination of the phase boundary between wadsleyite and ringwoodite in Mg2SiO4. Geophys. Res. Lett. 27, 803-806.

Takafuji, N., Hirose, K., Mitome, M., Bando, Y., 2005. Solubilities of O and Si in liquid iron in equilibrium with (Mg,Fe)SiO3 perovskite and the light elements in the core. Geophys. Res. Lett. 32, L06313.

Takahashi, E., 1986. Melting of a dry peridotite KLB-1 up to 14 GPa: Implications on the origin of peridotitic upper mantle. Journal of Geophysical Research: Solid Earth 91, 9367-9382.

Tan, Y., Helmberger, D.V., 2007. Trans-Pacific upper mantle shear velocity structure. J. Geophys. Res.: Solid Earth 112.

Tauzin, B., Debayle, E., Wittlinger, G., 2010. Seismic evidence for a global low-velocity layer within the Earth's upper mantle. Nat. Geosci. 3, 718-721.

Tenner, T.J., Hirschmann, M.M., Humayun, M., 2012. The effect of H2O on partial melting of garnet peridotite at 3.5 GPa. Geochem., Geophys., Geosyst. 13.

Thomas, C.W., Asimow, P.D., 2013. Direct shock compression experiments on premolten forsterite and progress toward a consistent high-pressure equation of state for CaO-MgO-Al2O3-SiO2-FeO liquids. J. Geophys. Res.: Solid Earth 118, 5738-5752.

Thorne, M.S., Garnero, E.J., 2004. Inferences on ultralow-velocity zone structure from a global analysis of SPdKS waves. Journal of Geophysical Research: Solid Earth 109.

Thybo, H., 2006. The heterogeneous upper mantle low velocity zone. Tectonophysics 416, 53-79.

Touboul, M., Puchtel, I.S., Walker, R.J., 2012. 182W evidence for long-term preservation of early mantle differentiation products. Science 335, 1065-1069.

Tronnes, R.G., Frost, D.J., 2002. Peridotite melting and mineral–melt partitioning of major and minor elements at 22–24.5 GPa. Earth Planet. Sci. Lett. 197, 117-131.

van Hunen, J., Moyen, J.-F., 2012. Archean Subduction: Fact or Fiction?, in: Jeanloz, R. (Ed.), Annual Review of Earth and Planetary Sciences, Vol 40, pp. 195-219.

Vinnik, L., Farra, V., 2007. Low S velocity atop the 410-km discontinuity and mantle plumes. Earth Planet. Sci. Lett. 262, 398-412.

Walter, M.J., 1998. Melting of garnet peridotite and the origin of komatiite and depleted lithosphere. Journal of Petrology 39, 29-60.

Wang, Y.B., Uchida, T., Von Dreele, R., Rivers, M.L., Nishiyama, N., Funakoshi, K., Nozawa, A., Kaneko, H., 2004. A new technique for angle-dispersive powder diffraction using an energy-dispersive setup and synchrotron radiation. Journal of Applied Crystallography 37, 947-956.

Wen, L., Helmberger, D.V., 1998. Ultra-Low Velocity Zones Near the Core-Mantle Boundary from Broadband PKP Precursors. Science 279, 1701-1703.

Williams, Q., Garnero, E.J., 1996. Seismic evidence for partial melt at the base of Earth's mantle. Science 273, 1528-1530.

Yamazaki, D., Kato, T., Ohtani, E., Toriumi, M., 1996. Grain growth rates of MgSiO3 perovskite and periclase under lower mantle conditions. Science 274, 2052-2054.

Yoshino, T., 2010. Laboratory Electrical Conductivity Measurement of Mantle Minerals. Surveys in Geophysics 31, 163-206.

Yoshino, T., Laumonier, M., McIsaac, E., Katsura, T., 2010. Electrical conductivity of basaltic and carbonatite melt-bearing peridotites at high pressures: Implications for melt distribution and melt fraction in the upper mantle. Earth Planet. Sci. Lett. 295, 593-602.

Yoshino, T., Matsuzaki, T., Shatskiy, A., Katsura, T., 2009. The effect of water on the electrical conductivity of olivine aggregates and its implications for the electrical structure of the upper mantle. Earth Planet. Sci. Lett. 288, 291-300.

Zahnle, K.J., Kastings, J.F., Pollack, J.B., 1988. Evolution of a Steam Atmosphere during Earth's Accretion. Icarus 74, 62-97.

Zhang, J., Herzberg, C., 1994. Melting experiments on anhydrous peridotite KLB-1 from 5.0 to 22.5 GPa. Journal of Geophysical Research 99, 17729-17742.

Zhang, J., Li, B., Utsumi, W., Liebermann, R.C., 1996. In situ X-ray observations of the coesite-stishovite transition: reversed phase boundary and kinetics. Physics and Chemistry of Minerals 23, 1-10.